

## Determination of magnetic resonance imaging biomarkers for multiple sclerosis treatment effects

Lyksborg, Mark; Larsen, Rasmus; Siebner, Hartwig Roman

*Publication date:*  
2013

*Document Version*  
Publisher's PDF, also known as Version of record

[Link back to DTU Orbit](#)

*Citation (APA):*

Lyksborg, M., Larsen, R., & Siebner, H. R. (2013). Determination of magnetic resonance imaging biomarkers for multiple sclerosis treatment effects. Kgs. Lyngby: Technical University of Denmark (DTU). (PHD-2013; No. 297).

## DTU Library

Technical Information Center of Denmark

---

### General rights

Copyright and moral rights for the publications made accessible in the public portal are retained by the authors and/or other copyright owners and it is a condition of accessing publications that users recognise and abide by the legal requirements associated with these rights.

- Users may download and print one copy of any publication from the public portal for the purpose of private study or research.
- You may not further distribute the material or use it for any profit-making activity or commercial gain
- You may freely distribute the URL identifying the publication in the public portal

If you believe that this document breaches copyright please contact us providing details, and we will remove access to the work immediately and investigate your claim.

# **Determination of magnetic resonance imaging biomarkers for multiple sclerosis treatment effects**

Mark Lyksborg

Kongens Lyngby 2013  
PHD-2013-297

Technical University of Denmark  
Institute for Applied Mathematics and Computer Science  
Building 321, DK-2800 Kongens Lyngby, Denmark  
Phone +45 45253351, Fax +45 45882673  
[reception@imm.dtu.dk](mailto:reception@imm.dtu.dk)  
[www.imm.dtu.dk](http://www.imm.dtu.dk)

PHD: ISSN 0909-3192

# Summary

---

This thesis describes methods for deriving multiple sclerosis (MS) biomarkers from Magnetic resonance images (MRI).

MS results in a neurodegenerative disease course to which MRI has proven sensitive. In particular diffusion MRI (dMRI), a modality reflecting microstructural properties of brain tissue has shown sensitivity towards the disease pathology of MS. We introduce three different methods for analysing MRI/dMRI in the white matter (WM) tracts, of an MS population. One method detects group-wise, tract-oriented differences based on features of the local diffusion tensor model. The next method, anatomical connectivity mapping (ACM) reflects voxel-wise whole-brain connectivity and is used to investigate cross sectional disease-related connectivity alterations. The third method presented is a voxel-based segmentation method able to detect WM abnormalities (WM lesions), with the potential of being used as lesion load markers often reported in clinical studies.

The main result of the first method is statistical differences between healthy controls and MS patients in 11 WM tracts. The ability to distinguish the clinically defined subtypes of relapse remitting and secondary progressive MS patients is found based on the ACM method. Using ACM, localized statistical differences were detected in the bilateral motor tracts. The most interesting result of the lesion segmentation method study, was that it achieved a segmentation performance which was better than two competing methods relative to the manual segmentations of the radiographers.

The methods presented in the thesis are useful in studies of MS and are expected

to have widespread applications in neuroscience.

# Resumé

---

I denne afhandling beskrives metoder til udledning af biomarkører for multipel sklerose (MS) baseret på magnetiske resonans billeder (MRI).

Multipel sklerose resulterer i et neuro-degenerativt sygdomsforløb med en sygdomspatologi som kan måles med MRI. Diffusions MRI (dMRI) som afspejler hjernevævets mikro-strukturelle egenskaber, har vist udtalt følsomhed overfor sygdoms patologien af MS. I afhandlingen præsenteres tre metoder til at analysere MRI/dMRI i hjernens hvid substans strukturer hos MS patienter. Den første metode påviser struktur-specifikke forskelle mellem en MS patient gruppe og en rask kontrol gruppe baseret på egenskaber ved diffusionsprocessen. Den anden metode, anatomical connectivity mapping (ACM) afspejler voxel-vise, hel-hjerne forbindelser og benyttes som input til et tværstudie af MS populationen. Den tredje metode er en voxel-baseret segmenterings metode som gør brug af traditionel strukturel MRI til at segmenterer anormaliteter i den hvide substans (læsioner). Læsions segmenteringer benyttes ofte til at kvantificerer patienters læsions byrde i kliniske studier.

Hoved resultatet for den første metode er, at der findes statistiske signifikante forskelle mellem raske kontroller og MS patienter i 11 hvid substans strukturer. Ved brug af ACM metoden findes desuden statistiske signifikante forskelle mellem to kliniske patientgrupper, recidiverende remitterende og sekundært progressive patienter, hvor forskellene primært findes i bilaterale motor-relaterede hvid substans strukturer. Det mest interessante fund i relation til læsion segmenterings metoden, er at metoden viser sig at være bedre end to konkurrerende metoder, sammenlignet med manuelt indtegnede segmenteringer.

Ud over at kunne bruges til at studerer MS, forventes metoderne præsenteret i

afhandlingen at have generelle anvendelses muligheder indenfor neurovidenskab.

# Preface

---

This thesis was prepared at the Image Analysis and Computer Graphics group at the Technical University of Denmark (DTU), in fulfilment of the requirements to obtain the doctor of philosophy degree (Ph.D.), within the topic of medical image analysis. Two-thirds of the project funding originated from the danish council for strategic research through a research grant with the title "Optimised treatment and monitoring of multiple sclerosis". The grant is managed by associate professor, Finn Sellebjerg at Danish Multiple Sclerosis Research Center (DMSRC). The last third of the funding was contributed by the ITMAN Graduate School program at DTU while the Danish Research Centre for Magnetic Research (DRCMR) provided research facilities enabling the project.

The work herein represents selected parts of the research work carried out during the Ph.D. period. The thesis consist of two parts. The first part contains a summary which covers background information on multiple sclerosis and a description of the methods forming core parts of the research work. The second part is made up by manuscripts written during the Ph.D. It contains tree research papers and one abstract.

The project was supervised by professor Rasmus Larsen from DTU, by senior researcher, Ph.D. Tim Bjørn Dyrby and professor Hartwig Roman Siebner, the ladder two from DRCMR. Part of the research was conducted at the Microstructure Imaging Group (MIG) at University College London (UCL), UK, under the supervision of assistant professor Gary Hui Zhang whom I visited for 6 months.

Kgs. Lyngby, April 2012 Mark Lyksborg



# Papers included in the thesis

---

- [Cha: 8] M. Lyksborg, H. Lundell, N. Reislev, H. R. Siebner, R. Larsen, and T. B. Dyrby. Correcting geometric distortions of Echo Planar Imaging using demons and reversed phase encoding. *Proceedings of International Society for Magnetic Resonance in Medicine (ISMRM), the 20th annual meeting, Melbourne*, pp. 2578, 2012. (Published).
- [Cha: 9] M. Lyksborg, T. B. Dyrby, P. S. Sørensen, M. Blinkenberg, H. R. Siebner, D. Alexander, R. Larsen, H. Zhang. Tract-oriented statistical group comparison of diffusion in sheet-like white matter. *Proceedings of the 10th IEEE International Symposium on Biomedical Imaging: From Nano to Macro, San Francisco*, 2013. (Published, 7th of April).
- [Cha: 10] M. Lyksborg, H. R. Siebner, P. S. Sørensen, M. Blinkenberg, A. Dogonowski, E. Garde, GJM. Parker, R. Larsen, T.B. Dyrby. Secondary progressive and relapsing remitting multiple sclerosis leads to widespread decreased anatomical connectivity. *NeuroImage*, 2013. (In submission).
- [Cha: 11] Mark Lyksborg, Rasmus Larsen, Per Soelberg Sørensen, Morten Blinkenberg, Ellen Garde, Hartwig R. Siebner, and Tim Bjørn Dyrby. Segmenting Multiple Sclerosis lesions using a spatially constrained K-Nearest Neighbour approach. *Proceedings of the 9th international conference on Image Analysis and Recognition - Volume Part II (ICIAR'12)*, Springer-Verlag, 156-163, 2012. (Published).

## Other disseminations

Mark Lyksborg, Mads Fogtmann Hansen, Rasmus Larsen. Increasing Cone-beam projection usage by temporal fitting. *Proceedings of the 8th French-Danish Workshop in Spatial Statistics and Image Analysis in Biology, Copenhagen*, 40-43, 2010. (Published).

M. Lyksborg, R. Larsen, P. S. Sørensen, M. Blinkenberg, A. Dogonowski, E. Garde, GJM. Parker, H. R. Siebner, T.B. Dyrby. Anatomical Connectivity Mapping - Measuring connectivity changes in Multiple Sclerosis. *Proceedings of International Society for Magnetic Resonance in Medicine (ISMRM), the 20th annual meeting, Melbourne*, 2012. (Published).

J. Romme Christensen, R. Ratzer, L. Börnsen, E. Garde, M. Lyksborg, H.R. Siebner, T.B. Dyrby, P.S. Sørensen, F. Sellebjerg . Natalizumab treatment of progressive multiple sclerosis reduces inflammation and tissue damage - results of a phase 2A proof-of-concept study. *Congress of European committee for treatment and research in multiple sclerosis (EctrimS)*, 2012. (Published).

# Acknowledgements

---

Writing a Ph.D. thesis from start to end is a sizeable task and in my case one that involves a lot of people. This section expresses my gratitude to the people who have inspired and kept me company for the last tree years.

Without funding from the Danish Council for Strategic Research (grant 2142-08-0039) managed by associate professor, Finn Sellebjerg at Danish Multiple Sclerosis Research Center (DMSRC), co-funding from the Danish Research Centre for Magnetic Resonance (DRCMR) and the Technical University of Denmark (DTU), this project would not have been possible. I would therefore like to thank these funding bodies. A special thanks to my main supervisors Rasmus Larsen (DTU), Tim B. Dyrby (DRCMR) and Hartwig R. Siebner (DRCMR) for your support, encouragement and discussions.

I would additionally like to thank the co-authors of the manuscripts and abstracts made throughout the Ph.D. In alphabetic order of appearance: Daniel C. Alexander, Ellen Gaarde, Gary H. Zhang, Geoffrey J.M. Parker, Henrik Lundell, Morten Blinkenberg, Nina Reislev and Per S. Sørensen. I owe a great debt to : Daniel C. Alexander and Gary H. Zhang for letting me visit the Microstructure Imaging Group (MIG) at University College London (UCL) for 6 months. I really enjoyed my stay and getting to know the many people at MIG. Thanks.

Thanks are due to all past and present members of the Danish Research Centre for Magnetic Resonance and the Image Analysis and Computer Graphics group at DTU Compute for fruitful discussions and a pleasant atmosphere. A special thanks to Jakob Wilm, Oula Pounti and Henrik Lundell for reviewing various aspects of the thesis.

x

---

# Abbreviations

---

AD	axial diffusivity
ALS	amyotrophic lateral sclerosis
CC	corpus callosum
cm-rep	continuous medial representation
CSF	cerebrospinal fluid
CST	corticospinal tract
DCT	discrete cosine transformation
dMRI	diffusion magnetic resonance imaging
DT	diffusion tensor
DTI-TK	diffusion tensor imaging tool kit
DWI	diffusion weighted imaging
EDSS	expanded disability status scale
EM	expectation-maximization
EPI	echo planar imaging
FA	fractional anisotropy
FFD	free form deformation
FLA	flip angle

FLAIR	fluid attenuated inversion recovery
fMRI	functional magnetic resonance imaging
FS	finite strain
GLM	general linear model
GM	grey matter
ICM	iterated conditional modes
IFO	inferior fronto-occipital fasciculus
ILF	inferior longitudinal fasciculus
K-NN	K-nearest neighbour
MD	mean diffusivity
MI	mutual information
mm	millimetre
MNI	Montreal neurological institute
MPRAGE	magnetization prepared rapid gradient echo
MRF	Markov random field
MRI	magnetic resonance imaging
MS	multiple sclerosis
ms	millisecond
MVU	maximum variance unfolding
NMI	normalised mutual information
OF	overlap fraction
PCA	principal component analysis
PDF	probability density function
PP	primary progressive
PPD	preservation of principal direction
PR	progressive relapsing
PSF	point spread function

PWA	piecewise affine
RA	relative anisotropy
RD	radial diffusivity
rf	radio frequency
ROI	region of interest
RR	relapse remitting
s	second
SI	similarity index
SLF	superior longitudinal fasciculus
SP	secondary progressive
SPD	symmetric and positive definite
SSD	sums of square difference
SVM	support vector machine
TBSS	tract-based spatial statistics
TE	time echo
TN	tensor norm
TR	repetition time
UNC	uncinate fasciculus
VBA	voxel-based analysis
WM	white matter



# Contents

---

Summary	i
Resumé	iii
Preface	v
Papers included in the thesis	vii
Acknowledgements	ix
Abbreviations	xiii
<b>I Summation</b>	<b>1</b>
<b>1 Introduction</b>	<b>3</b>
1.1 Scope of the project . . . . .	3
1.2 Multiple sclerosis . . . . .	4
1.3 Magnetic resonance imaging . . . . .	6
1.4 Thesis objectives . . . . .	10
1.5 Thesis outline . . . . .	10
<b>2 Data</b>	<b>13</b>
2.1 Siemens Trio . . . . .	13
2.2 Siemens Verio . . . . .	14
2.3 Subject assigned to thesis manuscripts . . . . .	15
<b>3 Diffusion MRI</b>	<b>17</b>
3.1 Introduction . . . . .	17

3.2	Background . . . . .	19
3.3	Artefacts . . . . .	21
3.4	Modelling fiber orientation . . . . .	24
3.5	Tractography . . . . .	31
3.6	Anatomical connectivity mapping . . . . .	38
3.7	Sheet-like models of white matter . . . . .	42
<b>4</b>	<b>Image Registration</b>	<b>55</b>
4.1	Introduction . . . . .	55
4.2	Methodology . . . . .	56
4.3	Thirion's demons . . . . .	69
4.4	Tensor reorientation strategies . . . . .	74
4.5	Tensor based image registration . . . . .	76
4.6	Building an atlas . . . . .	81
<b>5</b>	<b>Cross Subject Statistical Analysis</b>	<b>85</b>
5.1	Introduction . . . . .	85
5.2	The general linear model - Disease score modelling . . . . .	86
5.3	Localized sample based analysis . . . . .	87
5.4	Tract-oriented analysis . . . . .	89
<b>6</b>	<b>Tissue Segmentation</b>	<b>93</b>
6.1	Introduction . . . . .	93
6.2	Image features . . . . .	94
6.3	Markov random field segmentation . . . . .	96
6.4	Assessment of segmentation quality . . . . .	100
<b>7</b>	<b>Contribution Overview</b>	<b>103</b>
7.1	Correcting geometric distortions of Echo Planar Imaging using demons and reversed phase encoding . . . . .	103
7.2	Tract-oriented statistical group comparison of diffusion in sheet- like white matter . . . . .	105
7.3	Secondary progressive and relapse remitting multiple sclerosis leads to widespread decreased anatomical connectivity . . . . .	105
7.4	Segmenting Multiple Sclerosis Lesions using a Spatially Constrained K-Nearest Neighbour approach . . . . .	106
7.5	Conclusion . . . . .	107
<b>II</b>	<b>Contributions</b>	<b>109</b>
<b>8</b>	<b>Correcting geometric distortions of Echo Planar Imaging using demons and reversed phase encoding</b>	<b>111</b>

<b>9</b>	<b>Tract-oriented statistical group comparison of diffusion in sheet-like white matter</b>	<b>117</b>
<b>10</b>	<b>Secondary progressive and relapsing remitting multiple sclerosis leads to widespread decreased anatomical connectivity</b>	<b>125</b>
<b>11</b>	<b>Segmenting Multiple Sclerosis lesions using a spatially constrained K-Nearest Neighbour approach</b>	<b>147</b>



## Part I

# Summation



# Introduction

---

## 1.1 Scope of the project

The determination of multiple sclerosis (MS) biomarkers from images are motivated by several potential applications. They could be used as a supportive tool of the neurologist diagnosing MS. In fact, magnetic resonance imaging (MRI) already plays a key role when diagnosing MS, based on the McDonald criteria [103], [127], [126]. The McDonald criteria specifies the clinical symptoms patients must present with, to be positively diagnosed with MS. The most recent revision of the criteria includes MRI findings as part of making the diagnosis. This allows an earlier diagnosis since it can be made from fewer clinical symptoms if abnormal findings are present in the spinal cord or brain MRI. Image based biomarkers could also be used to assess the current state of the disease, aiding the treating neurologist in assessing the efficacy of a treatment and to determine future treatment. Compared to disease severity assessment made solely from a clinical exam, imaging markers have the benefit of being unbiased to factors which may affect the outcome of a neurologic exam, for instance due to patient fatigue and/or the treating neurologist level of experience. Removing/controlling the effects of such factors is important when testing the effect of a treatment, to allow an unbiased assessment.

The main funding source of the project originates from the Danish Council

for Strategic Research (grant 2142-08-0039, titled "Optimized treatment and monitoring of multiple sclerosis"). Several parallel Ph.D. projects are supported by this grant and the topics of these projects differ but are centered on clinical treatments trials, the study of blood, genetic and immunologic markers. These trials are supplemented by MRI markers some of which are calculated based on material presented in this thesis.

## 1.2 Multiple sclerosis

Most MS patients debuts during their late twenties or early thirtys, with a higher incidence rate amongst women relative to men. According to statistics released by the danish sclerosis association (<http://scleroseforeningen.dk/fakta-om-sclerose>, 15/11-2012), about 2/3 of the incidences are female while 1/3 are male. There are approximately 12500 diagnosed cases in Denmark with about 700 new cases arising each year.

Despite being recognized as an independent disease for more than 150 years [33], the exact cause of MS is unknown. It has been suggested that MS occurs as a result of genetic, environmental and infectious factors, [50], [102], [40] or combinations hereof. The genetic factor is supported by the increased recurrence rates in families [39]. For instance, studies involving identical twins have reported recurrence rates of 30 percent as opposed to none identical twins where the recurrence rates drops to approximately 5 percent. An environmental factor such as sunlight which increases production of D-vitamins, has been proposed to explain why people living farther from the equator are at higher risk of MS [9] while others suggest the increased stress levels of people living further from the equator as the explanation for the increased incidence rates [102]. Examples of infectious factors, believed to increase the risk of MS are viruses such as Epstein-Barr virus (Herpes), Chlamydia and Measles [69], [68]. Although plausible arguments can be made for all of these factors no definitive proof has been found.

### 1.2.1 Diagnosis and assessment

Diagnosis of MS is done by a neurologist according to the afore mentioned McDonald's criteria [103] where MRI plays a crucial role. Observing abnormalities in the white matter (WM) of an MRI exam can aid the diagnosis in cases where the clinical evidence in favour of MS diagnosis is otherwise weak.

Clinicians further classify MS patients based on a characterisation of their disease course [96]. Most patients start out being classified with the relapse remitting (RR) MS phenotype. The disease course of RR-MS patients is characterized by the repeated occurrence of MS attacks (relapses), followed by periods of remission where full or partial recovery occurs. Following a number of years, the patients will begin to experience gradual accumulation of disability in combination with relapses. This defines another MS phenotype known as secondary progressive (SP)-MS. Two other phenotypes used by clinicians are, the primary progressive (PP) characterized by a steady neurological decline from disease onset and the progressive relapsing (PR) phenotype which is similar to PP but with superimposed relapses occurring along with the steady neurological decline.

Patient treatments differ depending on the phenotypes classification. The RR-MS patients are typically treated by immunomodulatory drugs which decreases the occurrence rate of relapses [119], [105], [125], thereby delaying the progression rate of severity otherwise caused by an incomplete recovery from a relapse. Drugs with similar effects have also been approved for SP-MS patients, mainly intended to decrease the number of relapses experienced. At the time of writing, no treatment has shown convincing evidence of slowing the accumulation of disability in purely progressing patients such as PP-MS. As a consequence, there is no FDA (Food and Drug Administration) approved treatment of this phenotype.

The phenotype classifications are not very specific to assessing the current state of disease severity and are primarily used by neurologists to indicate which type of treatments is suitable. A more useful measure for assessing the disease severity is Kurtzkes expanded disability status scale (EDSS) [87], a quantity often used in treatments trials. The EDSS score quantifies disability of the eight functional systems; the pyramidal, cerebellar, brain-stem, sensory, bowel and bladder, visual, cerebral and other. The score ranges from 0 to 10 and increases in steps of 0.5. The EDSS=0 means no disability, the EDSS interval 1.0-4.5 generally refers to MS patients who are fully ambulatory (patients able to move around on their own), the EDSS interval 5.0-9.5 is defined by patients suffering from impairment due to ambulation (needs assistance to move around) while EDSS=10 means death due to MS. When assessing the sensitivity of various disease markers, EDSS scores or functionally specific scores are commonly used as the (ground truth) measure with which markers should correlate [56], [36], [57].

### 1.2.2 A microscopic view

To understand the effect that MS exerts on the brain a simplistic description of how the brain is wired for communication is first given (Figure 1.1). The

neuronal cells located in the cortical gray matter of the brain communicate by sending electrical signals along neural fibers called axons. The axons are encapsulated by the insulating substance of myelin (a lipid substance), found in the WM of the brain [72]. A schematic of the major WM components of the brain is included in Figure 1.1. It depicts the location of neurons at the end of myelinated axons, the oligodendrocytes which are responsible for myelin production as well as astrocytes (regulatory cells), microglial cells (immune cells), and blood capillaries, all central to maintaining balance in the micro-structural environment. An analogy to the brains network is a computer network where the neuronal cells are equivalent to the processing units (computers) while the axons correspond to the cabling of the network.

Multiple sclerosis is commonly perceived as a disease driven by WM pathology changes. Recent years have added additional complexity to this perception by revealing diffuse pathology changes in GM [11], [58] however the focus of the thesis will be limited to WM pathology. The WM pathology typically manifests as damage to the fatty myelin sheaths surrounding the axons of the brain and spinal cord, leading to demyelination and scarring of the brain. When myelin is lost, the axons can no longer effectively conduct electrical signals resulting in neurological disability. In our computer network example this corresponds to cutting or stripping the network cables of its insulation material resulting in decreased network performance. If a link/axon is completely severed, no communication may pass and the network message being sent may either come to a halt or have to pass through alternative cabling/axons. Detecting where and how the WM changes in relation to MS, is the main research questions addressed in this thesis. This question is addressed using MRI since the micro-structural changes due to MS, causes changes of the tissue composition which are measurable using MRI.

### 1.3 Magnetic resonance imaging

Magnetic resonance imaging (MRI) is used for in vivo imaging of soft tissue where the imaging contrasts arise due to different magnetic properties of the tissue types [72]. Images are acquired by positioning a subject within the bore of an MRI scanner made by a superconducting magnet which enables a strong magnetic field causing the water molecules, more specifically the protons of the body to align with the field. By briefly disturbing this field, the magnetic directionality of the molecules is changed and the molecules will over time re-establish their alignment with the field. During this spin realignment phase, the spins of the molecules induce a current which is read out by the scanners receiver coils. Numerous ways of disturbing the magnetic field and reading out signals

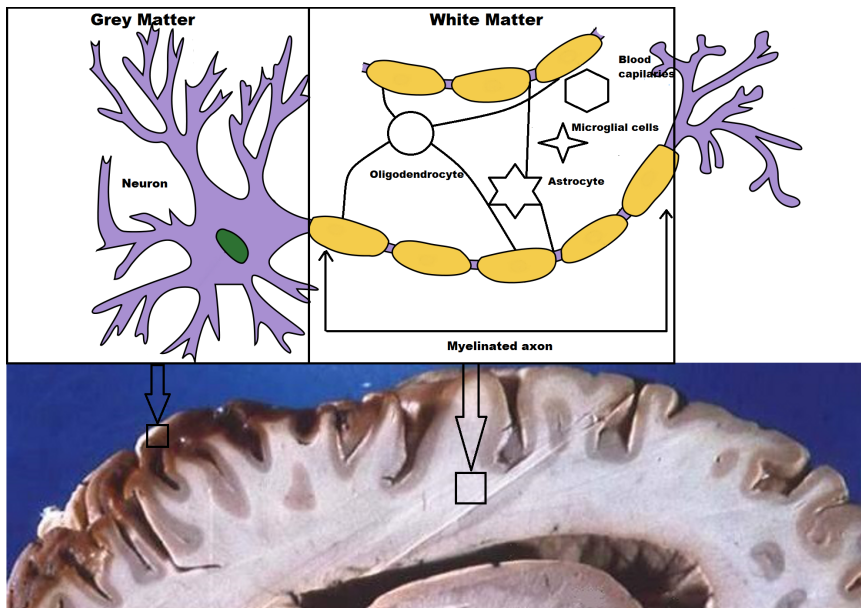


Figure 1.1: The two boxes at the top, illustrates major components of micro-structural environment of the brain. It depicts a grey matter neuron connected to myelinated axons in white matter and various immune cells. Each oligodendrocyte cell is attached to several axons and is responsible for myelin production. The astrocytes are regulatory cells maintaining homoeostasis while the microglial cells are immune cells combating infections, mobbing up debris and dying cells. These components are all connected in a symbiotic network relationship and therefore localized damage to any of these components may have longer ranging effects on the brains network. The bottom box shows a sagittal slice of the brain. The arrows originating from this box indicates the location of the micro-structural components.

exist. This give rise to different imaging contrast; such as T1 weighted images of magnetization prepared rapid gradient echo (MPRAGE) and T2 weighted images such as T2, fluid attenuated inversion recovery (FLAIR), functional MRI (fMRI), diffusion MRI (dMRI) and multiple others. The T2 and FLAIR modalities are commonly used to detect WM abnormalities (lesions) which appear as hyper intense voxels and are often used as part of McDonald's criteria. Multiple MS studies [57], have used the number of lesions as an image based marker hypothesized to correlate with the clinical disease scores. These studies widely agree that lesion load is an insufficient marker [56] but remains an often used marker in MS studies. *One of the three thesis objectives, is to perform an automated segmentation of WM lesions, allowing the estimation of lesion loads.*

Diffusion MRI [72] is believed to more accurately reflect changes of the WM compared to other modalities and is the area of focus throughout the thesis. It is an imaging modality sensitive to the mobility of water molecules and since this mobility is restricted/hindered by the micro structural environment of the brain tissue, the images are reasonably assumed to provide detailed information about the micro-structural information of the tissue. It may be able to provide qualitative information of the pathologies present in MS such as inflammation, axonal demyelination, Wallerian degeneration and atrophy as illustrated in Figure 1.3 which are known from histopathology to alter the micro-structural environment [59]. *Based on dMRI the second objective of the thesis is to quantify the accumulated effects these local pathologies have on the whole-brain connectivity of the WM network.*

Diffusion MRI can also be used to construct geometric representation of WM structures (tracts) which approximate the underlying geometry of axons. This makes it possible to analyse the properties of the diffusion process in a structure specific manner. *The third objective of the thesis, is to develop tools for assessing the health status of tissue of specific WM tracts and we shall widely refer this concept as tract-oriented analysis.*

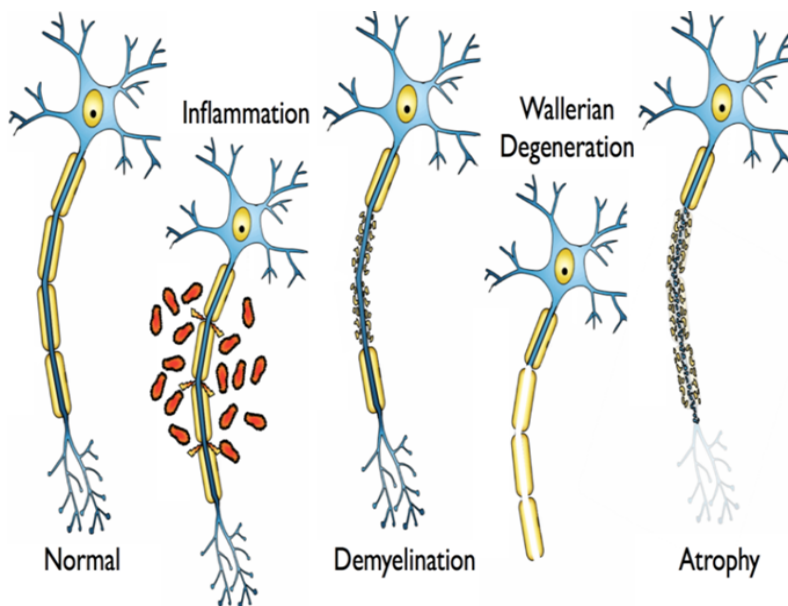


Figure 1.2: Illustrates the different disease pathology typically found in MS and a healthy axon. Inflammation usually occurs following an MS attack, as the micro-structural environments tries to mends tissue damage. The demyelination pathology is characterized by disintegration of myelin while the axon remains and occurs when i-reversible damage occurs. Wallerian degeneration typically occurs as an effect of distant axon injury causing the axon to disintegrate. Atrophy describes a state where micro-structural tissue has completely disintegrated.

## 1.4 Thesis objectives

The three main objectives of the thesis forming the basis of the derived papers of chapter 8-11 are:

- To develop tools for analysing the structural network integrity of the brain and use these tool to assess global and localized MS damage.
- To develop methodology for doing tract-oriented WM analysis and applying it to dMRI of MS patients.
- To segment WM lesions, using multiple MRI modalities and spatial features.

## 1.5 Thesis outline

The thesis is split into two parts.

Part I introduces and describes the methodologies used throughout the thesis manuscripts of part II. It covers dMRI processing, image registration, statistical analysis and brain tissue segmentation methods. To perform neuroimaging studies all of these method components may be involved. An analysis pipeline could for example consist of; 1) processing dMRI to enable further analysis, 2) image registration of all subjects to the same space ensure voxel-wise cross subject correspondence and 3) statistical analysis of voxels to decide disease score correlation or determine group-wise differences. Although tissue segmentation is not mentioned in this pipeline it may be used at all stages of the pipeline. For instance, to supply regions of interest for speeding up 1), to improve image registration accuracy of 2) or to remove the impact tissue volumes may have on 3).

Part II consists of self-contained manuscript prepared during the course of the Ph.D.

## Part I

**Chapter 1** is a general background and introductory chapter. It motivates the search for disease markers in MS and gives an introduction of the disease at a macroscopic and microscopic level. This is followed by a

general introduction to MRI. The chapter is concluded with stating the three main objectives of the Ph.D.

**Chapter 2** describes the MRI acquisitions of healthy control subjects and MS patients.

**Chapter 3** introduces diffusion MRI (dMRI). It covers a description of the diffusion process that gives rise to the dMRI, before explaining how to fit mathematical models to the dMRI signal enabling macroscopic reconstruction of the WM fascicle (WM tracts).

**Chapter 4** describes image registration methods. The chapter covers the methodological components involved in solving registration problems, from using rigid deformation models to highly flexible models. From deformation rigid models to highly flexible models. It also describe a high dimensional image registration method and how to construct population specific atlases.

**Chapter 5** describes statistical methods used to answer voxel-based, tract-oriented or whole-brain hypothesis, for example used to answer if there is statistical evidence of correlation between imaging markers and clinical outcome measures such as the EDSS disease score or to investigate group difference between MS patients and healthy controls or MS phenotypes.

**Chapter 6** suggest an approach for MRI tissue segmentation based on a voxel-based Markov random field (MRF) segmentation approach. The approach aimed at segmenting lesions based on multi-modal image features is described in detail.

**Chapter 7** gives an overview of the manuscripts of the thesis, by outlining the motivation, the objectives, the methodology and the main findings of the studies performed during the Ph.D. period.

## Part II

**Chapter 8** solves the problem of correcting geometric distortions of EPI sequences. It is based on the idea of acquiring two equally distorted images but with opposite directional distortion. We use image registration to estimate the voxel displacement corresponding to the distortion between the two images which is used correct the images of an EPI sequence. The correction approach is compared visually and quantitatively to two other approaches.

**Chapter 9** suggest an approach for tract-oriented group-wise comparison of diffusion indices defined on a sheet-like model. The approach models the sheet-like manifolds of 11 WM structures and performs statistical analysis

of diffusion indices sampled on the manifolds. The approach is demonstrated in a comparison study between healthy controls and MS patients.

**Chapter 10** studies the technique of ACM estimated using a pipeline particularly suited for group studies. The manuscript investigates how structural connectivity changes in WM regions due to MS, demonstrating that MS leads to widespread decreased connectivity and that the connectivity of certain localized WM regions, have a strong relationship with the MS disability which is measured by the EDSS.

**Chapter 11** describes a method for segmenting WM lesions using a spatially constrained K-nearest neighbour (K-NN) approach where the spatial smoothness constraints of the segmentations are introduced as the prior in a Bayesian formulation. The method is trained/tested and validated on structural and diffusion MRI of 15 MS subjects. It results in superior segmentation performance compared to freely available supervised segmentation methods.

## CHAPTER 2

# Data

---

The magnetic resonance imaging (MRI) of the thesis was acquired using two different scanners, a 3 Tesla Siemens Trio or Verio scanner. Subjects were scanned by; MD, Ph.D., Anne-Marie Dogonowski (TRIO) and Ph.D. student, M.Sc, Nina Reisleiv (Verio) at the Danish Research Centre of Magnetic Resonance. This chapter details thesis relevant subject demographics and outlines the sequences used to acquire MRI.

### 2.1 Siemens Trio

MRI data from 42 clinically stable patients suffering from MS, classified with an RR (n=27) or SP (n=15) phenotype and 25 healthy control subjects were acquired. The MS subjects had clinical disability rated according to the EDSS score, ranging from 0.0 to 7.0 with a mean $\pm$ standard deviation of  $4.31 \pm 1.77$ . Since the RR disease course is often the disease stage prior to SP, the EDSS of this group was not surprisingly lower. The EDSS range of the RR group was 0.0-4.5 and 3.5-7.0 for the SP group. The age of the patients range from 25 to 64 years with a mean of 43.57 years, and a gender split of 20 males and 22 females. Patients were under treatment with immunomodulatory drugs, such as Interferon- $\beta$ , Glatiramer acetate and Natalizumab (also known as Tysabri).

The 25 healthy control subjects had an age range of 26-69 with a mean of 43.4 years and a gender split of 10 males/15 females. Further details about subjects demographics and treatments can be found in the Ph.D. thesis of Anne-Marie Dogonowski [47]

Three different structural imaging modalities were acquired for each subject; 1) A T1-weighted image (MPRAGE) with a repetition time (TR)=1550 ms, an echo time (TE)=3.04 ms, a 9° excitation flip angle (FLA) and an imaging matrix of  $182 \times 218 \times 182$  acquired at  $1^3 \text{ mm}^3$  isotropic resolution. 2) A T2-weighted image (T2) using TR=3000 ms, TE=354 ms, FLA=180°, a voxel resolution of  $1.1^3 \text{ mm}^3$  and an imaging matrix of  $196 \times 256 \times 192$ . 3) A T2-weighted image (FLAIR) with TR=6000 ms, TE=353 ms, FLA=180°, a  $1.1^3 \text{ mm}^3$  resolution and a matrix of size  $220 \times 256 \times 192$ .

A whole-brain diffusion MRI (dMRI) was acquired using the twice-refocused spin echo sequence [131]. The echo planar imaging (EPI) sequence, consist of 71 sequentially recorded images, including 10 b0 images with no diffusion sensitivity and 61 diffusion weighted images (DWI)s acquired at 61 directions with gradient strength and diffusion time yielding a b-value of  $1200 \text{ mm}^2/\text{s}^2$ . Each image was acquired with sequence parameters TR=8200 ms, TE=100 ms, FLA=90° and an isotropic voxel size of  $2.3^3 \text{ mm}^3$  with an image matrix size of  $96 \times 96 \times 61$ . To make possible retrospective inhomogeneity distortion correction, a field map imaging sequence was acquired just prior to dMRI. It was based on a double gradient echo sequence with TR=479 ms with short and long echo times, TE<sub>1</sub>=5.19 ms, TE<sub>2</sub>=7.65 ms, FLA=60°, image matrix size  $128 \times 128 \times 47$  and a voxel resolution of  $2 \times 2 \times 3 \text{ mm}^3$ .

## 2.2 Siemens Verio

MRI data of five healthy subjects were acquired on this scanner. They are only used in the manuscript of chapter 8 which has the purpose of comparing the performance of geometric distortion correction approaches. Correspondingly, making information about subject demographics irrelevant.

A T1-weighted structural image (MPRAGE) was acquired with TR=1900 ms, TE=2.32 ms, FLA=9° and an imaging matrix of  $224 \times 256 \times 256$  at  $1^3 \text{ mm}^3$  isotropic resolution.

A whole-brain dMRI was acquired using the twice-refocused spin echo sequence [131]. The sequence consist of 71 sequentially recorded images, including 10 b0 images with no diffusion sensitivity and 61 DWIs encoded using 61 non-collinear

directions with gradient strength and diffusion time yielding a b-value of 1500 mm/s<sup>2</sup>. Each image was acquired with sequence parameters TR=11400 ms, TE=89 ms and an isotropic voxel size of 2.3<sup>3</sup> mm<sup>3</sup> with an image matrix size of 96 × 96 × 61.

To make possible retrospective inhomogeneity distortion correction of dMRI using either of three methods, three additional sequences were acquired. 1) A field map imaging sequence was acquired just prior to dMRI. It was based on a double gradient echo sequence with TR=479ms with short and long echo times, TE<sub>1</sub>=4.92 ms, TE<sub>2</sub>=7.38 ms, FLA=60°, image matrix size 64 × 64 × 42 and a voxel resolution of 3 × 3 × 3 mm<sup>3</sup>. 2) An additional b0 image was acquired using the same b0 sequence parameters but with a reversed phase encoding direction causing distortion artefacts to occur opposite of the standard phase encoding direction. 3) A sequence for mapping the point spread function (PSF) was acquired using the same EPI parameters as the dMRI acquisition.

## 2.3 Subject assigned to thesis manuscripts

All data was acquired before starting this thesis but not all data was easily accessible from the database system of the hospital. These problems have had an impact on which subjects are included in the four studies of thesis.

The paper described in Chapter 8 is based on data from an ongoing study of the blind population. Since only 5 healthy control subjects had been scanned at the time of publication, these 5 were included. Demographic information was not collected.

The paper of chapter 9 was done at University College London (UCL). Prior to leaving for London, the readily available MRI of MS and control were extracted from the hospital database. 35 MS and 25 healthy control subjects were successfully extracted using the database extraction pipeline. This gave 21 RR-MS and 14 SP-MS which were the basis of the study. The healthy subjects had an age range of 26-69 with a mean of 44.72 years. Based on their phenotype the SP-MS had an age range of 29-64 with a mean of 49.4 years and the RR-MS had an age range of 24-56 with a mean of 40.3 years.

Some of the initial failed data extractions were corrected upon returning from London and the work of the paper of chapter 10 was written. This paper is based on the Anatomical Connectivity Mapping (ACM). The estimation is based on probabilistic estimation is very time consuming if choosing to estimate on the ACM until convergence is achieved. This is what we did and ultimately

meant we did not manage to estimate the ACM for the full amount of subjects before thesis deadline. For this reason 19 RR-MS, 15 SP-MS patients and 20 healthy controls were included in the study. Even if we had enough time prior to deadline, it would not be possible to use the full set of subjects since one subject was missing a fieldmap sequence and two had extreme ghosting artefacts in the dMRI. The demographics of the group is found in the manuscript of chapter 10.

Finally, the paper of chapter 11 was limited to the same phenotype homogeneous group of 15 SP-MS patients.

# Diffusion MRI

---

## 3.1 Introduction

Diffusion magnetic resonance imaging (dMRI) can be used to infer the microstructural tissue compositions of a voxel. It has found application in early stage diagnosis of acute-stroke [161], and to study various neurological conditions such as Alzheimer’s disease [24], amyotrophic lateral sclerosis (ALS) [34], multiple sclerosis (MS) [36], [55], [57]. It is also widely used to infer the macroscopic geometry of the neuronal fiber pathways of white matter (WM) using the methods of tractography [13], [88].

This chapter introduces the diffusion process as measured by dMRI and the mathematical models used to infer the microscopic and macroscopic properties of the tissue. Section 3.2 will supply contextual background on how the diffusion process gives rise to signal changes in dMRI. Section 3.3 will give an overview of imaging artefacts influencing dMRI. Section 3.4 will introduce the widely used tensor model for quantifying the diffusion process in voxels of a single fiber population and its extension to the multi-fiber population. This section also explains how the principal direction of diffusion is derived from the tensor model and introduces scalar diffusion indices also derived from the tensor. The principal direction of the tensor model, are used by tractography algorithms to perform in-vivo reconstruction of the pathways of WM. Section 3.5 covers

both deterministic tractography and probabilistic tractography. Understanding both types of tractography is relevant to the remainder of the chapter, since probabilistic tractography is used to estimate the anatomical connectivity mapping (ACM), described in section 3.6 and deterministic tractography is used in section 5.4 to enable a geometric description of WM pathways. The ACM described in section 3.6 yields a scalar map reflecting the relative connectivity of each voxel with respect to the rest of the brain and was used in a cross sectional phenotype study, presented in chapter 10. The model based sheet-like geometric representation of WM pathways(tracts) introduced in section 3.7 concludes the chapter. In this thesis, this model is used to perform tract-oriented statistical analysis as detailed in section 5.4. A manuscript detailing the results of such tract-oriented analysis investigating a cohort of MS patients, can be found in chapter 9.

## 3.2 Background

Diffusion can be described as process of mass transport, resulting from molecular motion with no outside influence. A popular experiment illustrating the diffusion phenomenon is one of dropping a dye into a glass of water [17]. Over time the dye spreads, in a spherically symmetric profile with no external influences. This is known as diffusive mixing and results from collisions between atoms or molecules or particles in the liquid. The motion of this random process is also known as Brownian motion. It is the purpose of dMRI to measure the bulk of this motion. Einstein [52] came up with a simple mathematical description of the bulk motion which he showed follows a Gaussian distribution, when the assumption of free diffusion is upheld. In which case the mean-squared displacement is given by

$$\langle r \rangle^2 = 2 \cdot d \cdot D \cdot \tau, \quad (3.1)$$

where  $D$  is the diffusion coefficient (also called the apparent diffusion coefficient) we are interested in measuring using dMRI,  $\tau$  is time spend observing the diffusion process,  $\langle r \rangle^2$  is the mean squared displacement of the particles and  $d$  is the spatial dimensionality of the process.

The assumption of Gaussian displacement gives rise to a simple equation describing the relationship between the diffusion process and the diffusion weighted images (DWI)s of a dMRI acquisition. The equation is

$$I = I_0 \cdot e^{(-\tau q^T D q)}, \quad (3.2)$$

where  $D$  is a  $3 \times 3$  matrix and  $q$  is the so-called diffusion wavevector making the DWI contained in  $I$  sensitive to the mobility of water molecules along the gradient direction applied during the dMRI sequence.  $I_0$  is a T2-weighted image based on the same scanner sequence and timings as  $I$  but with the diffusion part omitted. The equation states that a change in  $I$ , relative to  $I_0$  can be described by an exponential attenuation, with the exponent given by the Gaussian diffusion process occurring along a fixed direction.

With the usage of the Stejskal-Tanner [141] pulse gradient spin-echo sequence and the Gaussian displacement model, eq. (3.2) can be re-written as

$$I = I_0 \cdot e^{-(\gamma \cdot \delta \cdot G)^2 (\Delta - \delta/3) \hat{q}^T D \hat{q}} = I_0 \cdot e^{-b \cdot \hat{q}^T D \hat{q}}. \quad (3.3)$$

$\delta$ ,  $G$  are equivalent to the duration and magnitude of the gradients,  $\Delta$  is the temporal time separation between the start of the two diffusion sensitizing gradients of the Stejskal-Tanner sequence,  $\gamma = 267.513 \cdot 10^6 \text{ rad s}^{-1} \text{ T}^{-1}$  is the gyromagnetic constant for protons and  $\hat{q}$  is the unit normalized direction of the

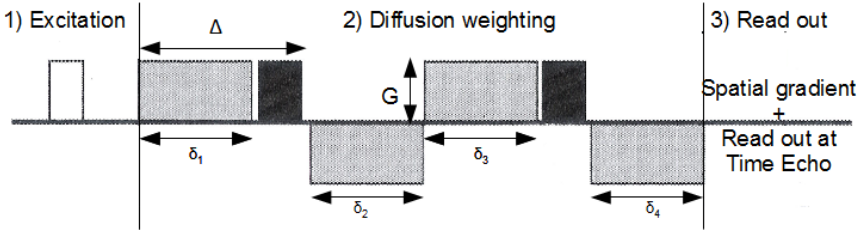


Figure 3.1: Sequence diagram illustrating the twice-refocused spin echo sequence. It depicts a division of the sequence into three parts; 1) MRI signal excitation using a radio frequency (rf) pulse, 2) the diffusion weighting part, consisting of four diffusion weighted gradients shown in grey each applied for a duration  $\delta_i$  with the magnitude  $G$  and two refocusing rf-pulses shown in black. Part 3) takes care of the data collection part of spatial gradient encoding and reading out the MRI signal.

wavevector  $q$ . The values of  $\delta$ ,  $G$  and  $\Delta$  are all sequence parameters influencing the amount of diffusion sensitivity encoded in the images. Altering these parameters will make the sequence more or less sensitive to diffusion. For spherical acquisition schemes these parameters are constant and are often summarized into a single b-factor as done in eq. (3.3). In general increasing the value of  $b$  will increase sensitivity to the slower diffusion processes but usually at the cost of compromising scan time and signal to noise ratio.

In this thesis the twice-refocused spin echo sequence [131] was used to acquire the DWIs. The sequence diagram of the twice-refocused spin echo sequence is illustrated in Figure 3.1. It shows a division of the sequence in three parts; 1) MRI signal excitation using a radio frequency pulse (rf), 2) diffusion weighting and 3) data read out, which consists of spatially encoding image positions using scanner gradients and reading out the image signal. Part 1) and 3) are common to all MRI sequences while part 2) is what make the diffusion sequence different from other MRI sequences. The twice-refocused sequence differs from other diffusion sequences since it consist of two pairs of diffusion sensitizing gradient pulses as opposed to just one as is the case with Stejskal-Tanner sequence. This has the positive effects of reducing eddy current artefacts (see section 3.3). DWIs acquired using the twice-refocused sequence can however still use the same signal attenuation equation as the Stejskal-Tanners, presented in eq. (3.3). This is achieved by setting  $\delta$  equal to the sum of the first and the third gradient durations,  $\delta = \delta_1 + \delta_3$  and  $\Delta$  to the temporal difference between the start of first and the third gradient, shown in Figure 3.1.

### 3.3 Artefacts

In this section we shall give an overview of four artefacts commonly occurring with echo planar imaging (EPI) sequences, the type of sequence used to acquire both the DWIs and the corresponding non-diffusion weighted images (b0). The artefacts may be caused by; physiological noise, tissues susceptibility, subject movement and eddy currents arising in the scanner hardware. Being aware of or actively correcting for these artefacts may improve the accuracy of statistical analysis based on the images.

#### Physiological noise

An example of physiologic noise that may corrupt the images of an EPI sequence is the cardiac cycle. It acts as a pulsation effect on the brain and failing to correct this artefact results in increased apparent diffusivity near the periventricular regions [153]. Although it is well recognized problem described in, [83], [82], [32], not many research groups actively acquire data with the aim of minimizing the artefact as could for instance be done by cardiac gated imaging. Nor have we taken steps to minimize this artefact.

#### Tissue susceptibility

Artefacts due to tissue susceptibility are largest at air-tissue interfaces of the brain and particularly near the frontal-lobe sinuses. The artefact occurs when the tissue of the subject disturbs the homogeneous field of the scanner. Since image reconstruction is based on the assumption of a completely homogeneous field, a local inhomogeneous field will cause this artefact. It manifests as geometric warping and local intensity build-ups in the images, occurring predominantly along the phase encoding direction. The phase encoding direction is often set to correspond with the anterior-posterior (AP) direction of the brain as to preserve brain symmetry despite warping. A popular way of correcting the artefact was suggested by [79]. It consists of acquiring a double gradient echo sequence using two distinct echo timings (TE). This so-called field map sequence makes it possible to estimate the voxel displacement map which gave rise to the geometric distortion and may be used to undistort the images. An example of the field map correction is given in Figure 3.2. Figure 3.2(a) depicts a slice of an EPI acquired image without diffusion weighting (b0) prior to distortion correction, Figure 3.2(b) depicts the same slice after distortion correction and Figure 3.2(c) shows the voxel displacement map used to correct the image.

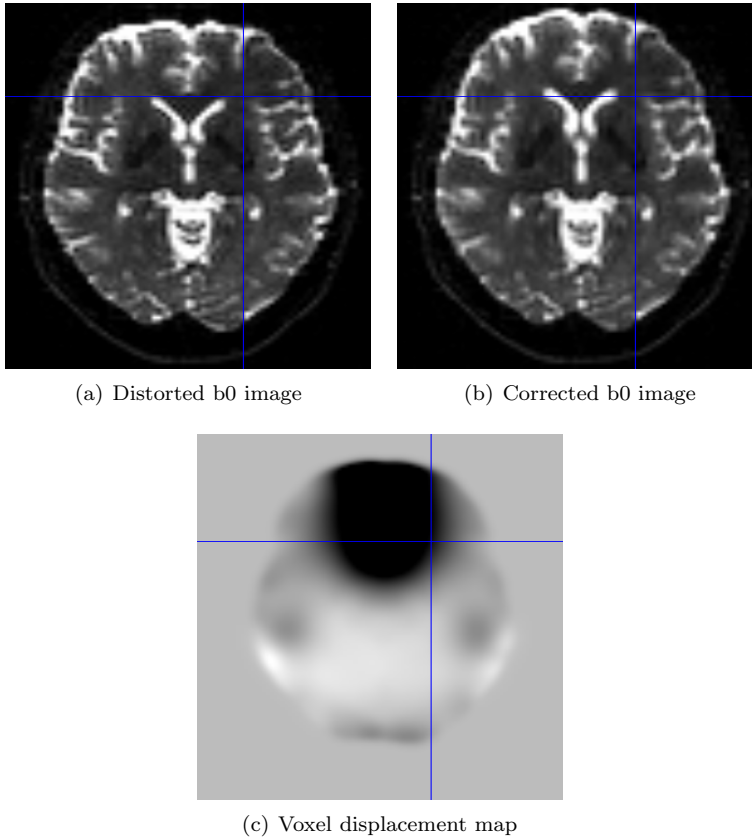


Figure 3.2: Illustrates the field inhomogeneity artefacts present in EPI data due to tissue susceptibility corrupting the homogeneity of the magnetic field. The axial slice in (a) depicts a distorted image while (b) depicts the same slice after a geometric distortion correction has been applied to (a). For comparison reasons the blue cross was positioned in the same location of the slice in (a),(b) and we note that the corrected image in (b) has been stretched along the anterior-posterior direction. The correction was based on the field map approach that outputs a voxel displacement map shown in (c)

Alternative ways of performing this correction is through the point spread function (PSF) method [178] and the reversed gradient method by [31]. The PSF method requires additional sequences from which to derive a voxel displacement map. The reversed gradient method is based on acquiring an additional b0 image but with an oppositely directed phase encoding direction of the EPI sequence compared to the usual b0 image. This results in a pair of b0 images where distortions are similar in magnitude but oppositely directed thus in one b0 image, features are compressed while they are stretched in the other. By identifying corresponding points in the two images it is possible to infer a voxel displacement map, possibly based on image registration as described in [73]. We shall re-visit this technique in the paper of chapter 8 where we suggest an extension of the approach and compare it with other approaches.

## Subject motion

Analysis based on the DWIs and b0 images, assumes that the field of view of every voxel comes from the same micro-structural tissue across all the images. As a consequence gross head movement during scan time may lead to erroneous analysis results. It is therefore common practice to rigidly align all images with the first b0 of the sequence.

## Eddy current

The eddy current artefact is caused by the rapidly switching gradients of the scanner which induce additional unwanted currents in the scanner hardware that can affect the magnetic field of the scanner in an undesirable manner. This artefact typically manifests as 2D affine distortion of image slices. It is common practice to assume that eddy current artefacts can be corrected using one single 3D affine model as described in [82]. This assumption allows simultaneous correction of motion-related and eddy current artefacts as they can both be corrected by aligning all images with the first b0 image using a 3D affine model. The affine model is fitted using image registration as described in chapter 4.

Throughout the thesis and unless otherwise stated we use a combination of the field map correction approach and an affine model to estimate a combined voxel displacement map that simultaneously compensates for susceptibility, movement and eddy current artefacts.

### 3.4 Modelling fiber orientation

#### The tensor model

Using the diffusion tensor (DT) model it is possible to quantify the amount of diffusion displacement occurring in a voxel and infer the direction along which a water molecule is most likely to travel. This is also called the principal direction. The matrix-vector formulation of the DT model has already been given in eq. (3.3), resulting in the diffusion attenuation equation for the  $i^{th}$  image

$$I_i = I_0 \cdot e^{(-b \cdot \hat{q}_i^T D \hat{q}_i)}, \quad (3.4)$$

where  $D$  is a  $3 \times 3$  dispersion matrix of 6 unique dispersion parameters reflecting the dispersion of the diffusion process while  $\hat{q}$  is the direction of diffusion sensitivity. The dispersion matrix of the DT is estimated by minimizing the least squares problem

$$\arg \min_D \left( \sum_{i=1}^n (\hat{I}_i - I_i)^2 \right), \quad (3.5)$$

with  $n$  denoting the number of DWIs. This non-linear problem is solved using a Levenberg-Marquardt algorithm [89], [101]. The dispersion in  $D$  is expected to be symmetric and positive definite (SPD) but the SPD property is easily violated due to noise and numerical inaccuracies, leading to non-physically meaningful DTs. To ensure the SPD property a Cholesky decomposition [160] can be used to estimate  $D$ . The decomposition is  $D = L^T L$  where  $L$  is a triangular matrix and the Cholesky product is guaranteed to give an SPD matrix. Therefore estimating the parameters of  $L$  instead of  $D$ , ensures that  $D$  will become SPD.

A simpler way of estimating  $D$  is to take the natural logarithm of the normalized signal of eq. (3.4), and to reorganize the problem as a system of linear equations solvable through matrix inversion. We avoid this approach, since it may result in DTs with no physical meaning and it has been demonstrated in simulation studies the approach is less accurate compared to the solution of solving the non-linear problem [82].

#### The principal direction of diffusivity

From the DT, it is desired to infer the principal direction since it is generally assumed to coincide with the tangential direction of a WM fiber. Such knowledge will allow in-vivo reconstruction of WM pathways. The direction is found as the principal axes of the Gaussian ellipsoid which explains the largest amount

of variation from the diffusion process. The directional variance is quantified in  $D$  where the three orthogonal axis of the ellipsoid are estimated by solving the eigen-system of equations

$$D\Phi = \Lambda\Phi, \quad (3.6)$$

where  $\Phi$  is a matrix of eigenvectors,  $\Phi = [e_1, e_2, e_3]$ . It is assumed that the eigenvalues in the diagonal matrix  $\Lambda$  are sorted according to size, meaning  $\lambda_1 > \lambda_2 > \lambda_3$  and therefore  $e_1$  is the principal direction.  $\lambda_1$  describes the variation of diffusivity along the principal direction while  $\lambda_2$  and  $\lambda_3$  quantify diffusivity occurring orthogonal to  $e_1$ .

## Scalar diffusion indices

From the eigenvalues of the DTs, a number of scalar diffusion indices quantifying properties of the DT have been proposed in literature [12]. The most used are, fractional anisotropy (FA), mean diffusivity (MD), radial diffusivity (RD), the tensor norm (TN) and have widely been used as indices indicating localised pathology changes of WM tissue. In the context of MS, people have shown reduced FA, along side reduced MD of both lesioned areas and in normal appearing WM (NAWM) [170], [36], [67], presumable reflecting axonal damage [35]. Localized changes in these indices have also been linked to disease-related disability [115] and to explore differences between the clinical phenotypes of MS [130].

Fractional anisotropy (FA) [12] is calculated using all the eigenvalues of a DT

$$FA = \sqrt{\frac{3}{2}} \cdot \frac{\sqrt{(\lambda_1 - \bar{\lambda})^2 + (\lambda_2 - \bar{\lambda})^2 + (\lambda_3 - \bar{\lambda})^2}}{\sqrt{\lambda_1^2 + \lambda_2^2 + \lambda_3^2}}. \quad (3.7)$$

FA values range from 0 to 1 and describe the degree of anisotropy of a DT. A value of 0 means the diffusion process is isotropic and a value of 1 means that the diffusion process is fully restricted along the principal direction. It is used in several studies, to indicate the myelination degree of WM. However it is a measure which can be difficult to interpret when the assumption of a one fiber model no longer holds. A voxel containing complex fiber configurations such as crossing, fanning or bending fibers will alter the FA in an unpredictable manner in which case it may be difficult to assess if FA changes are due to pathology or a complex configuration.

Another popular scalar measure used to assess micro-structural WM changes is the mean diffusivity (MD) which is calculated as the mean of the eigenvalues

$$MD = \frac{\lambda_1 + \lambda_2 + \lambda_3}{3}. \quad (3.8)$$

It reflects the average size of a DT, independent of orientation and shape and can be used to monitor certain disease conditions, particularly acute stroke where tissue changes due to stroke are observed earlier than with conventional MRI [161].

The tensor norm (TN) is calculated by

$$TN = \sqrt{\lambda_1^2 + \lambda_2^2 + \lambda_3^2} \quad (3.9)$$

and is simply the square root of the sums of squared eigenvalues.

Radial diffusivity (RD) is the average diffusion occurring perpendicular to the main principal direction and is estimated by

$$RD = \frac{\lambda_2 + \lambda_3}{2}. \quad (3.10)$$

It has been proposed as being particularly sensitive towards measuring the changes in MS, associated with Wallerian degeneration [92]. Often reported alongside RD, is the axial diffusivity (AD) which is the eigenvalue summarizing the average diffusion along the principal direction.

The montage in Figure 3.3 shows five diffusion indices, estimated from an MS patient with a WM lesion, indicated by the arrow. We see a decrease in FA values in the proximity of the lesion while both the AD and RD show increased diffusivity. Intuition suggests that a drop in FA must be caused by a larger increase in RD compared to the increase in AD, which has previously been observed in MS studies [26]. From the MD indices some unexpected dark voxel regions are seen. These occur at tissue interface boundaries where Gibbs ringing, image distortions and uncorrected motion artefacts can cause the diffusion tensors to reflect something which has no physical meaning. The work of the thesis considers analysis of cerebellar white where such artefacts are rare. For this reason we don't expect them to impact our results.

These indices all collapse the DT into an interpretable scalar unit however this may have the adverse effect of getting rid of interesting geometric diffusion properties of the underlying tissue. For instance the same FA value could arise from very different DT profiles thus simultaneous consideration of several indices may lead to increased insight. There are indices which try to take this issue into account. The Westin metrics [171] were proposed to decompose the DT into the three components of a linear, a planar and a spherical component and though we did not explore this approach, we can envision usefulness of such decomposition. Other interesting measures not treated here, include the relative anisotropy (RA) [14] and the skewness measure [121], the latter measuring higher order properties of the DT (the degree of pancake shape versus cigar shape).

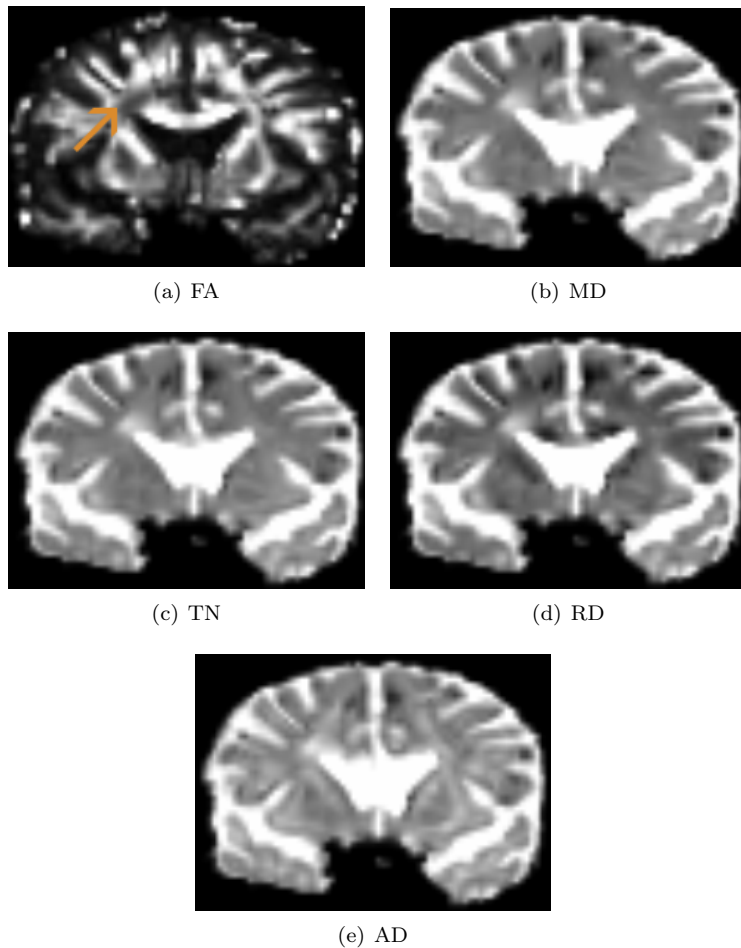


Figure 3.3: Depicts the scalar diffusion indices of FA, MD, TN, RD and AD. These coronal slices are from the frontal part of the brain where a lesion is present as indicated by the arrow in (a). The lesion is visible in all modalities though with slightly different contrast. From the MD indices some dark voxel regions are seen. These typically occur at tissue interface boundaries where Gibbs ringing, image distortions and uncorrected motion artefacts can cause the diffusion tensors to reflect something which has no physical meaning.

## Multi-tensor model

The multi-tensor model [152] is a generalization of the single tensor model which replaces one Gaussian model with a mixture of Gaussian models with the intended purpose of modelling mixed fiber distributions. The signal equation, describing the diffusion process from a mixture of Gaussians is

$$I_i = I_0 \cdot \sum_{j=1}^n a_j e^{(-b \cdot \hat{q}_i^T D_j \hat{q}_i)}. \quad (3.11)$$

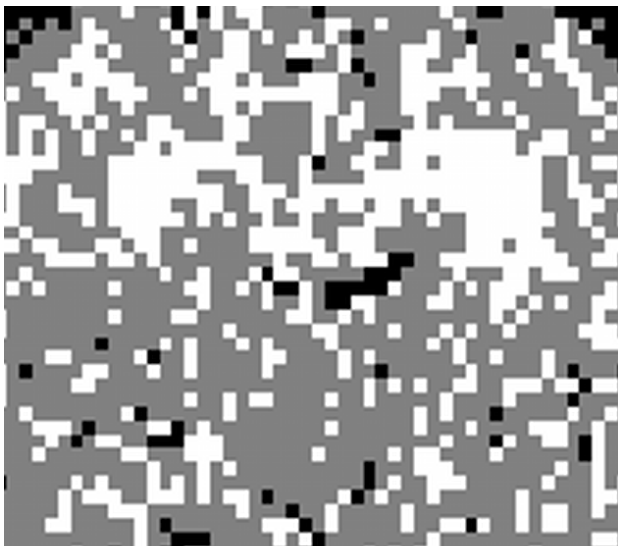
The equation contains the parameters of  $n$  covariance matrices  $D_j$ , the influence of which are determined by the weights  $a_j \in [0, 1]$  subject to the constraints that  $\sum_{i=j}^n a_j = 1$ . Estimating the model requires the use of non-linear optimization such as Levenberg-Marquardt [89], [101]. For stability reasons we use an approach enforcing that the second and third eigenvalues should be the same [4]. To estimate the multi-tensor model one needs to first determine the number of fiber populations  $n$ , within a given voxel.

The choice of  $n$ , poses a model selection problem where accuracy is lost by choosing  $n$  too large and choosing  $n$  too small, can lead to the estimation of incorrect principal directions of the DTs. To select  $n$  we use the approach proposed by Alexander et al. [3] and implemented in the Camino software package (<http://cmic.cs.ucl.ac.uk/camino/>). It classifies voxels as being either isotropic, one-fiber or two-fiber voxels. An example of the resulting classification as well as a corresponding multi-tensor slice is shown in Figure 3.4(a)-(b). From the classifications of the figure, the reader may notice a sparse number of isotropic CSF voxels and an over representation of one-fiber voxels (anisotropic voxels). This may make it difficult to distinguish anatomical structures from the classification map. However it has no consequence for the estimated diffusion tensors of these regions since a single tensor is fitted in both of these cases. Only when a two-fiber voxel is classified do we use a different model, namely the multi-tensor ( $n=2$ ).

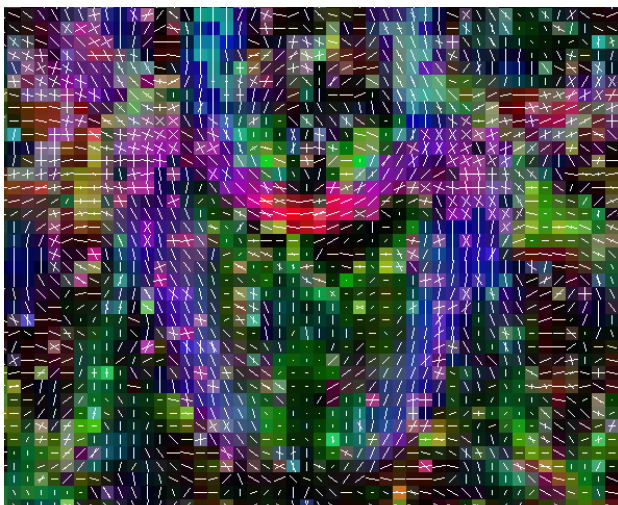
The classification is done by fitting several spherical harmonics series to the diffusion measurements of each voxel. Higher order models result in better fits where the quality of a model fit can be measured using the sums of squared residuals which follows a  $\chi^2$  statistic. The classification approach fits the spherical harmonics model of order 0, 2, 4, enabling the user decide a statistical threshold that justifies the use of higher order models. The threshold is compared to the F-test statistic of each voxel where the F-test statistic is calculated as the ratio between two  $\chi^2$  model fit statistics of two models with differing model order. Tree model comparisons are made requiring the user specification of tree F-test thresholds.

Camino ships with an interactive tool enabling users to adjust the model selection threshold on the fly. Adjustments may be done until the following criteria are visually satisfied; 1) voxels classified as order 0, correspond to cerebrospinal fluid (CSF) and grey matter (GM), 2) voxels with order 2 classification, correspond to WM and 3) voxels with order 4 classification, correspond to WM regions of crossing fibers, typically identified where the corticospinal tract (CST) and the corpus callosum (CC) intersect.

We use the multi-tensor to model multi-fiber voxels but a number of alternative approaches exist. An overview of these methods can be found in the book by Johansen-Berg et al. [72] which describe the methods of; the multi-tensor, ball and stick [16], persistent angular structure MRI (PASMRI) [1], spherical deconvolution (SD) [149], [148], diffusion spectrum imaging (DSI) [163] and qball imaging [151]. These model forms all have very different computational complexity and for instance the DSI require high resolution data beyond standard clinical sequences. In principle any of these approaches could be used instead of the multi-tensor. We choose this model primarily due to its simplicity and low computational complexity.



(a) Fiber classification



(b) Multi-Tensors

Figure 3.4: Illustrates the classification of dMRI voxels, classified as being either isotropic, anisotropic or a two-fiber compartment voxels and the multi-tensors fitted based on the classifications. (a) Shows the classification of a coronal slice with isotropic voxels in black, anisotropic voxels in grey and two-fiber voxels shown in white. (b) Shows a zoomed view of the principal directions of the fitted multi-tensors overlaid onto a directionally encoded RGB background image, red=left/right, blue=inferior/superior and green=anterior/posterior.

## 3.5 Tractography

Tractography methods are used with the purpose of in-vivo reconstruction of the WM pathways of the brain. Studies on post mortem minipigs [51] and rat brains [91] using tracer injection techniques have confirmed the ability of tractography methods, to infer WM pathways largely parallel with ex-vivo anatomy. The methods are commonly divided into two different types; deterministic and probabilistic methods, both generating connected curves in space. These curves are known as streamlines where a collection of spatially coherent streamlines is referred to as a fiber bundle or a WM tract.

During this section we shall describe the ideas behind two deterministic methods [13], [88] and one probabilistic method [118]. This subset of methods only covers a few of the available tractography methods. An outline of a wider range of methods may be found in the books of [72] and [81].

### Deterministic tractography

#### Euler's method

Euler's method for streamline estimation, was initially described in [13]. It is based on the assumption that a streamline may be represented by a curve in space  $r(s)$ ,  $s$  being the arc length of the curve and that the differential change of the streamline can be described using Frenet's equation [65],

$$\frac{dr(s)}{ds} = t(s) \quad (3.12)$$

Further, the normalized tangent of the streamline curve is assumed equal to the principal direction  $e_1$  of a voxel such that Frenet's equation may be re-written as

$$\frac{dr(s)}{ds} = e_1(r(s)). \quad (3.13)$$

In other words the tangential change of a streamline curve, at location  $r(s)$  is given by  $e_1(r(s))$ . This differential equation enables the estimation of  $r(s)$  using methods for solving differential equations. Euler's method is such a method, resulting in the iterative update,

$$r(s_1) \approx r(s_0) + h \cdot e_1(r(s_0)). \quad (3.14)$$

The streamline  $r(s)$  is estimated via this iterative update where the step length  $h$  determines the error of the approximation and  $r(s_0)$  is the streamline starting position (the seed voxel). The final streamline estimated by the method,

is constructed by combining two separate streamlines at the seed voxel. One streamline is initiated in the positive and the other is initiated in the negative  $e_1(r(s_0))$  direction. The combination of these two streamlines is required to estimate the full streamline, since the sign of the principal direction  $e_1$  is arbitrary.

### The tensor deflection method

Compared to Euler's methods, the strength of this method is an improved robustness when estimating streamlines through regions of high directional uncertainty. It was designed to work with the DT model and similar to Euler's method, the streamline evolves iteratively. The iterative update is given by

$$\begin{aligned} r(s_1) &\approx r(s_0) + h \cdot v_{out}, \\ v_{out} &= f \cdot e_1 + (1 - f) \cdot (1 - g) \cdot v_{in} + g \cdot D \cdot v_{in}, \end{aligned} \quad (3.15)$$

where  $v_{out}$  is the tracking direction at the front of the streamline,  $e_1$  is the principal direction at the current location,  $D$  is the tensor at the front of the streamline and  $v_{in}$  is the principal direction of the previous iteration. The values of  $f$  and  $g$  are user specified constants in the interval  $[0, 1]$  and for the specific case of  $f = 1$ ,  $g = 0$  the tensor deflection method is equivalent to Euler's method. Alternative values of  $f$  and  $g$  allows this approach to be tuned for specific tracking purposes [88], [165]. When used with  $f = 1$ ,  $g = 1$ , it was demonstrated in [88] that the tensor deflection term,  $g \cdot D \cdot v_{in}$  down-weighs the current direction of a tensor if it is highly isotropic, while ignoring  $v_{in}$  if the tensor at the current location is highly anisotropic. This is particularly useful when tracking through regions of crossing fibers, elucidated by the example in Figure 3.5 which visually compares a fiber bundle based on Euler's method in (a), (c) with a fiber bundle based on tensor deflection in (b), (d). Both methods are used to track the left CST using the same seed regions, with tensor deflection outputting more streamlines than Euler's approach, likely due to its ability of behaving rigidly when passing through crossing fiber regions.

### Probabilistic tractography

Probabilistic tractography was introduced as a way to overcome some of the limitations inherent to deterministic tractography. Unlike deterministic approaches, probabilistic tracking allows to quantify the uncertainty related with estimating brain connections. This uncertainty may stem from scanner noise, subject motion, multiple fiber populations within a voxel [2] and non-axon micro-structural

features contributing to the diffusion signal. Deterministic tractography assumes that these effects are negligible, opposite to probabilistic tracking which aims to account for the uncertainty caused by these noise sources.

To quantify the uncertainty of a connection, probabilistic tractography uses Monte Carlo based streamlines which are generated by propagating the front of a streamline using eq. (3.14) but instead of following the principal direction of the DT, a direction is sampled from a probability density function (PDF) which models the directional uncertainty of a fiber in a voxel. The stochastic sampling and streamline propagation continues until the streamline stopping criteria are met. Since the purpose of probabilistic tractography is to estimate the distribution of fibers which are achievable due to noisy conditions, every Monte Carlo streamline is repeated a large number of times.

Once all streamlines have been estimated, they are binarized into streamline count maps (3D images) using the number of streamlines entering a voxel, as a count reflecting connectivity between the voxel and the seed region voxels. The volumetric map is often the desired output of performing probabilistic tractography.

A key component of probabilistic tracking is the PDF of directional uncertainty which has to be estimated for each DT voxel. The PDFs are estimated as a calibration stage prior to probabilistic tractography using the approach of Parker et al. [118] implemented in the Camino software package [41]. The calibration works by generating a number of artificial DTs with differing eigenvalues from which DWI measurements are simulated. Noise is added to the simulated DWI measurements and the principal directions of the noise corrupted DWIs are estimated. By repeatedly adding noise to the simulated DWIs and estimating the principal directions, the directional uncertainty distribution (the PDF) is estimated for each of the artificially DTs, after which the PDFs are mapped back to the DTs of the original image data. The pre-calibration is achieved using the Camino routines of `dtlutgen` followed by `picopdf`. The routines require as input, the assumed SNR of the images set to 16 and the specification of a continuous PDF where we choose the Bingham distribution [20]. An alternative to this PDF is the Watson distributions described in [100] and [81]. The Bingham distribution is preferred since it allows a more general form of the directional probability distribution defined on the sphere. The Watson distribution can be considered as a special case of the Bingham distribution. The Watson distribution only allows circular probability functions defined on the sphere while the Bingham distribution allows elliptical probability functions. With no other information available about the more appropriate distributional form we prefer the more general distribution.

## Tractography parameters

Tractography methods usually require the following inputs parameters to be specified:

- 1) A seed region of voxels, where we expect the fiber bundle of interest to intersect. These voxel regions are often re-sampled if a denser streamline sampling is needed.
- 2) A set of criteria for terminating or excluding erroneous streamlines based on their expected geometric behaviour. An example of such a criterion is the angular threshold which terminates a streamline if it turns more than a specified number of degrees across a voxel. Similar criteria based on curvature and torsion are described in [13]. Streamline length is another geometric criteria used to exclude streamlines that do not fit the expected length requirements of a fiber bundle.
- 3) A set of way point masks indication regions of interests (ROI)s, used to exclude all streamlines not passing through them. Way point masks may also be used to as exclusion masks removing streamlines passing through the way points. Often a combination of inclusive and exclusive way point masks is needed to segment a fiber bundle.
- 4) A set of criteria for successfully terminating streamlines. The most common termination criterion of a streamline is based on FA. Once entering a region of low FA (for instance  $FA \leq 0.15$ ), streamline propagation terminates. Another possibility is to let the streamline run until it reaches the background, possibly indicated by a background mask.

## Example of deterministic tractography

The two methods of deterministic tractography (Euler's and tensor deflection), a seed regions of voxel and the FA streamline termination criteria of 0.15 were used to segment the left corticospinal tract (CST), shown in Figure 3.5. Figure 3.5(a)-(b) shows an example of tracking without additional inclusion masks causing a large number of streamlines which do not correspond with the expected appearance of the left CST. To remove false positive streamlines, two inclusion masks, an angular threshold criteria of 30 degrees and a minimum/maximum length criteria of 100/230 mm were used. Filtering the streamlines using these criteria resulted in the fiber bundle shown in Figure 3.5(c)-(d) which better reflects the expected appearance of the left CST.

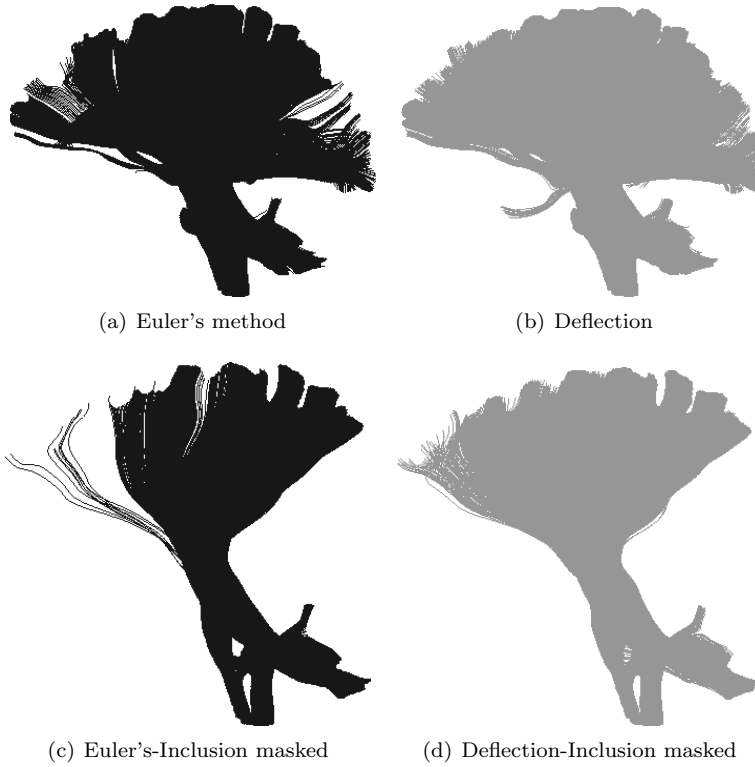


Figure 3.5: A visual comparison of Euler's method with the tensor deflection method, both used infer the fiber bundle of the left corticospinal tract. The top row of (a) and (b) compares the two methods using the same seed region but without any additional way point masks applied while the bottom row of (c) and (d) visually compares the two when two inclusion mask have been applied (One covering the pontine crossing region and one covering the superior corona radiata). Euler's method retained 8744 streamlines after applying the inclusion masks while the tensor deflection retained 11297 streamlines, reflection increased robustness of the tensor deflection towards proceeding through regions of crossing fibers near the corpus callosum.

## Example of probabilistic tractography

An example of probabilistic tractography is depicted in Figure 3.6(b)-(d), based on using 1000 streamlines per seed voxel, to estimate the connectivity index. The seed region used for this example is shown in Figure 3.6(a). This example was generated using a single DT model, a step-size of  $h = 0.5$  mm and a stopping criteria of  $FA=0.15$ . The example demonstrates a well known problem of tractography, namely that the probability of making a connection decreases with distance to the seed region which does not generally reflect reality.

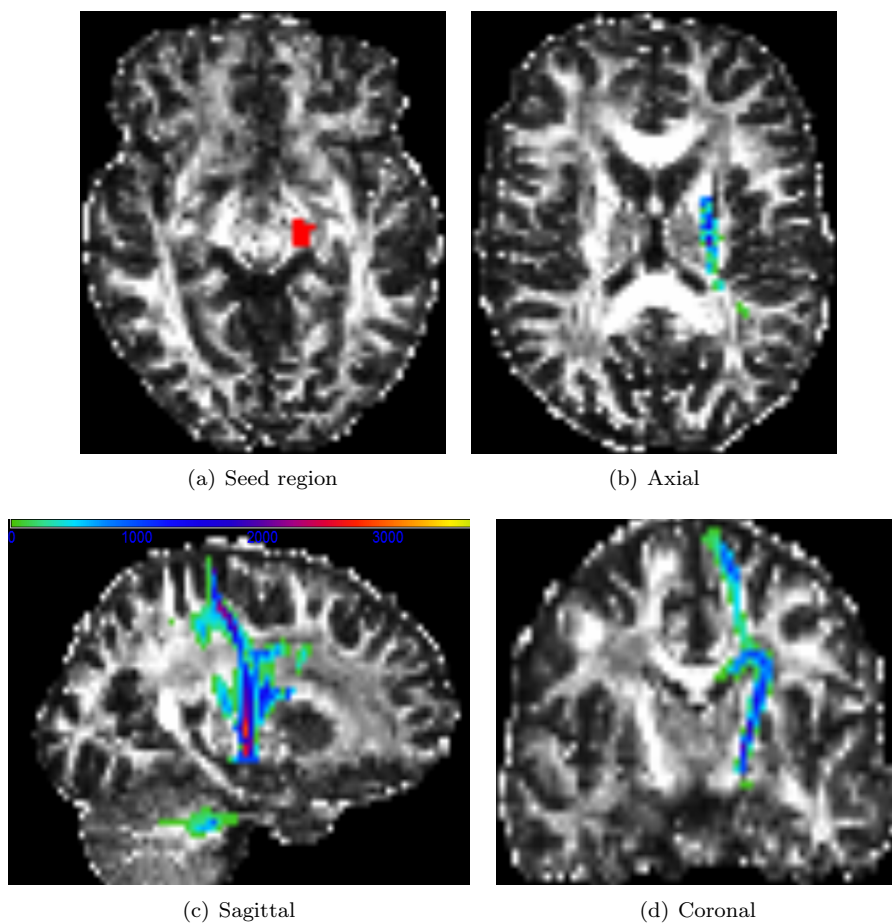


Figure 3.6: Probabilistic tractography visualized using the neurological convention. The tractography is based on 1000 Monte Carlo streamlines used to estimate the connectivity with respect to the seed region (a) of the right corticospinal tract. (b)-(d) shows the connectivity index as a heat map with larger values indicating strong connectivity. The seed and the connectivity indices are overlaid on the background of an FA image

### 3.6 Anatomical connectivity mapping

Anatomical connectivity mapping (ACM) was proposed by Embleton et al. [53] as a method for obtaining a voxel-wise measure of whole-brain structural connectivity. ACM and variations hereof have previously been used to study Alzheimer's disease [24], showing a decreased connectivity in the GM area of the Supramarginal Gyrus. A technique similar to ACM (not whole-brain but instead WM structure specific), has also been used to study the disease of amyotrophic lateral sclerosis (ALS) [34], a disease aggressively targeting motor neurons. They showed that the connectivity indices of the CST had a strong relation with the disease progression scores compared to FA which was better at distinguishing healthy subjects from ALS subjects. Most recently it has also been applied to RR-MS [25] to investigate how it relates with measures of cognitive impairment. We have used ACM in a group study of MS, suggesting a difference between the connectivity distributions across the entirety of WM between a healthy group of subjects and the MS patients. The results of this study are included in the contribution of chapter 10, where we also study the voxel-wise differences between two group of patients with the clinical diagnosis of RR-MS and SP-MS.

#### Estimating the ACM

Previous studies using ACM [53], [24], [25], have estimated the connectivity values of the ACM by seeding probabilistic tractography from all voxels of the brain and counting the number of times each voxel is hit by a streamline. Upon completion, the ACMs of these studies were spatially normalized to an atlas space enabling voxel-wise statistical analysis.

The estimation of ACM requires a seed mask for each subject and obviously, inconsistent cross subject masks will influence the values of the ACM, since an erroneously large mask will produce more streamlines while an erroneously small seed mask will produce fewer streamlines. Similarly, individual size and brain shape differences will alter the ACMs and if not accounted for, the ACMs will be biased by these differences, leading to changes in the values of the ACMs. The authors of [24] recognize the problem and suggest two different linear hit count normalizations, to compensate for overall cross subject brain size differences. While such approaches may work in practice, the size of the brains, the non-linear shape difference between the brains and erroneous seed masks are unlikely to cause changes of the ACM which are purely linear in nature.

We propose a modified estimation pipeline to overcome this problem which has some similarities with [29]. It avoids the need for individual seed masks and di-

rectly accounts for the non-linear shape and size variations across the brains of a study. The ACM of a subject is estimated using a three step pipeline; 1) A multi-tensor is fitted to the voxel-wise diffusion measurements using the approach described in section 3.4. 2) The multi-tensor volume is spatially normalized to the common atlas space (the FMRIB58 FA atlas of FSL) using a combination of the B-spline image registration of FSL [78](<http://fsl.fmrib.ox.ac.uk/fsl/fslwiki/>) and the preservation of principal direction algorithm [5]. 3) The ACM is estimated in this normalized space, through the probabilistic tractography method previously described. It uses a seed and stop criteria mask derived by thresholding the FMRIB58 FA atlas using the threshold  $FA > 0$  and the number of Monte Carlo streamlines per voxels is fixed to 500. This number was selected as a trade off, by balancing computational requirements against the statistical (stochastic) uncertainty of the ACM estimates. The choice of using 500 streamlines per voxel was based on the experiments described in the next section.

## Deciding the number of streamlines

To minimize the stochastic uncertainty of the connectivity values of an ACM it is important to choose a sufficiently large number of streamlines. To determine the number of streamlines we use an experimental approach based on repeated estimation of ACMs from five healthy subjects. The ACM of each subject is estimated five times for a fixed number of streamlines,  $nstreams = \{10, 50, 100, 150, 300, 500, 700\}$  and the voxel-wise coefficient of variation (CV) is calculated for each of the five subjects where CV is defined as the standard deviation divided by the mean. The uncertainty of an ACM estimate is calculated as the average CV across all voxels and can be expressed as a function of streamlines. The average CV function indicates the effect additional streamlines will have upon the estimated ACM and is inversely proportional to the signal to noise ratio (SNR).

The average CV function is plotted in Figure 3.7 and indicates an exponentially decreasing benefit of increasing the number of streamlines. The uncertainty function seems to converge, when using between 300-700 streamlines. As a consequence, 500 streamlines were used to estimate the ACMs of this thesis.

## An example

The appearance of an ACM, reflecting the anatomical whole-brain connectivity of a healthy subject is shown in Figure 3.8. The figure depicts an axial, a coronal and a sagittal slice. We notice a high anatomical connectivity in WM tracts and

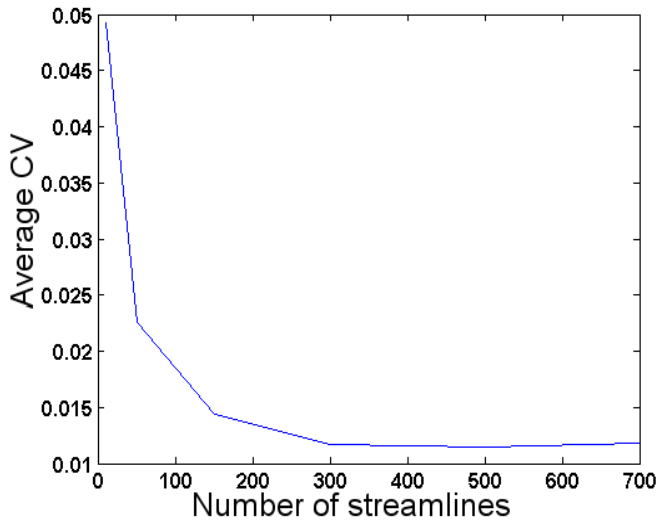


Figure 3.7: The average sample coefficient of variation (CV) for five repeated ACM estimations of five different healthy subjects. The average CV is shown as a function of the number of streamlines indicating a diminishing uncertainty for a large number of streamlines (above 300)

relative low connectivity in regions of CSF and GM. To the naked eye ACM may appear similar to FA but measures something very different as demonstrated in chapter 10, where group-wise analysis based on ACM and FA lead to widely different conclusions.

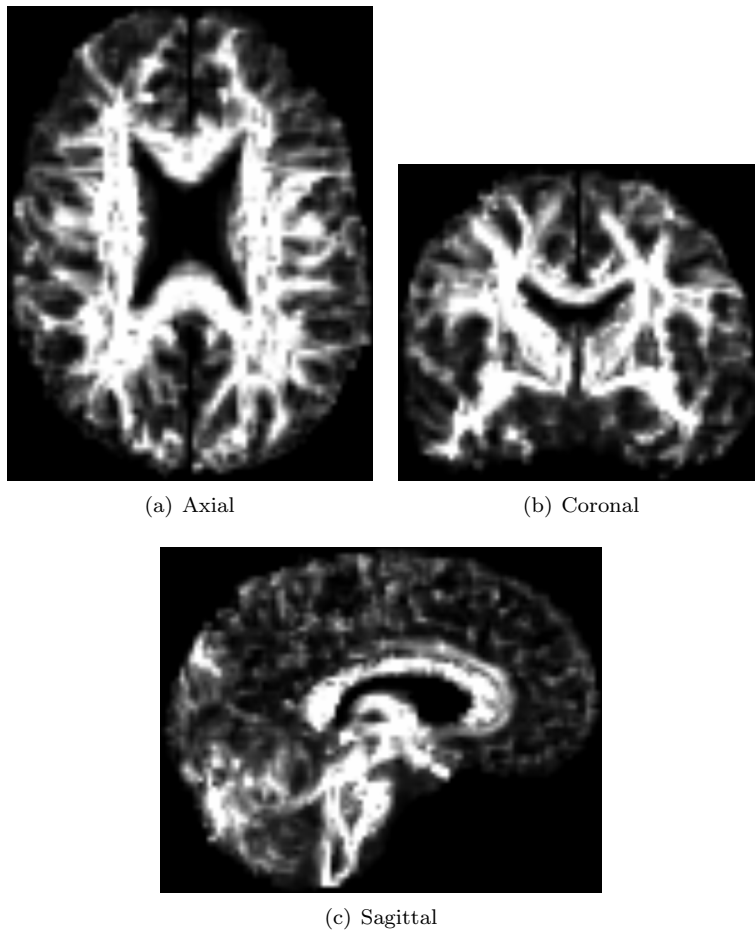


Figure 3.8: Shows an axial, a coronal and a sagittal slice of the ACM of a healthy subject visualized using the neurological convention.

### 3.7 Sheet-like models of white matter

One possible usage of a sheet-like model is as part of a pipeline performing group-wise, tract-oriented statistical analysis. This pipeline forms the basis of the paper in chapter 9. It is illustrated in Figure 3.9 and consist of; 1) building an atlas enabling cross subject correspondences, 2) modelling a WM tract using a sheet-like model and 3) performing statistical analysis to answer hypotheses with respect to a diffusion indices defined on the sheet-like model. The role of the sheet-like model is to supply a robust and consistent way of sampling diffusion indices along WM tracts and to supply an elegant way of visualizing diffusion indices along the sheet.

The sheet-like model is based on the continuous medial representation (cm-rep) suggested by Yushkevich et al. [175]. The cm-rep is a sheet-like surface-based model which is fitted to the binary representation of a WM tract such that the interior of the medial sheet-like surface-based model encompasses the streamlines of a WM tract. There is a one-to-one correspondence between points on the sheet and the surface which enables a sampling of diffusion indices along lines extending from the medial sheet to the surface. These lines are illustrated using a 2D binary object in the second box of Figure 3.9. The diffusion samples along these lines are usually averaged and projected onto the medial sheet location. Repeating the sampling for an entire study population, the subjects of which are assumed in correspondence enables statistical analysis and visualization of the diffusion indices as a function of the sheet position.

Before describing further details on the cm-rep, we shall briefly describe the background of alternative methods answering the same hypotheses as those answered using the tract-oriented analysis.

#### Alternative methods

The simplest methodological alternative to a cm-rep based analysis approach, is using a region of interest (ROI) based approach. The ROI-based approach use manual contouring of the WM tracts and performs cross subject voxel-based statistical analysis inside the ROI. Difficulties of this approach are that contouring is prone to errors, it is hard to determine the significance of the results due to the multiple comparisons problem and it may be hard to visualize the results of subsequent statistical analysis. An overview of ROI-based approaches is given in [140]. Problems due to contouring inaccuracies can be mitigated using a streamline based ROI approach [116]. This approach segments a WM tract using tractography and converts the streamlines into a binary ROI used for ROI-

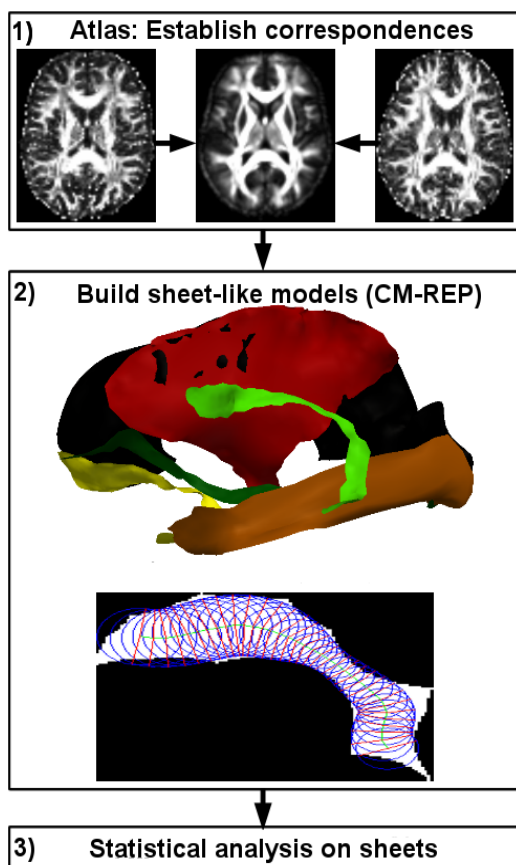


Figure 3.9: Illustrates a pipeline of the components involved in a cross subject tract-oriented study. The pipeline consist of; 1) building an atlas to enable cross subject correspondences, 2) estimating sheet-like models for each WM tract using cm-rep and 3) performing statistical analysis to answer tract specific hypothesis with respect to diffusion indices sampled using the sheet-like models.

based statistical analysis. However this approach still has difficulties due to the multiple comparisons problem. Further any false positive streamlines may cause erroneous ROI. These difficulties have led to more complex analysis approaches. Courouge et al. [42] and Goodlett et al. [70], proposed to quantify diffusion indices as a function of streamline arclength, enabling the diffusion indices of a fiber bundle to be projected onto a medial streamline yielding an averaged diffusion curve per WM tract, per subject allowing functional statistical analysis and visualization of diffusion indices as a function of arclength. The cm-rep can be considered as an extension of this idea by recognizing that many WM tracts are not tube-like but have shapes of sheet-like topology as demonstrated in [177]. A sheet-like model may be more accurate since the erroneous usage of tube-like models can lead to averaging diffusion indices coming from completely different areas of the tract.

Compared to the tract-oriented analysis approach, the approach of tract-based spatial statistics (TBSS) [138] is a popular alternative for doing sheet-like analysis of diffusion indices. TBSS estimates the medial sheet based on morphological operations from a thresholded average of study related FA images. Therefore its sheet is only a discrete approximation compared to the sheet of the cm-rep which takes the geometry of the tracts into account. Further TBSS does not know the surface of the WM tracts which limits analysis to diffusion indices that coincide with medial sheet. TBSS relies on image registration to establish cross subject correspondence which can be highly inaccurate therefore an ad-hoc strategy of searching for maximum FA values along lines perpendicular to the medial sheet for each individual subject. The outcome of such sampling strategy is to best our knowledge unknown in the vicinity of severe MS pathology.

## Estimating a sheet-like model

The estimation of a sheet-like model can be split in two parts, a tract segmentation part and a model fitting part. During the segmentation part, faithful binary segmentations of the WM tract are obtained. Each segmentation is found using tensor deflection tractography [88] which outputs streamlines that are turned into a binary volume. The binary volumes of several tracts have been concatenated into one volume, shown in the top box of Figure 3.10 where each volume is indicated by a different color. During the fitting part, the medial sheet-like model is estimated by fitting the cm-rep [175] to the binary segmentations of the WM tracts as shown in the lower box of Figure 3.10. Details on the segmentation of WM tracts and a formulation of the cm-rep model are given in the following sections.

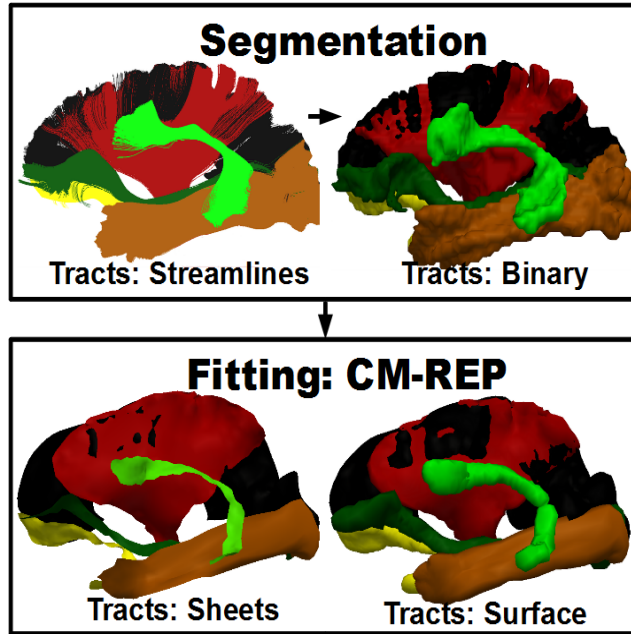


Figure 3.10: Illustrates the process of how the cm-rep is fitted to obtain sheet-like models of WM tracts. Fitting is done in two stages; 1) Tractography is used to segment the WM tracts (top box). The tracts segmented are the corpus callosum (black), the inferior longitudinal fasciculus (brown), the uncinate fasciculus (yellow), the superior longitudinal fasciculus (light green), the corticospinal tract (red) and the inferior fronto-occipital fasciculus (dark green). 2) The cm-rep is fitted to the binary representation of each WM tract, the result of which is shown in the bottom box.

## Segmenting tracts

The larger WM tracts of the brain are segmented. This includes the corpus callosum (CC), the corticospinal tracts (CST), the uncinate fasciculus (UNC), the superior longitudinal fasciculus (SLF), the inferior longitudinal fasciculus (ILF), inferior fronto-occipital fasciculus (IFO). The latter five are segmented both in the left and right hemispheres, giving a total of 11 WM tract segmentations.

The WM tract segmentations are estimated using the tractography algorithm of tensor deflection [88], using a step length of 0.5 mm, a streamline termination criteria of  $FA \leq 0.15$  and an angular termination criteria of 45 degrees. Streamlines are also disregarded based on their minimum or maximum lengths to get streamlines that are as spatially homogeneous as possible.

Streamlines are seeded within the entire brain of a tensor atlas and tract-specific ROI masks are used to include streamlines associated with a given WM tract. The specification of these masks follow the recommendations given by [109], as described in the following.

### *Corpus callosum:*

The CC is tracked using two inclusion masks, keeping only streamlines terminating in both the left hemisphere cortex and the right hemisphere cortex. The inclusion mask of one hemisphere covers a coronal mask intersecting the splenium, a coronal mask intersecting the genu and an axial mask positioned above the top part of the mid sagittal corpus callosum identified from an FA image. Asking for the structural connections between the two masks of the left/right hemisphere reconstructs the entire corpus callosum.

### *Corticospinal tract:*

To track the CST of a hemisphere, two inclusion masks are used to keep streamlines going through the pons and terminating in the area of the motor cortex. We further use an exclusion mask to exclude false positive streamlines proceeding into the opposite hemisphere of what is intended.

### *Uncinate fasciculus:*

To track the UNC of a hemisphere, two inclusion masks are delineated based on an FA image. The frontal lobe is identified in the coronal plane and the an inclusion mask delineated. The anterior temporal lobe is identified in the coronal plane and the second inclusion mask is delineated.

### *Superior longitudinal fasciculus:*

To track the SLF of a hemisphere, an inclusion mask is identified from an RGB image containing the principal directions in the red (left/right), green

(anterior/posterior) and blue (inferior/superior) channel. From an FA image additional inclusion masks are delineated. These masks are delineated using a coronal perspective to get rid of spurious cortical streamline projections. In 2002, Mori et al. [109] introduced this way of tracking the SLF. Since then research results have surfaced suggesting that the SLF should be divided into four sub-tracts [98] and that the tract which we denote superior longitudinal fasciculus (SLF) is indeed the tract known as the arcuate fasciculus. Nevertheless since we have based our segmentation on Mori's work we retain the naming convention.

*Inferior longitudinal fasciculus:*

To track the ILF of a hemisphere, which runs from occipital to the temporal lobe, two inclusion masks are delineated using the coronal orientation of an FA image. The first is delineated in a slice containing the occipital lobe and the second is delineated to include the mid-temporal lobe.

*Inferior fronto-occipital fasciculus:*

To track the IFO of a hemisphere that runs from the occipital to the frontal lobe, two inclusion masks are delineated using a coronal slice perspective of an FA image. The first one is delineated in a slice containing the occipital lobe and the second one is delineated from a slice depicting the frontal lobe.

The above specifications of inclusion/exclusion masks have been applied to segment both the left and right hemisphere tracts of the tensor atlas brain. The streamline representations segmented from using these ROIs are shown in the top box of Figure 3.10.

## The continuous medial representation

The continuous medial representation (cm-rep) approach was suggested by Yushkevich et al. [175] as an extension to a discrete medial-representation (m-rep) [122]. It is general approach for estimating a smooth medial sheet-like model of a binary image object with the assumption that the medial axis of the object poses sheet-like shape topology. The approach is therefore suitable for modelling WM tracts as many of these structures have sheet-like topology as demonstrated in [177]. We use the publicly available implementation of cm-rep which can be downloaded from <http://sourceforge.net/projects/cmrep/>, to estimate the models.

The cm-rep model is parameterized by the tuple  $m, r$  with  $m$  modelling the spatial loci of the sheet and  $r$  the associated radial field that makes up the surface of the model. The parameters of the sheet and the surface are estimated as to

maximize the overlap between the interior of the model and a binary image while enforcing regularity conditions on the model. Adopting the notation of [128] we let  $M : \mathbb{R}^3 \rightarrow \mathbb{R}^1$  denote an image assumed to be +1 inside and -1 outside the binary object. The cm-rep model is optimal when it minimize the cost function

$$f(m, r) = 1 - (1/V_c) \int_C M(x) \partial x + \sum_{i=1}^n w_i \int_C T(x) \partial x. \quad (3.16)$$

The first integral of eq. (3.16) denotes the image matching energy where  $C$  is the interior domain of the model. The second term of eq. (3.16) sums over  $n$  model priors which are weighted according to  $w_i$  the weights are determined experimentally. The integral of the image matching term is approximated through numerical integration by sampling  $M$  along the spoke positions given by

$$x(m, r, \xi) = \begin{cases} m + \xi \cdot r \cdot (-\nabla_m r + \sqrt{1 - |\nabla_m r|^2} \cdot N_m), & \xi > 0 \\ m - \xi \cdot r \cdot (-\nabla_m r - \sqrt{1 - |\nabla_m r|^2} \cdot N_m), & \text{otherwise} \end{cases} \quad (3.17)$$

The integral of eq. (3.16) is evaluated by discretization of  $\xi \in [-1, 1]$ , the range of which determines the interior of the surface-based model and  $\xi > 0$  refers to one side of the sheet and  $\xi < 0$ , the other side. When  $\xi = 1$  or  $\xi = -1$  the spatial coordinates are on the boundary of the surface-based model. the variable of  $N_m$  denotes the unit normal at  $m$  and  $\nabla_m r$  is the Riemannian gradient.

#### *Making the model continuous:*

To give the model a continuous basis rather than a discrete basis, the authors of [175] suggested to model  $r$  and  $m$  as B-spline functions parameterized over a 2D domain, given by the implicit  $(u, v)$  coordinate system. In this case, the radial field takes on the continuous form  $r(u, v) : \mathbb{R}^2 \rightarrow \mathbb{R}^1$  and the radii for any  $(u, v)$  coordinates are given by the spline

$$r(u, v) = \sum_{j=1}^{n_1} \sum_{k=1}^{n_2} b_j(u) b_k(v) w_{jk} \quad (3.18)$$

The spatial coordinates of the sheet are similarly defined by the mapping  $m(u, v) : \mathbb{R}^2 \rightarrow \mathbb{R}^3$  using the B-spline form

$$m^{(i)}(u, v) = \sum_{j=1}^{n_1} \sum_{k=1}^{n_2} b_j(u) b_k(v) w_{jk}^{(i)}, \quad (3.19)$$

where  $i$  denotes the  $i$ th spatial dimension of  $m$ . To use a continuous model, requires an estimate of the mapping which takes us from the  $(u, v)$  coordinates to  $m(u, v)$ . The mapping is supplied by the maximum variance unfolding (MVU) [164] technique, which creates a mapping from the high dimensional input vectors to some low dimensional Euclidean vector space. The MVU searches

for the mapping that preserves the original Euclidean distances of the higher dimensional space also, in the lower dimensional space. Therefore applying the MVU technique, gives the 3D to 2D mapping with the least Euclidean distortion of a localized neighbourhood of the original higher dimensional data. By introducing the splines into eq. (3.17), the cost function in eq. (3.16) can be expressed a function of the B-spline parameters. The optimal parameters for the cost function are estimated by minimizing the cost function using a brute force evolutionary optimization method [104].

Several advances for extending the model have been suggested in literature, for instance by formulating the problem as a partial differential equation [176] or using a different continuous representation for the model. These options haven't been explored during the thesis.

#### **Model priors:**

The model priors of the cost function in eq. (3.16) are designed to penalize undesired model behaviour. We shall only give a brief explanation of the model priors and the effects they exact on the model. A more detailed description can be found in [128].

##### *Medial regularity constraint (medReg):*

This prior enforces regularity of the medial sheet  $m$  by penalizing distortion in the area element of the triangular mesh that make up the sheet. It does so by maintaining a geometric correspondence between the initial medial sheet and the medial sheet during the fitting process.

##### *Boundary curvature constraint (bCurv):*

This prior penalize high curvature on the boundary of the model, thereby enforcing a smooth model.

##### *Boundary jacobian constraint (bJac):*

This prior term, prevents the boundary from crossing itself as a result of the fitting process. Effectively achieved by penalizing if a boundary point of the model lies inside one of the spheres given by  $m, r$ . This term enforce that the inequalities of  $|b_k^+ - m_j| > r_j$  and  $|b_k^- - m_j| > r_j$  should hold for the  $m_j$  position with respect to all the boundary positions  $b_k$  of the model.

##### *Radial thickness constraint (rReg):*

The radial thickness prior, prevents the radial field  $r$  from becoming very small. As the radii in  $r$  goes to zero this penalty term goes to infinity.

##### *Medial angles constraint (mAng):*

This term controls the quality of the medial mesh  $m$ , penalizing if the angles of the triangles in  $m$  become excessively small.

Tract	medReg	bCurv	bJac	rReg	mAng	bAng	bGrad	tVal
CC	0.1	0.0	0.01	0.00001	75	75	10000	0.01
CST-L	0.0015	0.0	0.01	0.00009	125	125	10000	0.01
CST-R	0.0015	0.0	0.01	0.00012	125	125	10000	0.01
SLF-L	0.5	0.0	0.01	0.0009	350	100	5000	0.01
SLF-R	0.5	0.0	0.025	0.00085	350	450	8000	0.01
ILF-L	0.0015	0.0	0.01	0.00009	150	100	5000	0.01
ILF-R	0.1	0.0	0.01	0.00001	75	50	4500	0.01
UNC-L	0.1	0.0	0.015	0.0001	100	50	5000	0.01
UNC-R	0.1	0.0	0.015	0.0001	100	50	5000	0.01
IFO-L	1.0	0.0	0.01	0.0002	1250	475	9000	0.01
IFO-R	1.0	0.0	0.012	0.0003	100	850	9500	0.01

Table 3.1: List the weights of the model priors in the cost function of eq. (3.16), which are used to fit the cm-reps. The weights are shown for 11 different WM tracts. Each row of the table, correspond to a different WM tract while each column lists the model prior weights.

*Boundary angles constraint (bAng):*

This term controls the quality of the surface boundary mesh  $b$ , penalizing if the angles of the triangles become excessively small.

*Boundary gradient constraint (bGrad):*

This prior ensures that the Riemannian gradient  $\nabla_m r$  has magnitude close to 1 at the edge of the medial sheet which according to eq. (3.17) removes the influence of the surface normal when estimating spoke directions at the edge. The spoke directions at the sheet edge will thus correspond approximately to  $\nabla_m r$ .

*Tangent validity constraint (tVal):*

This prior safeguards a problem that may occur when estimating gradients at the edge of the medial sheet where it may happen that  $\nabla_u m$  is almost parallel to  $\nabla_v m$ . These should not be parallel and thus the term penalize if the angles between the two partial derivatives are small.

The models are fitted using all of these prior terms , weighted according to  $w_i$  of eq. (3.16). The weights used to fit the cm-rep, to the binary segmentations of the 11 WM tracts, are specified in Table 3.1.

**Avoiding local cost function minima:**

The cost function of eq. (3.16) may contain several minima that could lead to an optimization method finding a suboptimal set of spline parameters. One way of

avoiding local minima solutions is by making the cost function smoother. This can be done by smoothing the binary image  $M(x)$  using a Gaussian function with zero mean and smoothing scale given by its standard deviation. Smoothing has the effect of removing noise and small scale image details. The cm-rep model is fitted at a fixed number of smoothing scales, a strategy denoted as multi-scale fitting where the cm-rep model is estimated at a smoother scale is used as the starting point for estimating the model at a less smooth scale. As previously mentioned, the cm-rep model is fitted using an optimization strategy described in [104].

## Results

A separate cm-rep model was fitted to individual binary representations of each WM tract of the CC, the CST, the UNC, the SLF, the ILF and the IFO. These were represented at three different scales for the purpose of multi-scale fitting, given by the standard deviations of  $\sigma=(2\text{ mm}, 1\text{ mm}, 0.8\text{ mm})$ . To obtain a good starting guess from which to start the fitting, a previously published cm-rep atlas [177] was used. Having a good starting guess for  $m$  and  $r$  decreases the possibility of local minima and ensures faster convergence.

The results of fitting all the sheet-like models are shown in Figure 3.11. It shows the surface of a cm-rep model in yellow and the binary target image (not smoothed) in purple.

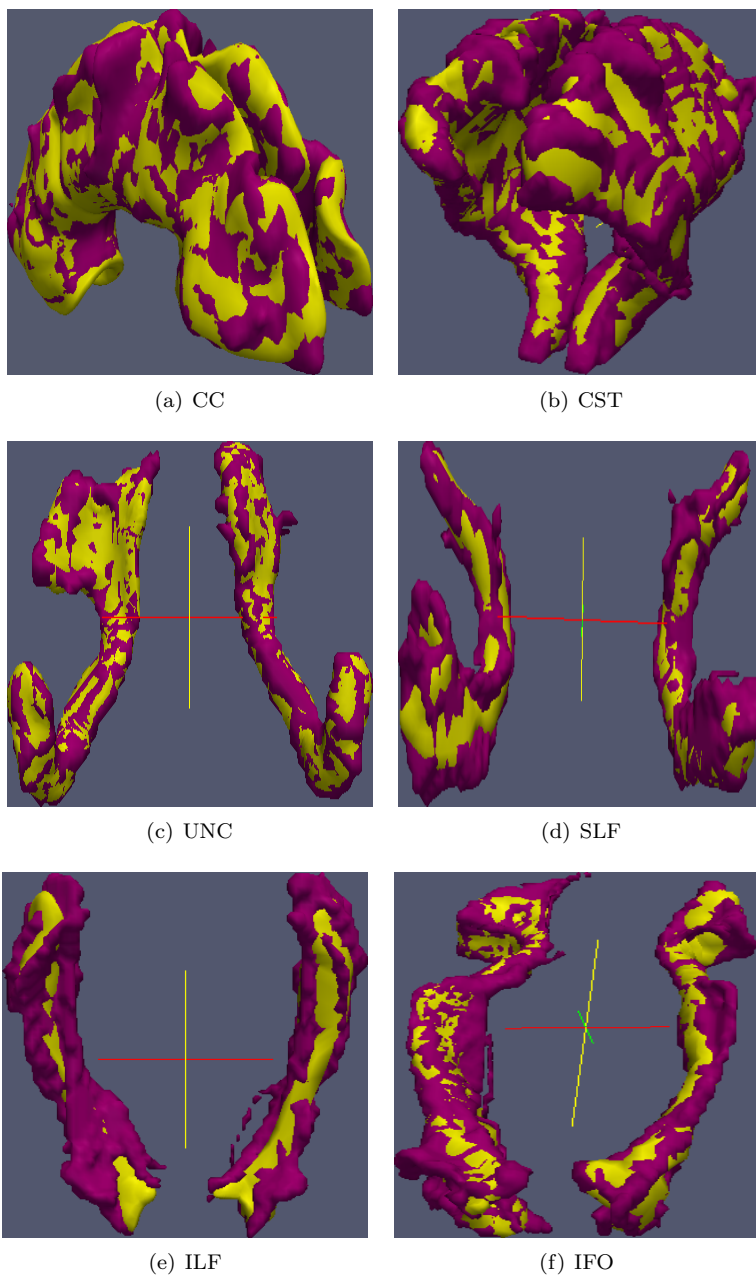


Figure 3.11: Shows the binary representations of WM tracts (purple) and the fitted cm-rep models (yellow) for the CC, the CST, the UNC, the SLF, the ILF and the IFO. Visualized using the neurological convention



# Image Registration

---

## 4.1 Introduction

The purpose of image registration is to bring the discrete image representation of two or more objects into the same space of meaningful correspondence. If we choose the image  $F(x)$  as a fixed image of reference and  $M(y(x))$  as the moving image the objective of image registration is to determine the spatial deformation  $y(x)$  that ensures

$$F(x) \approx M(y(x)). \quad (4.1)$$

To solve an image registration problem several components are required. 1) An image interpolation scheme giving continuous support of an image, 2) a similarity measure quantifying how similar  $M(y(x))$  is to  $F(x)$ , 3) a deformation model specifying how to deform the coordinates of the moving image and 4) an optimization algorithm searching for the deformation which optimizes the similarity measure. These four components will be introduced during section 4.2. Section 4.3 proceeds to introduce a non-parametric image registration approach known as Thirion's demons which has been applied in chapter 8, as a technique for correcting geometric image distortions. The last sections of this chapter will cover high dimensional image registration with application to diffusion tensor models, thus in section 4.4 we introduce two common strategies used to deform

diffusion tensors (DT) when the deformation is known. This naturally leads to section 4.5 where a method for high dimensional image registration is described. Finally section 4.6, introduces methodology for building population specific atlases useful for voxel-based (localized) cross subject statistical analysis. The atlas building strategy applies to scalar image registration approaches as well as high dimensional registration techniques.

## 4.2 Methodology

### 4.2.1 Image interpolation

To enable the deformation of an moving image  $M$ , requires the evaluation of  $M$  at spatial grid coordinates which do not coincide with the grid coordinates of the image. Conceptually, this can be achieved by modelling the image intensities as a continuous function across the image domain. Such that the image is described by the functional mapping  $M(p) : \mathbb{R}^d \rightarrow \mathbb{R}^1$  which evaluates the spatial coordinate  $p$  and outputs the intensity value  $M(p)$ . This mapping is commonly referred to as an image interpolation function. For reasons of efficiency, the linear interpolation function is highly popular. When  $d = 3$ , the (tri)-linear interpolation function is given by

$$\begin{aligned}
 M(p) = & M(x_0, y_0, z_0) \cdot \epsilon_1 \cdot \epsilon_2 \cdot \epsilon_3 \\
 & + M(x_1, y_0, z_0) \cdot (1 - \epsilon_1) \cdot \epsilon_2 \cdot \epsilon_3 \\
 & + M(x_0, y_1, z_0) \cdot \epsilon_1 \cdot (1 - \epsilon_2) \cdot \epsilon_3 \\
 & + M(x_0, y_0, z_1) \cdot \epsilon_1 \cdot \epsilon_2 \cdot (1 - \epsilon_3) \\
 & + M(x_0, y_1, z_1) \cdot \epsilon_1 \cdot (1 - \epsilon_2) \cdot (1 - \epsilon_3) \\
 & + M(x_1, y_0, z_1) \cdot (1 - \epsilon_1) \cdot \epsilon_2 \cdot (1 - \epsilon_3) \\
 & + M(x_1, y_1, z_0) \cdot (1 - \epsilon_1) \cdot (1 - \epsilon_2) \cdot \epsilon_3 \\
 & + M(x_1, y_1, z_1) \cdot (1 - \epsilon_1) \cdot (1 - \epsilon_2) \cdot (1 - \epsilon_3)
 \end{aligned} \tag{4.2}$$

where  $M(p)$  becomes a distance weighted average of the voxel intensities found at the 8 nearest integer grid positions. The weights of  $\epsilon_1, \epsilon_2, \epsilon_3$  reflects the relative influence of the intensities at the nearest voxels, and are estimated by  $\epsilon_i = \Delta(i)/(h(i))$ , with  $h$  corresponding to the voxel-wise spacings and  $\Delta(i)$  is the distance to the nearest integer grid position along the  $i$ th dimension. The formula of eq. (4.2) can be simplified to lower ( $d=1$  or  $d=2$ ) and generalized for higher dimensionality as done in [108]. Other popular choices of image interpolation functions are the cubic [76], [84] and sinc interpolations [154] which generally result in smoother functions, however these choices usually come at

the cost of significantly increased computational requirements. The nearest neighbour interpolation is not used for image registration problems, since this function is non-continuous across voxels, however it is often used to deform images containing region of interests, that needs to be deformed similarly to a moving image.

### 4.2.2 Similarity measures

To align the two images  $M$  (moving image) and  $F$  (fixed image) based on their intensities, a definition of optimality  $\phi$  is required. This optimality measure is expressed using the following integral

$$D(M, F) = \int_{\Omega} \phi(M(y(x)), F) dx, \quad (4.3)$$

where  $\Omega$  denotes the region of interest within the imaging domain and  $y$  is the function deforming the spatial domain as to rearrange the voxels of  $M$ . The goal of image registration is to determine  $y$  as to achieve an optimal value of  $D(M, F)$ , however there are several ways of specifying  $\phi$ , the appropriate choice depending on the images being registered. For images of the same modality, acquired on the same scanner, specifying  $\phi$  as the sums of square difference (SSD) is sufficient while different modalities and or different scanners require more complex similarity measures, such as cross correlation, correlation ratio [107], [108] or mutual information (MI) [37], [158].

#### Sums of square differences

Using a sums of square difference (SSD) metric leads to the discrete similarity measure

$$D^{SSD}(M, F) = \frac{1}{2} \int_{\Omega} (M(y(x)) - F)^2 dx \approx \frac{1}{2} \cdot h \sum_i (M(y(x_i)) - F(x_i))^2, \quad (4.4)$$

where  $h$  is the size of a volume element of a voxel, according to the midpoint quadrature rule [64]. It is implicitly assumed that  $R = M(y) + \epsilon$ , with the noise  $\epsilon$  assumed to be Gaussian distributed with zero mean and unknown variance.

A key feature of this similarity measure is the existence of the Gateaux derivative [108] which is

$$\nabla D_i^{SSD}(M, F) = h \cdot \nabla M(y(x_i)) \cdot (M(y(x_i)) - F(x_i)). \quad (4.5)$$

This makes it possible to find the optimal  $y$  of an SSD similarity measure using gradient based optimization methods.

### Mutual information

Mutual information (MI) was introduced by [158] as a similarity measure for image registration. It is a statistical measure indicating how much is known about a voxel in  $M$  given knowledge of the corresponding voxel in  $F$ . It is defined as

$$D^{MI}(M, F) = H(p(M)) + H(p(F)) - H(p(M, F)). \quad (4.6)$$

$H(p(M))$  and  $H(p(F))$  are the marginal entropies of the probability distribution of the image intensities, similarly  $H(p(M, F))$  is the entropy for the joint probability of the two images.  $H(p)$  denotes Shannon's definition of entropy [136] and quantifies the concentration of probability as calculated in a discrete setting by

$$H(p) = \sum_i p(i) \cdot \log(p(i)), \quad (4.7)$$

where the index  $i$  sums over all possible bins of the probability density. The marginal and joint probability densities are estimated from normalized histograms as in the following equation,

$$p(j) = \frac{hist(j)}{\sum_j^n p(j)} \text{ and } p(j, k) = \frac{hist(j, k)}{\sum_j^n \sum_k^n p(j, k)}. \quad (4.8)$$

The  $n$  number of bins in which to divide the intensity range of the images for estimating normalized histograms, is decided by the user and  $n$  need not be the same for  $F$  and  $M$ .

To improve the robustness of the MI measure [143] suggested the normalised mutual information (NMI). NMI was experimentally shown able to increase the robustness of image registration when images have varying field of views. The NMI similarity measure is evaluated by

$$D^{NMI}(M, F) = \frac{H(p(M, F))}{H(p(M)) + H(p(F))}, \quad (4.9)$$

and is usually the preferred cost criteria when performing multi modal image registration.

### 4.2.3 Deformation models

It is generally assumed that the deformed coordinates of  $y(x)$  can be expressed as,

$$y_i(x_i) = T(x_i) + u(x_i), \quad (4.10)$$

where  $x_i$  is the coordinate vector of the  $i$ th grid position,  $T$  denotes a global scale deformation model typically modelled using a rigid or an affine model while  $u$  is a small scale localized displacement field of non-rigid nature. When the deformation is only due to rigid motion, the non-rigid part may not be part of the image registration problem and  $u = 0$ .

### The rigid model

It is the choice of model when spatially aligning images of the same object but under the assumption that the difference between the  $M$ ,  $R$  images is purely due to rigid motion. This is often the case in MRI examinations where several images of the same subject are acquired during a single examination.

A proper rigid coordinate deformation must preserve Euclidean angles and length after the deformation. The deformation model performs the spatial co-ordinate mapping  $\varphi : \mathbb{R}^d \rightarrow \mathbb{R}^d$  and for  $d=3$ , the rigid model that deforms the vector  $x_i = [x \ y \ z]^T$  is given by

$$\begin{aligned}
 y_i &= R \cdot x_i + t = R(\phi_x)R(\phi_y)R(\phi_z) \cdot x_i + [t_x \ t_y \ t_z]^T, \\
 R(\phi_x) &= \begin{pmatrix} 1 & 0 & 0 \\ 0 & \cos(\phi_x) & -\sin(\phi_x) \\ 0 & \sin(\phi_x) & \cos(\phi_x) \end{pmatrix} R(\phi_y) = \begin{pmatrix} \cos(\phi_y) & 0 & \sin(\phi_y) \\ 0 & 1 & 0 \\ -\sin(\phi_y) & 0 & \cos(\phi_y) \end{pmatrix} \\
 R(\phi_z) &= \begin{pmatrix} \cos(\phi_z) & -\sin(\phi_z) & 0 \\ \sin(\phi_z) & \cos(\phi_z) & 0 \\ 0 & 0 & 1 \end{pmatrix}.
 \end{aligned} \tag{4.11}$$

Three consecutive rotations are followed by 3 translations resulting in a 6 parameter model. Due to its low dimensional nature, this model is often estimated using none gradient based optimization methods.

### The affine model

The 3D affine model is a 12 parameter model with 6 parameters corresponding to those of the rigid model, 3 additional parameters are used to model the shearing of an image and the last 3 parameters model the scale. A formulation

of the model for deforming the  $x_i$  coordinates is

$$y_i = R \cdot Z \cdot S \cdot x_i + t$$

$$S = \begin{pmatrix} s_x & 0 & 0 \\ 0 & s_y & 0 \\ 0 & 0 & s_z \end{pmatrix} \quad Z = \begin{pmatrix} 1 & z_1 & z_2 \\ 0 & 1 & z_3 \\ 0 & 0 & 1 \end{pmatrix}. \quad (4.12)$$

$S$  is the scaling matrix,  $Z$  is the shearing matrix while  $t$  and  $R$  are given in eq. (4.11). The model can also be formulated directly as a 12 parameter linear deformation model expressed in the following matrix form

$$y_i = Q(x_i) \cdot w \quad (4.13)$$

$$= \begin{pmatrix} x_{i1} & x_{i2} & x_{i3} & 1 & 0 & 0 & 0 & 0 & 0 & 0 & 0 & 0 \\ 0 & 0 & 0 & 0 & x_{i1} & x_{i2} & x_{i3} & 1 & 0 & 0 & 0 & 0 \\ 0 & 0 & 0 & 0 & 0 & 0 & 0 & 0 & x_{i1} & x_{i2} & x_{i3} & 1 \end{pmatrix} \begin{pmatrix} w_1 \\ \vdots \\ w_{12} \end{pmatrix}$$

where the subscript index  $ix$  denotes the  $xth$  dimension of the  $ith$  voxel while  $[w_1 \dots w_{12}]^T$  are the 12 parameters of the affine model. This formulation is popular for gradient based optimizer due to its simple linear form. On the other hand, the explicit formulation in eq. (4.12) benefits from direct access to the rotation/translation/shearing and scaling parameters.

## Flexible deformation models

The class of locally flexible deformation models belong to the family of non-rigid deformations which change the shape of an object such that Euclidean distances and angles are no longer preserved between the original and the deformed object. A highly flexible model is usually the choice of model when attempting to establish correspondences between different subjects. However it has a wide range of applications, for instance it has been used to do MRI artefact corrections [73], assessing longitudinal brain changes [139] and providing an initialisation for automated tissue segmentation [38], [156].

A very popular model is the free form deformation (FFD) model introduced by Ruckert et al. [134]. This model is based on multivariate splines and for the 3D

mapping  $u(x_i) : \mathbb{R}^3 \rightarrow \mathbb{R}^3$  it is given by

$$\begin{aligned}
 y_{i1} &= x_{i1} + \sum_{j=1}^{n_1} \sum_{k=1}^{n_2} \sum_{l=1}^{n_3} b_j(x_{i1}) b_k(x_{i2}) b_l(x_{i3}) w_{jkl}^1 \\
 y_{i2} &= x_{i2} + \sum_{j=1}^{n_1} \sum_{k=1}^{n_2} \sum_{l=1}^{n_3} b_j(x_{i1}) b_k(x_{i2}) b_l(x_{i3}) w_{jkl}^2 \\
 y_{i3} &= x_{i3} + \sum_{j=1}^{n_1} \sum_{k=1}^{n_2} \sum_{l=1}^{n_3} b_j(x_{i1}) b_k(x_{i2}) b_l(x_{i3}) w_{jkl}^3 \quad (4.14) \\
 b(x) &= \begin{cases} (x+2)^3, & -2 \leq x < -1 \\ -x^3 - 2(x+1)^3 + 6(x+1), & -1 \leq x < 0 \\ x^3 + 2(x-1)^3 - 6(x-1), & 0 \leq x < 1 \\ (2-x)^3, & 1 \leq x < 2 \end{cases}
 \end{aligned}$$

The deformation of a voxel along a given direction is found as the sum of a voxels spatial coordinate  $x_i$  and the displacements of the cubic B-spline where the value of the B-spline is given by a linear combination of basis functions  $b(x)$  and their affiliated parameters in  $w^1, w^2, w^3$ . The number of basis functions  $(n_1, n_2, n_3)$  along each dimension determines the flexibility of the model so that more basis functions yield increasing flexibility. The centre of the basis functions are usually positioned equidistantly throughout the image domain, achieved by translating and scaling the basis functions of eq. (4.14).

Another popular approach (especially in neuroscience) is to model the deformation using a low order discrete cosine transformation (DCT) [10], as expressed in eq. (4.15)-(4.16)

$$\begin{aligned}
 y_{i1} &= x_{i1} + \sum_{j=1}^m \sum_{k=1}^m \sum_{l=1}^m d^{[j]}(x_{i1}) d^{[k]}(x_{i2}) d^{[l]}(x_{i3}) w_{jkl}^1 \\
 y_{i2} &= x_{i2} + \sum_{j=1}^m \sum_{k=1}^m \sum_{l=1}^m d^{[j]}(x_{i1}) d^{[k]}(x_{i2}) d^{[l]}(x_{i3}) w_{jkl}^2 \quad (4.15) \\
 y_{i3} &= x_{i3} + \sum_{j=1}^m \sum_{k=1}^m \sum_{l=1}^m d^{[j]}(x_{i1}) d^{[k]}(x_{i2}) d^{[l]}(x_{i3}) w_{jkl}^3.
 \end{aligned}$$

The user specifies the desired number of basis functions  $m$ , with higher  $m$  yielding increasingly oscillating functions. The DCT basis functions  $d^{[j]}(x)$  are de-

fined,

$$\begin{aligned}
 k &= \frac{x_{iq} - \min(x_{:q}) + 1}{\max(x_{:q}) - \min(x_{:q})} \\
 d^{[1]}(x_{iq}) &= \frac{1}{\sqrt{n}}, n = \text{length}(x_{:q}) \\
 d^{[j]}(x_{iq}) &= \sqrt{\frac{2}{n}} \cdot \cos\left(\frac{(\pi \cdot k - 1)(j - 1)}{2 \cdot n}\right)
 \end{aligned} \tag{4.16}$$

where  $q = \{1, 2, 3\}$  indexes the dimension, such that  $k$  becomes an integer lying in the range  $[1:n]$  where  $n$  is the size of the  $q^{th}$  image dimension. To evaluate  $d^{[j]}(x_{iq})$  for an image grid position  $i$ , the value  $k$  must first be determined. This  $k$  is inserted into the cosine expression which allows to evaluate the basis function value at  $i$ .

The two deformation models of FFD and DCT are widely used in registrations involving brains, due to their implementation in software tools such as FSL [139] (<http://fsl.fmrib.ox.ac.uk/fsl/fslwiki/>) and SPM [10] (<http://www.fil.ion.ucl.ac.uk/spm/>). The DCT is often thought to be more constrained since it is usually only evaluated for lower orders thus it is not expected to have the same flexibility as the FFD, however it has been argued in [10] that only low order deformations are required for image registration of brains. A 1D illustration of both the FFD(8 basis functions) and DCT( $m=7$ ) is shown in figure 4.1. Since both models have a linear parametrization, they are differentiable and gradient based optimization made possible.

Other highly flexible deformation models are the thin plate splines [21] and multivariate lower order polynomials [172]. A more recent suggestion is to use polyrigid or polyaffine models [8]. Model free alternatives also exists however such approaches lack the constraints imposed by a parametric model thereby increasing the possibility of unrealistic deformations. Regardless of the model, image registration leads to ill posed optimization problems. Addressing this problem, is done by regularization, the topic of the next section.

#### 4.2.4 Regularization

Image registration based solely on similarity measures is inherently ill-posed: For every spatial location  $x_i$  one is asking for a higher dimensional function  $u(x) : \mathbb{R}^d \rightarrow \mathbb{R}^d$ , to be estimated from the scalar intensity information only. In general there are many different deformation fields which could yield the same similarity measure optimum. The standard way to address an ill-posed problem, is to regularize, by modifying the problem stated in eq. (4.3) such that

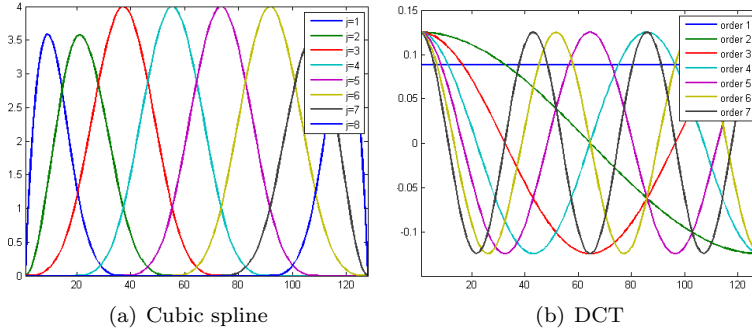


Figure 4.1: Shows the basis functions of the B-spline deformation model and the discrete cosine transformation (DCT). For simplicity these are shown in 1D. The domain ranges from  $[1:128]$  thus using 8 B-spline basis functions results in a spacing distance of 16 between each of the basis function. The DCT is visualised using 7 basis function

the solution space is constrained to containing fewer local minima (ideally just one). The modified problem to solve is

$$D(M, F) = \int_{\Omega} \phi(M(y(x)), F) + \lambda S(u(x)) dx \quad (4.17)$$

From a mathematical point of view, the regularizer denoted by  $S(u(x))$  should make the registration problem well-posed and turn the problem into a convex function. In practice even the modified (regularized) similarity measure will allow for many local minima, and the results will depend on a good starting point for registration process and the right choice of  $\lambda$ . Two popular regularizers which are available from most image registration tool-kits and have been used during this thesis are the membrane energy also called diffusion energy and the bending energy.

In a discretize setting the membrane energy is given by

$$S(u(x)) = \sum_i \sum_{j=1}^3 \sum_{k=1}^3 \left( \frac{\partial u_{ji}}{\partial x_{ki}} \right)^2 \quad (4.18)$$

and is the summation of the deformation field derivatives squared with respect each of to the 3 directions. This has the effect of penalising extreme local stretching/compression of the deformation model. The bending energy imposes similar constraints on the deformation model but also penalize curvature and is

given by

$$S(u(x)) = \sum_{k=1}^3 \sum_{i=1}^3 \left( \frac{\partial^2 u_{ki}}{\partial^2 x_{1i}} \right)^2 + \left( \frac{\partial^2 u_{ki}}{\partial^2 x_{2i}} \right)^2 + \left( \frac{\partial^2 u_{ki}}{\partial^2 x_{3i}} \right)^2 + \quad (4.19)$$

$$2 \left[ \left( \frac{\partial^2 u_{ki}}{\partial x_{1i} \partial x_{2i}} \right)^2 + \left( \frac{\partial^2 u_{ki}}{\partial x_{1i} \partial x_{3i}} \right)^2 + \left( \frac{\partial^2 u_{ki}}{\partial x_{2i} \partial x_{3i}} \right)^2 \right]$$

These types of regularization (membrane and bending energies), may seem ad hoc but are meaningful from a physical point of view. It makes sense that two neighbouring voxels of the same tissue would experience similar types of deformation. The estimation of 1st and 2nd order derivatives of the field is elaborated upon in [10] and depends on the choice of deformation model but in case of the FFD and DCT models previously presented, it boils down to taking the derivatives of the basis functions.

### 4.2.5 Optimization

The purpose of optimization methods is to either minimise or maximise a problem usually stated in the form of a cost function, such as eq. (4.17). In the context of image registration problems, the optimization aims to find deformation model parameters minimizing the unconstrained cost functions specified through the similarity measures of eq. (4.4)-(4.9) or in case of ill-posed problems eq. (4.17). We can widely classify the optimization algorithms used for image registration in two groups. Algorithms that do not need gradients and those that require gradients. Due to time complexity issues, the first group is used to solve small scale problems with a low number of parameters as opposed to the second group which solves large scale problems with a high number of parameters.

#### Small scale problems

If the number of parameters is low, search based optimization methods are suited for estimating parameters, thus these type of methods are used with rigid and affine deformation models. The general concept of the optimization methods is to search the parameters space by adjusting each parameter in turn until no further change is observed in the cost function similarity measure. Most search based methods are more intelligent than this description recognizing that such an approach could lead to a huge number of function evaluation before an optimum is found. The key to these method is in learning appropriate search

direction based on previous iterates. Powell's method [129] is the method used during this thesis (also used by SPM8) however any properly calibrated search method could potentially solve small scale problems [111], [74].

### Large scale problems

If the number of parameters is high, gradient based optimization algorithms are needed for efficiency reasons. One of the most efficient methods for solving image registration problem is the Gauss-Newton method [108] suitable for solving the problem of eq. (4.4) or the regularized cost function of eq. (4.17). The Gauss-Newton method is an iterative method performing the basic iteration of

$$\begin{aligned} J^T J h_{gn} &= -J^T r \\ w &= w + \alpha h_{gn} \end{aligned} \tag{4.20}$$

At each iteration it solves the linear system of equations to obtain a direction  $h_{gn}$  which is added to the current best solution of the parameters in  $w$ . The system of equations is derived using a first order Taylor approximation of the residual  $r(w+h) \approx r(w) + r'(w)h = r(w) + J(w)h_{gn}$ , which is put into eq. (4.4). By taking the derivative of the expression and equating it to zero, the Gauss-Newton system can be derived [112]. The Jacobian matrix  $J(w)$  contains the elements  $J(w)_{ij} = dr_i/dw_j$  giving it the size of  $n_{voxels} \times n_{params}$ . Instead of evaluating and inverting the prohibitive large  $J^T J$  matrix on the left hand side one may use a conjugated gradient [71] to solve the linear system. Since  $h_{gn}$  is a direction,  $\alpha$  has to be set to a value that decrease the image similarity function. This is a 1D sub-optimization problem solvable using a line-search method [113].

Levenberg [89] and Marquardt, [101] suggested a modification to the Gauss-Newton equation renaming it to the Levenberg-Marquardt algorithm. The modified system being

$$(J^T J + \mu I) h_{lm} = -J^T r. \tag{4.21}$$

The constant  $\mu$  is automatically tuned during the optimization such that if the Gauss-Newton system is a poor approximation of the function it is increased, thereby turning the direction  $h_{lm}$  into a steepest descent direction. If the Gauss-Newton system of equations serves as a good approximation, the Gauss-Newton direction is used. A properly chosen scheme for updating  $\mu$  mitigates the need for a line-search method.

The optimization methods described here are only a subset of the method which have been applied to solve image registration problems. Other popular choices

are the steepest descent, conjugate gradient and L-BFGS algorithms [112], [62], [94]. These algorithms only need access to evaluating the gradient and not the Jacobian which in the case of SSD is given by  $g = J^T \cdot r$ . As such any problem which is solvable by a Gauss-Newton or a Levenberg-Marquardt approach is also solvable using these algorithms, albeit probably solved less efficiently.

The image registration approaches used in the thesis, rely on gradient and Gauss-Newton optimization, only in combination with the SSD type of similarities measure. The implementation of gradient based optimization in relation to NMI or MI is more complicated, see for instance [124], [123].

### 4.2.6 Multilevel and smoothing

The multilevel method is a practical approach to improving robustness of image registration as to avoid local minima of the similarity based function but also to speed up the convergence rate of the algorithm. A multilevel approach solves the image registration problem at increasingly higher resolutions. Image registrations are initiated on a down-sampled and Gaussian smoothed representation of the moving image  $M$  and the fixed image  $F$  and upon solving the problem the deformation model is propagated on to a finer image resolution. The image registration is repeated for this and any consecutive resolution levels, until the finest resolution is reached.

The idea behind the approach is that at coarser resolutions, the similarity measure is less influenced by details and appears smoother to an optimizer. A smooth problem is easier to solve and should lead to a good starting point, from which the more detailed problem can be solved efficiently. A multilevel strategy can be the key to a successful and efficient image registration as demonstrated by many authors [145], [146], [63].

### 4.2.7 Example

To demonstrate some of the elements explained during the previous sections, an example registration was constructed. An intra subject registration was conducted with the purpose of bringing a T2 modality image into the space of an MPRAGE. It was performed using SPM8 using a rigid deformation and NMI similarity criteria as shown in figure 4.2. The figure shows the deformed T2 image in figure 4.2(c) which is more similar to figure 4.2(a) than the original image shown in figure 4.2(b). A clear change of codependency of the joint probabilities

distribution  $p(M,F)$  is observed. The distribution is depicted prior to registration in 4.2(d) and after registration in 4.2(e). This change in codependency, is supported by the NMI similarity, increasing from 1.02 to 1.12.

A two stage multi-level registration scheme sampled at 4 mm, 2 mm was applied to solve this particular image registration problem. In addition a FWHM of 5 mm was used to smooth the normalized histograms of the NMI similarity measure where the histogram was based on 256 bins.

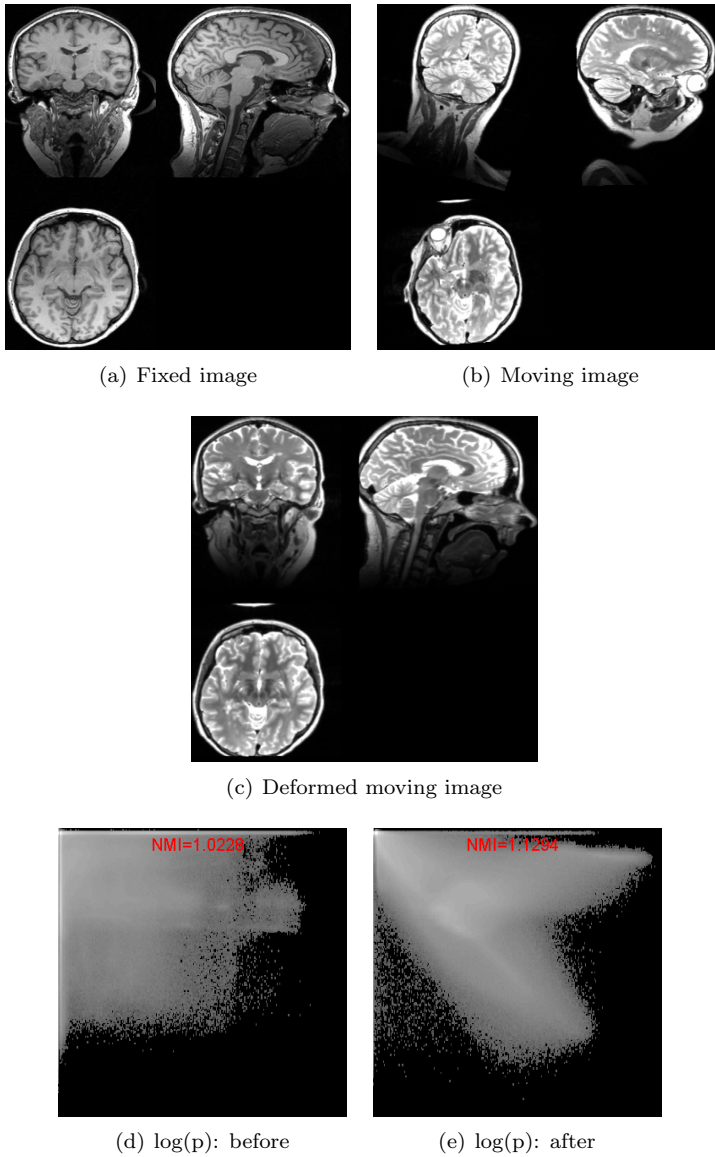


Figure 4.2: Example of multi-modal rigid image registration, visualized using the neurological convention. Shows the same coronal, sagittal and axial slice of the original images in (a)-(b) and the rigidly transformed image in (c). Further (d) and (e) shows the logarithm of the joint histograms ( $p$ ) from before and after registration.

## 4.3 Thirion's demons

Thirion's approach [147] to solving the problem of image registration, was originally thought to be somewhat ad hoc. It has later been shown to be theoretically well founded [157], minimizing a mean square error similarity function. It is a non-parametric approach, estimating the displacement field without the constraints of a deformation model. Thus any smoothness constraints on the deformation field has to come from regularization. Thirion's demons impose the regularization constraints, through smoothing of the gradient, making it particularly efficient compared to other non-parametric approaches. Compared to methodology previously introduced, Thirion's demons differs in terms of the similarity function, its deformation model and how it ensures regular deformation fields, further it employs an iterative update of the deformation field that does not use the traditional gradient based optimizers. The image interpolation step however remains the same as previously introduced.

In Thirion's original formulation each voxel is a demon which has an attraction force along a direction, derived from the image gradient. The classic implementation proposed by Thirion is found in algorithm (4.1). The iterative updates

---

**Algorithm 4.1** Thirion's demons

---

**repeat**

$$v(x) = \frac{(M(y(x)) - F(x)) \nabla F(x)}{\nabla F(x)^2 + (M(y(x)) - F(x))^2}$$

$$v(x) = G(0, \sigma) * v(x)$$

$$u(x) = u(x) + v(x)$$

$$y(x) = x + u(x)$$

**until** Convergence

---

of this algorithm proceeds for a fixed number of iterations, or until stopped by other ad hoc criteria. Step 2 of the algorithm, convolves the force field with a Gaussian kernel evaluated through the operator  $*$  and was mentioned in [157] to enforce an approximate fluid regularization on the image registration problem. The Gaussian kernel determines the smoothness of the field through the standard deviation  $\sigma$ . Step 3 and 4 of the algorithm performs an additive update of the deformation field.

A symmetric deformation field update was later proposed [159], [132] and shown to be more efficient while generating more regular deformations [86]. The method was also extended to emulate a diffusion type of regularization by introducing an additional convolution operator step into the algorithm. Introducing these improvements result in algorithm 4.2 minimizing the SSD similarity cost function of eq. (4.22), with  $\Omega$  denoting the image domain and  $v$  the transforma-

tion update at a given iteration.

---

**Algorithm 4.2** Thirion's symmetric demons
 

---

```

repeat
   $v_1(x) = \frac{(M(y(x)) - F(x)) \nabla F(x)}{\nabla F(x)^2 + \lambda \cdot (M(y(x)) - F(x))^2}$ 
   $v_2(x) = \frac{(M(y(x)) - F(x)) \nabla M(y(x))}{\nabla M(y(x))^2 + \lambda \cdot (M(y(x)) - F(x))^2}$ 
   $v(x) = v_1(x) + v_2(x)$ 
   $v(x) = G(0, \sigma_{fluid}) * v(x)$ 
   $s(x) = G(0, \sigma_{diff}) * (u(x) + v(x))$ 
   $y(x) = x + v(x)$ 
until Convergence
  
```

---

$$\sum_{i \in \Omega} (F(x_i) - M(y(i)))^2 + \frac{\sigma_i^2}{\sigma_x^2} \cdot \sum_{i \in \Omega} (\nabla v_i)^2 \quad (4.22)$$

Algorithm 4.2 can be reformulated to be solved by gradient based optimization methods as in [86], in which case the velocity field  $v(x)$  becomes a voxel-wise gradient descent direction which decreases the function in eq. (4.22). Using this descent direction the limited memory-Broyden, Fletcher, Goldfarb and Shanno (L-BFGS) [94] algorithm is used to minimize the problem. In line with Thirion's original suggestion  $\sigma_i = \|F(x_i) - M(y(x_i))\|^2$ . The parameter choices of  $\sigma_{fluid}$  and  $\sigma_{diff}$ ,  $\sigma_x$  should be tweaked for a given problem and  $\lambda = 1/(\sigma_x^2)$  can be understood as the weighting parameter of regularisation. It can also be viewed as a term penalising the noise level of the spatial deformation.

The efficiency of this method is one of the reasons for its large success which it achieves due to the Gaussian convolution way of implementing regularization which can be done extremely efficient in the Fourier domain. In contrast, traditional image registrations requires the evaluation of derivatives of regularisation, which is computationally expensive. Although we did not take steps to produce diffeomorphic fields it is possible to achieve [157].

## Un-warping geometric distortions of echo planar imaging

The reason for introducing Thirion's demons in this thesis, is to solve the problem of un-warping the geometric distortions of images from echo planar imaging (EPI) sequences as presented in the abstract of chapter 8.

Diffusion weighted images (DWIs), acquired using EPI sequences, are subject to many imaging artefacts, one of which is caused by static magnetic field inhomogeneity due to tissue susceptibility which causes a geometric displacement of the

voxel intensities, along the phase encoding direction of the images. Correction of this artefact is important to obtain anatomical correct images that can be aligned with structural MRIs, see also section 3.3.

By acquiring two DWIs without diffusion weighting ( $b_0$ ), each with a reversed read-out gradient polarity, the same image distortion can be induced in both  $b_0$  images but with opposite distortion directions [73], [31]. This is illustrated in Figure 4.3(a)-(b) showing two oppositely distorted  $b_0$  images and further highlighted in Figure 4.3(c) where one  $b_0$  image shown in red has been overlaid on top of the other  $b_0$  shown in green. The displacement field relating the displacement between two reversely distorted  $b_0$  images, is estimated using image registration similar to [73].

Thirion's demons is used to estimate the deformation field  $u(x) : \mathbb{R}^3 \rightarrow \mathbb{R}^1$  for the matching problem  $F(x) \approx M(y(x)) \cdot (1 + J(u))$ . Modulation of the intensities with the Jacobian is required since geometric distortions also lead to an intensity pileup in distorted regions which needs to be compensated. The displacement field for geometrically un-warping all DWIs, is given by half the estimated displacement field,  $u/2$ .

*The registration pipeline:*

A 3 stage image registration pipeline is proposed to increase the robustness of estimating the deformation field. For each stage the deformation field of the previous stage is used as a start guess for the next. The procedure is:

- 1) Estimate the field between two background thresholded  $b_0$  images being matched.
- 2) Estimate the field between two double thresholded and smoothed  $b_0$  images using a threshold for the background and a second for removing the cerebrospinal fluid (CSF).
- 3) Estimate the field based on the true intensity of the two  $b_0$  images, introducing intensity modulation into the image registration problem only at this stage.

The thresholding yields binary estimates of brain tissue which are easy to register and only slightly affected by intensity modulation of the  $b_0$  intensity distortions. The image registration during stage 1-2 brings the deformation field in the proximity of the desired solution while avoiding potential minima which could occur due to the added complexity of Jacobian modulation. At stage 3, the image registration occurs between the two  $b_0$ s and intensity modulation becomes essential.

## A demonstrator case

An example from utilizing the approach is shown in Figure 4.3. (d) Shows the moving image (red) completely deformed into the domain of the fixed image (green) and (e)-(g) shows the correctly undistorted image, the deformation field estimated using Thirion's and a displacement map from the highly popular fieldmap [79] approach aiming to solve the same problem. It is noted how the displacement maps obtained from the fieldmap approach and Thirion's demons have certain similarities but also dissimilarities. From inspection alone it is hard to say which is the smoother field but Thirion's demons result are obviously impacted by the smoothness prior present in image registration problems. Tweaking of the smoothness penalty could potentially make the two more similar but may not be desirable if the field map results are inferior as indicated by the results in chapter 8.

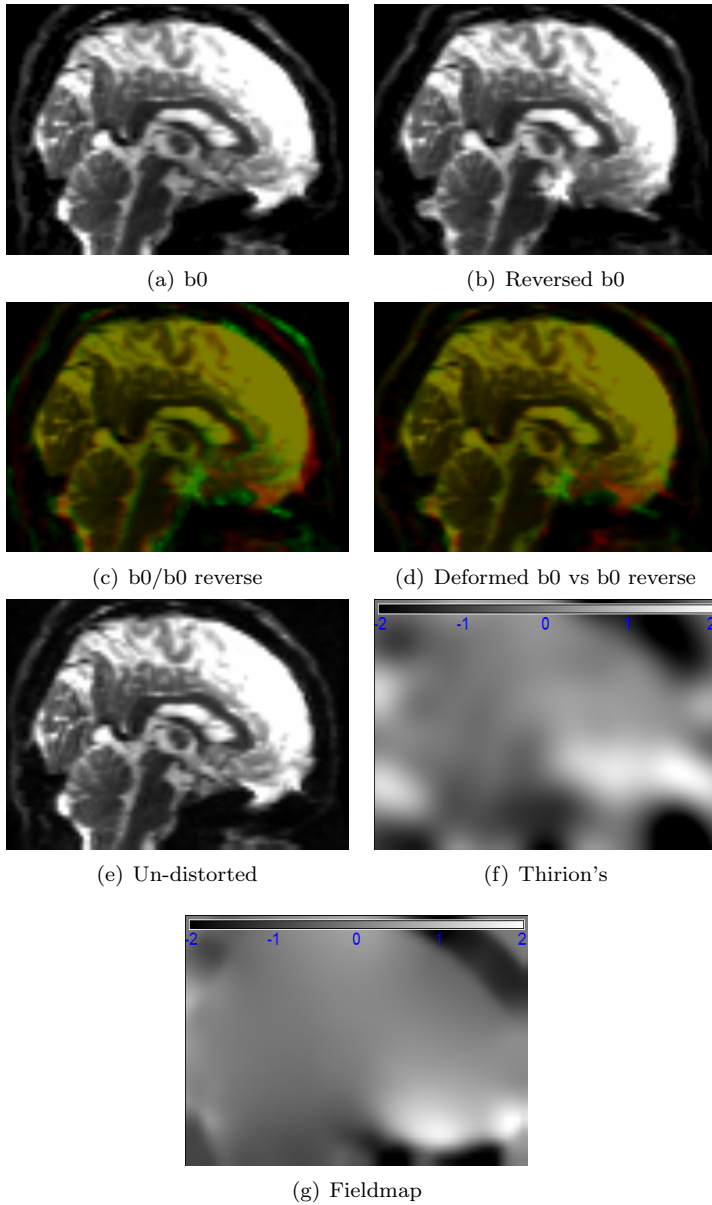


Figure 4.3: Example of using Thirion's demons to estimate a voxel displacement map and correcting for geometric image distortions. Two b0 images with reverse phase encodings are shown in (a)-(b) and overlaid on-top of each other as the red/green overlay in (c). The brain of the b0 image in green is more compressed than the red. In (d) the red b0 is fully transformed towards the green. (e) Shows the b0 artefact corrected image using half the voxel displacement of the image registration. (f) Shows the voxel displacement map of our approach which is compared to the map of the field map approach in (g)

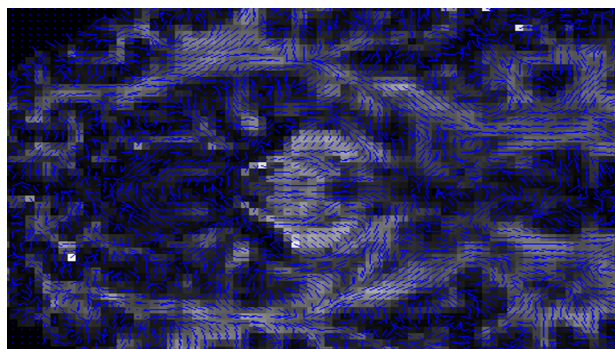
## 4.4 Tensor reorientation strategies

Until now we have mainly been concerned with deforming 3D scalar images. If the end goal is to perform cross subject analysis between diffusion tensors (DT), special techniques are needed. Applying an image deformation to each individual 3D volume of a 4D DT volume causes problem because the underlying direction of the DTs will not be changed unless something is done to explicitly change the orientation. To illustrate this problem we have simulated a rotation of a 4D DT volume with and without proper tensor reorientation. Figure 4.4(a) shows the principal directions overlaid on the background of a fractional anisotropy (FA) image while Figure 4.4(b) shows the directions after rotation of the DT volume (no reorientation). Clearly the principal directions of the DTs shown as blue arrows are no longer aligned with the anatomy. Solutions to this problem were suggested by Alexander et al. [5] and the result of using one of these solutions is shown in Figure 4.4(c) where proper reorientation have been applied to the DTs.

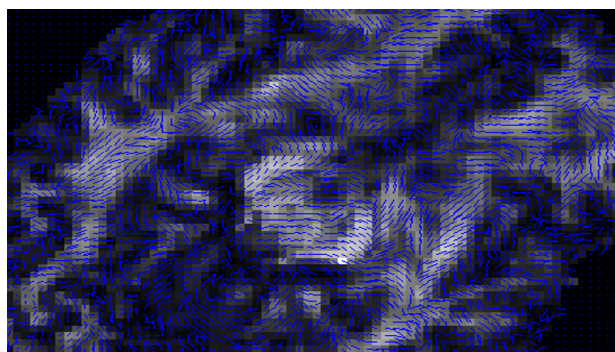
Lets now consider two strategies for properly reorienting tensors. The finite strain (FS) and the preservation of principal direction (PPD) approach. First we note that if an image deformation is given purely by a rotation matrix  $R$ , the DT can be reoriented by  $D' = R^T D R$ . This will be the basis for the two strategies which differ in how they approximate  $R$  from what we initially assume to be affine deformations.

If the image deformation is made up by an  $3 \times 3$  affine matrix  $A$  (dis-regarding translations), the above reorientation strategy still applies however it requires knowing the rotational part of  $A$ . The (FS) approach [99] offers the solution, by decomposing the matrix  $A$  into an orthogonal rotation matrix  $R$  and an affine component  $F$  such that  $A = F R$  where  $R = (A A^T)^{-1/2} A^T$ .

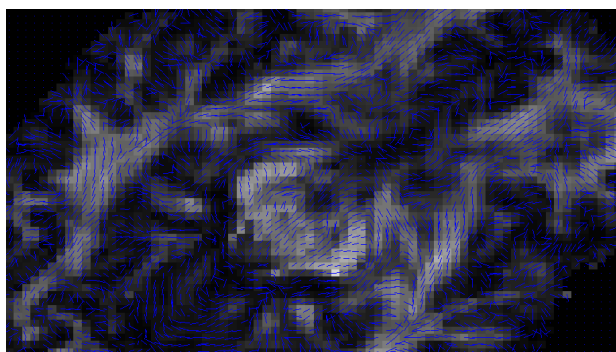
The PPD [5] algorithm was later suggested as a better approach for estimating the rotation  $R$ . It works by defining  $n_i = A e_i / |A e_i|$ , which is the re-normalized  $i$ th eigenvector after applying the transformation  $A$ . The desired rotation  $R$ , which is required to map the original  $e_1$  to  $n_1$  is estimated via PPD. The PPD computes a separate  $R$  at each voxel and uses it to reorient only the DT in that voxel. The  $R$ s returned by PPD are unique rotation matrix mapping  $e_1$  to  $n_1$  and  $e_2$  to a unit vector perpendicular to  $n_1$  in the plane spanned by  $n_1$  and  $n_2$ . It is calculated by the first estimating the angle between  $n_1$  and  $e_1$ , and applying this rotation to  $e_2$  such that the rotation between  $n_2$  and  $R_1 e_2$  allows to estimate a secondary rotation  $R_2$  resulting in the desired solution  $R = R_1 R_2$  which is then applied to  $D$  as previously mentioned. The PPD angular estimation follows the recipe of the original article [5].



(a) DT volume



(b) Rotated DT volume



(c) PPD corrected DT volume

Figure 4.4: Highlights the importance of reorienting DTs undergoing image transformations. (a) Shows the principal directions of the DTs. (b) Shows the principal direction of DTs undergoing an axial image rotation of 45 degrees with no reorientation applied, resulting in erroneous orientation of the principal directions with respect to the WM fibers. (c) Shows the effect of applying the reorientation strategy of PPD to solve the problems in (b)

1. Compute a rotation matrix  $R_1$ , that maps  $e_1$  onto  $n_1$ . The axis and angle of this rotation are obtained from the vector and scalar products of  $e_1$  and  $n_1$ .
2. Estimate the projection vector  $P(n_2) = n_2 - (n_2 \cdot n_1) \cdot n_1$ .
3. Compute a rotation matrix  $R_2$ , that maps  $R_1 e_2$  onto  $P(n_2)$  where the axis of rotation is  $R_1 e_1$  and the angle is obtained from the dot product of  $R_1 e_2$  with the unit normalized  $P(n_2)/|P(n_2)|$ .

Both the FS and PPD can be generalised for higher order image deformations by considering the Jacobian matrix of a deformation field. Assume a higher order deformation is described by a displacement field  $u(x)$ , than an affine matrix  $A$  can be described by a local linear model derived from the Jacobian  $J$  of  $u$ :  $A(x) = I + J(u(x))$ , where  $I$  is a  $3 \times 3$  identity matrix. This affine matrix  $A$  allows the rotation  $R$  to be computed using either the FS or PPD approach.

These strategies are applicable using deformation fields derived based from registering 3D scalar images but can also be used to formulate an image registration problem using all of the tensor components. This is the topic of the next section.

## 4.5 Tensor based image registration

High dimensional image registration is relevant when multi channel image data is available and all are believed to contribute with information relevant to improving correspondences between the moving image and the reference image. The diffusion tensor (DT) fits this description and has been the subject of several papers suggesting DT based image registration approaches [135], [117], [44] and [180]. Another interesting approach with particular emphasize on large scale deformations is presented by Cao et al. [27]. This approach deviates from the other DT registration approaches by matching based on the principal eigenvector direction only, instead of using the full DT.

We have used the approach implemented in the diffusion tensor imaging tool kit (DTI-TK) (<http://dti-tk.sourceforge.net/>), as described by Zhang, in [180], [181]. These papers suggested the use of a piecewise affine (PWA) deformation model, to construct a similarity measure aimed at optimizing not only the similarity between tensor components but also the orientation of the tensors. Approaches prior to this did not explicitly optimize with respect to tensor orientation but retrospectively took care of the tensor reorientation via the previously described PPD algorithm.

The components of Zhang’s approach are the same as those needed for scalar image registration problems, thus requiring an interpolation method, a deformation model, a similarity measure and an optimization method. An overview of these components as used in high dimensional registration, is given next.

### Interpolation: The Log-Euclidean framework

As with any image registration problem, an interpolation method is needed for re-sampling images. Using a standard approach may lead to inappropriate results since an Euclidean average of DTs might change the shapes of the DTs in an undesirable way, potentially producing non SPD DTs. This problem was observed in [150], [7] where an average of two DTs led to the determinant of the Euclidean mean of the DTs to become larger than the average determinants of the original DTs. Thereby demonstrating that tensor averaging introduces increased dispersion of the tensors, which is physically unrealistic.

The purpose of the log-Euclidean framework independently proposed by [7] is to minimize unrealistic effects, while maintaining SPD properties of the tensors. Using the log-Euclidean metric space, a mean is calculated by

$$E(D) = e^{\sum_{i=1}^n w_i \ln(D_i)}. \quad (4.23)$$

In order to use this mean for image re-sampling, each  $w_i$  must be the weightings relating to each of the nearest neighbour tensors  $D_i$ . The weights are determined by the distance to the positions of the tensors similar to the case of ordinary image re-sampling as seen in the introduction.

The formula in eq. (4.23) suggest to take the matrix logarithm, perform the Euclidean operation (the average) and finally exponentiate the results. This approach is general for the log-Euclidean framework and allows other Euclidean based operations to be evaluated as well, see [7] and [120]. In terms of the metric space, the null eigenvalue space can only occur at infinite metric distance and thus becomes impossible to achieve in practice. This ensures the preservation of SPD DTs.

The log-Euclidean technique is a specific instantiation, of the more general Riemannian metrics presented by [61], however this technique suffers from an increased computational burden and thus the log-Euclidean framework is preferred.

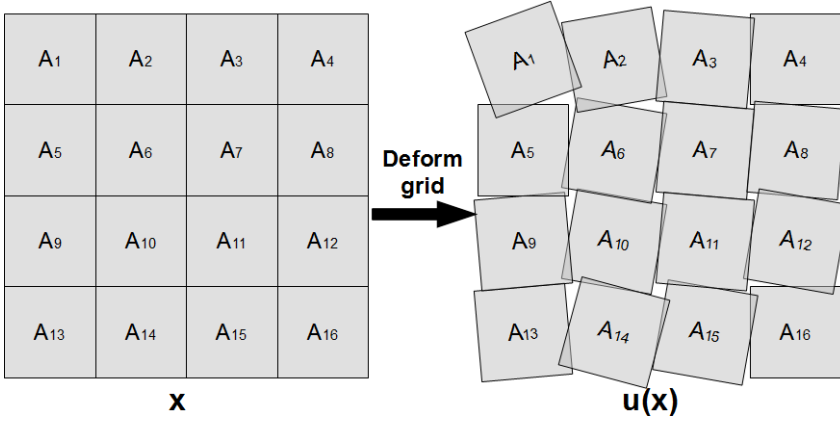


Figure 4.5: Shows the local division of space used by the PWA deformation model. On the left is shown a  $4 \times 4$  division of the spatial image domain, each part of the  $i$ th domain is equipped with an affine model  $A_i$ . On the right is an illustration of how the PWA model deforms the grid.

### Deformation: The piecewise affine model

The piecewise affine (PWA) model is a locally flexible deformation model which consists of several affine models dividing the image domain. Each individual model is responsible for optimally deforming the  $i$ th part of the moving image towards a corresponding part of the fixed image. This localized model is illustrated in Figure 4.5 showing how the model would be defined across a 2D image, using a  $4 \times 4$  PWA model. The models are indexed by  $A_1 \dots A_{16}$  with the index  $i$  running from left to right, therefore the top-left model of the Figure 4.5 is  $A_1$  and the bottom right is denoted  $A_{16}$ . When a smooth deformation displacement field is desired across the entire domain, the interpolation scheme of [93] is used.

### Similarity: Tensor based

The SSD similarity, enabling explicit optimization of the orientation between the moving tensor image (M) and the fixed tensor image (F), can be written

$$D(M, F) = \sum_i \int_{\Omega_i} \|M(RSx+t) - RF(x)R^T\|^2 dx + \lambda \sum_{i,j} \int_{\Omega_i \cap \Omega_j} \|A_i x - A_j x\|^2 dx. \quad (4.24)$$

This equation consist of a two part sum, the first part is the tensor similarity which sums the SSD norm across  $i$  rectangular regions of the image. The second part is a regularization term weighted by  $\lambda$ . It enforces smoothness along the boundaries of the  $(i, j)$  neighbouring regions of the PWA model. We note how the similarity part of the function uses the reorientation ideas presented in section 4.4, to explicitly orientate the tensor of the fixed image into the deformed moving image. This is of course possible due to the choice of the PWA deformation model where each affine model can be written as a combination of rotation  $R$ , scale and shearing contained in  $S$  and the translational components in  $T$ .

## Optimization

To solve the problem of eq. (4.24), a conjugate gradient optimizer [62] is used since, the form of the function is differentiable with respect to rotation, scaling, shearing and translation. The analytical gradients of the function with respect to the parameters can be found in the paper by Zhang, [181].

The PWA model is fitted in a coarse to fine manner starting with a few affine models, covering large regions of the domain. Once convergence is achieved using the coarse PWA model, the domain is subdivided and the coarse affine model parameters are propagated into the subdivided domain where the cost function is again solved. Upon convergence at the finest level, the PWA model is discretized into a displacement field  $u(x)$  used to deform the moving image into the space of the fixed image. At this stage the PPD algorithm presented in the previous section, is applied to reorient the tensors.

An example of applying the registration algorithm is shown in Figure 4.6. It shows the tensors of a slice in the fixed image domain  $F$  in (a), the same slice of the original moving image  $M$  is shown in (b) and the result of deforming the tensors of  $M$  into the space of  $F$  is shown in (c). Visual inspection of (a)-(d) suggests that the deformed moving tensor is considerably better aligned than the original tensor.

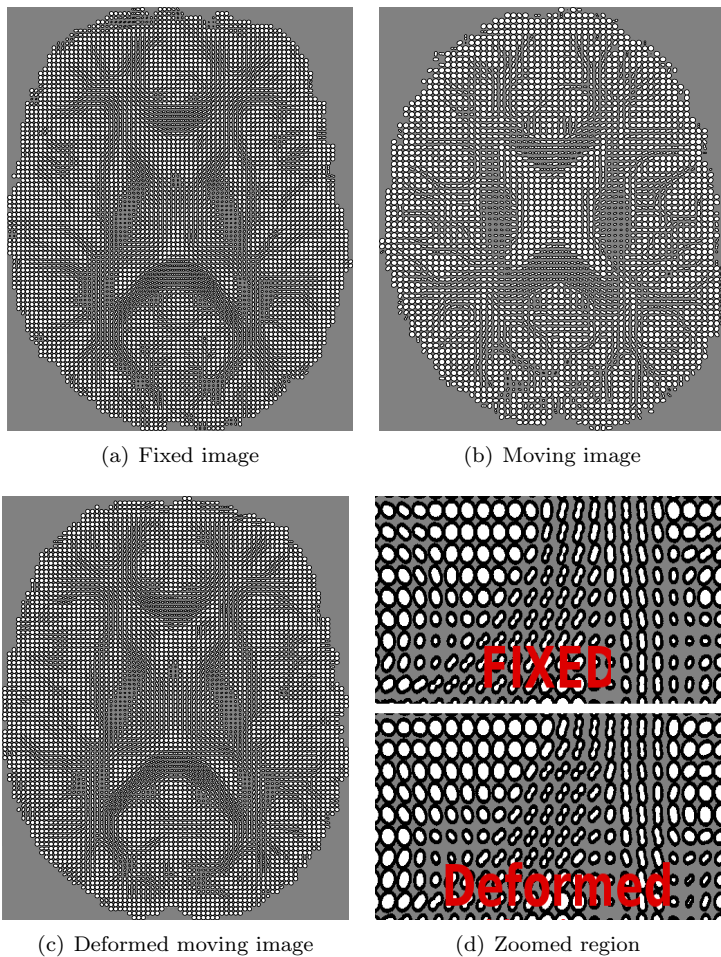


Figure 4.6: Illustrates high dimensional tensor image registration using neurological convention, where (a) shows the tensors ellipsoid profiles of a slice in the fixed image domain, (b) shows the corresponding slice of the moving tensor image and (c) the deformed the tensors of the moving image. The fixed image in (a) has a higher voxel resolution ( $1.75 \times 1.75 \times 1.75 \text{ mm}^3$ ) than the moving image ( $2.3 \times 2.3 \times 2.3 \text{ mm}^3$ ) in (b). After deforming the tensor image, it is output at  $1.75 \times 1.75 \times 1.75 \text{ mm}^3$  in (c). (d) shows a regional zoom of the fixed and deformed images taken near the splenium. This enables a detailed view of the registration performance

## 4.6 Building an atlas

The inter variability of anatomy shape across brains makes the interpretation of medical images challenging. The construction of an atlas addresses this problem by defining a common reference space to compare anatomy between subjects, between groups of subjects and corresponding sites. To combat this challenge, the Talairach atlas [144] was one of the first atlas spaces proposed for the brain. The Talairach brain is one brain dissected and photographed and an anatomical meaningful coordinate system built from it. Researchers desiring to use this atlas have to somehow bring their images into this coordinate space, a task suited for image registration whether intensity based or correspondence based. The Montreal neurological institute (MNI) atlas [54] was later developed as an atlas based on a large population of healthy subjects thus constructing a space more suitable to represent a previously unseen brain. Today the MNI atlas is one of the most used in neuro imaging and different variations of MNI based atlases exist.

If an MNI atlas is deemed inappropriate for a specific study or not available one could build a population specific atlas from the available subjects. We use the ideas proposed by [22], [77] to build an intensity based atlas  $M_0$  which is unbiased with respect to the anatomical shape variations across subjects. The procedure for building the atlas is described in algorithm 4.3.

---

**Algorithm 4.3** Population specific atlas construction

---

**Require:** Rigidly register subset images to a fixed image.

**Require:** Estimate mean  $M_0$

**repeat**

    Rigidly register all images to  $M_0$

    Update  $M_0$

**until** Convergence

**repeat**

    Affinely register all images to  $M_0$

    Update  $M_0$

**until** Convergence

**repeat**

    Non-rigidly register all images to  $M_0$

    Update  $M_0$

**until** Convergence

---

The approach usually runs for a fixed number of iterations to before declaring convergence. At each repeated registration the results of the most recent registration is used as start guess for the current registration. During the fi-

nal stage of the process, deformation fields and deformed images are usually output. Figure 4.7 shows the construction of a human atlas using 25 healthy subjects. The atlas was constructed using high dimensional tensor registration and is used in the paper described in chapter 9, to supply a common reference space for studying the diffusion indices of an MS population. The figure depicts the atlas after completing each of the steps 3-5. Throughout this process, the atlas becomes less blurred enabling improved registration accuracy at the next step. Alternative approaches to estimating population specific unbiased atlases using image registration are found in, [19], [133] and [142].

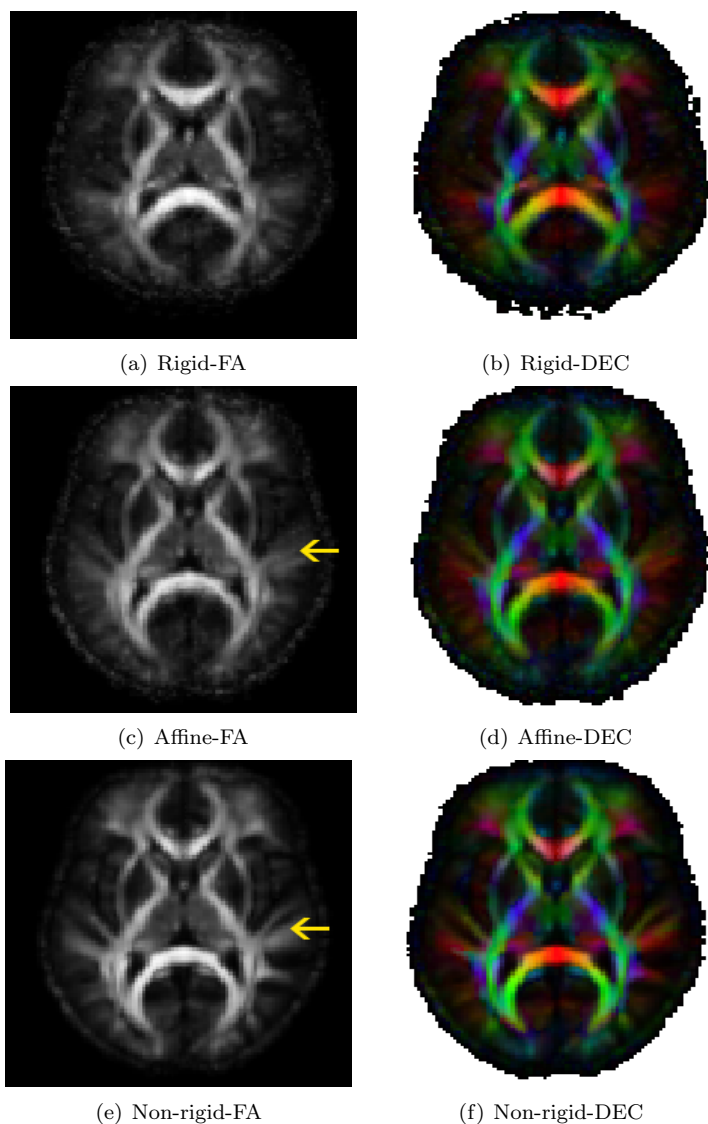


Figure 4.7: Shows an axial slice of a tensor atlas as it converges to the mean atlas and becomes crispier as the deformations become more flexible, shown in neurological convention. (a)-(b) Shows the FA and the RGB directionally encoded colormap (DEC) of a slice of the tensor atlas after rigid registration where RGB(R=left/right, G=anterior/posterior, B=inferior/superior). (c)-(d) shows the FA and DEC slice after affine registration and (e)-(f) shows the FA and DEC after the PWA registration. Regions of improvements are indicated by the yellow arrow.



## CHAPTER 5

# Cross Subject Statistical Analysis

---

### 5.1 Introduction

This chapter introduces statistical analysis methods used to identify and/or quantify the information content of hypothesized multiple sclerosis (MS) image markers. To draw meaningful inference based on statistical methods requires pre-processed images. Strategies for pre-processing diffusion MRI were described during chapter 3 and chapter 4. Throughout this chapter it is assumed that such strategies have been applied to the images, enabling cross subject correspondence and the statistical methods detailed in this chapter are only applicable under this assumption.

In section 5.2, the classical linear regression model is revised as a tool for analysing the information content of image markers.

The model is also used in section 5.3, which describes localized sample based analysis also known as voxel-based analysis (VBA). VBA allows for the identification of localized regions of the brain that might indicate disease pathology and has been used to study diseases such as Alzheimer's disease [24], amyotrophic lateral sclerosis (ALS) [179], MS [116], [28], [174], pediatric chromosome 22q11.2 deletion syndrome [177] and multiple others.

Finally, section 5.4 presents a method proposed in the manuscript of chapter 9 which is used to examine whole-structure hypothesis based on scalar diffusion indices (FA, TN) derived from diffusion MRI. For instance, to answer if the multivariate diffusion indices of an entire WM tract are significantly different between two groups of subjects.

## 5.2 The general linear model - Disease score modelling

We define the disease score model as a model that is based on one or more covariates (imaging markers) is able to predict the disease score, to some degree of certainty. A popular model form is the general linear model (GLM)

$$Y_i = \beta_0 + \beta_1 X_{i1} + \dots + \beta_n X_{ik} + \epsilon_i, \quad i = 1 \dots n, \quad (5.1)$$

where  $n$  is the number of independent values equal to the number of study subjects and  $k$  denotes the number of covariates assumed to generate the individual disease score observations in  $Y_i$ . Covariates could be imaging markers or confounds such as gender and age. Collecting all observations in  $Y$  and the covariates in the design matrix  $X$ , eq. (5.1) can be re-written in matrix form

$$Y = X\beta + \epsilon. \quad (5.2)$$

It is assumed that the underlying process generating  $Y$  is the result of a stochastic process generating independent and identically distributed variables from a normal distribution  $Y_i \sim N(\mu, \sigma^2)$ . In this case the optimal least squares solution is given by

$$\hat{\beta} = (X^T X)^{-1} X^T Y. \quad (5.3)$$

To quantify and compare the performance of several models based on competing imaging markers we can use the coefficient of determination  $R^2$  as a performance metric. It attains the value 0 for a poorly performing model and 1 for a model which predicts  $Y$  without error. Roughly speaking, a higher  $R^2$  value indicates a more informative marker. A general definition of  $R^2$  is

$$R^2 = 1 - \frac{SSQ_{err}}{SSQ_{tot}}, \quad SSQ_{err} = \|\hat{Y} - Y\|^2, \quad SSQ_{tot} = \|\bar{Y} - Y\|^2 \quad (5.4)$$

and corresponds to the fraction of the variance explained by the fitted model  $\hat{Y}$  relative to the usual variance.

Further information about linear regression analysis and model comparison measures such as  $R^2$  can be found in books detailing GLMs [46], [48], [162].

## 5.3 Localized sample based analysis

The purpose of a localized statistical analysis is to examine if localized changes of the brain are related to the overall state of a disease such as MS. The analysis is done by fitting a GLM to the cross subject values of each voxel and deciding whether the parameters of interest are significantly different from the null hypothesis. If so, it is rejected in favour of the alternative hypothesis, indicating a disease relevant voxel.

To examine where the image values of two groups are different, we formulate a separate GLM for each voxel.  $Y$  contains cross subject values of a specific voxel and  $X$  is the design matrix corresponding to the grouping variables and cross subject confounding covariates. After fitting the GLMs to all voxels of the image domain, Student's t-test [162] may be used to test the hypothesis of group differences,

$$t = \frac{\bar{x} - \bar{y}}{S_{xy} \cdot \sqrt{(1/n_x) + (1/n_y)}}. \quad (5.5)$$

In this two sample t-test  $\bar{x}$ ,  $\bar{y}$  correspond to the GLM group parameter estimates, possibly adjusted for confounding covariates.  $S_{xy}$  is the pooled variance between the two groups, of sample sizes  $n_x$  and  $n_y$ . If we assume unequal variance of the two populations, the denominator of the test changes and the test becomes known as Welch's t-test [167].

Once calculated, the volume of t-tests can be visually inspected. However, for ease of interpretation the t-test are usually thresholded to retain only voxels that are most likely to correspond with the rejection of a null hypothesis. This is done by choosing a probability value  $\alpha$  from the theoretic t-test distribution and finding the corresponding t-test threshold. If we desire less than  $\alpha = 0.05$  probability of erroneously rejecting that the group means are the same, the threshold  $t$  must full-fill  $P(T = t) = 1 - 0.05$ . This rejection threshold should not be confused with the p-value which is defined as the probability threshold where a hypothesis goes from being accepted to being rejected.

### Multiple comparisons

The selection of the null hypothesis rejection criteria  $\alpha$  becomes difficult when doing multiple voxel-based tests, since each individual voxel test is performed with  $\alpha$  probability of falsely rejecting the null hypothesis. This means that the chance that at least one hypothesis is falsely rejected becomes much higher than  $\alpha$ . Bonferroni [49] suggested to solve this problem by dividing  $\alpha$  with the

number of hypothesis test conducted. Bonferroni's strategy leads to a very conservative choice of  $\alpha$  often unable to detect any volumetric differences, therefore less conservative approaches are needed to select an appropriate  $\alpha$ . One problem with the Bonferroni approach which makes it overly conservative, is that it does not take into account that neighbouring voxels are highly correlated. Accurately accounting for such effects may significantly change the value of  $\alpha$ . The correlation of voxels may originate from several sources but a dominant source is the smoothing of data often used to increase the signal to noise ratio [97] prior to statistical analysis.

To account for the problem of multiple comparisons [95], [106], the small volume correction (SVC) approach suggested by Worsley et al. [173] can be used to estimate Family Wise Error (FWE) corrected p-values with respect to small regions of interest (ROIs). The SVC accounts for spatial correlation of the images and is less conservative than whole-brain corrections such as the Bonferroni but requires prior knowledge of ROIs. The ROIs should be specified independently from the study being conducted and requires a priori ROI specific hypothesis to be formulated before doing the SVC analysis.

The above ways of dealing with the multiple comparison problems rely on random field theory [97], developed in the context of functional MRI and the topic is further treated in [49], [173] and [66]. We have used the SVC analysis strategy to do the voxel-based ACM analysis described in the manuscript of chapter 10 where we formulated the hypothesized areas of interest to be the motor-related tracts.

## Multivariate hypothesis tests

If the type of analysis is multivariate, the ordinary t-test is altered to Hotelling's t-squared statistic [75],

$$T^2 = \frac{(n_x n_y)}{(n_x + n_y)} (\bar{x} - \bar{y}) S^{-1} (\bar{x} - \bar{y}). \quad (5.6)$$

The mean model parameters of the two groups are collected in vectors  $\bar{x}$ ,  $\bar{y}$  and the pooled covariance matrix is estimated in  $S$ .

## 5.4 Tract-oriented analysis

This statistical method investigates whole-tract hypothesis. It enables to answer whether the multivariate diffusion indices defined on a sheet-like model of a WM tract (described in section 3.7), results in significant difference between two groups of subjects.

The first part of this section describes how a tract-oriented statistical model is formulated and estimated. The model serves as a compact functional description of diffusion indices sampled on the WM tract. The compact description of otherwise high dimensional data, makes statistical inference tractable as it takes care of the inherent high-dimension, low-sample-size problem. The second part of tract-oriented analysis draws statistical inference about subjects based on the compact model description using permutation tests, resulting in a significance value suggesting whether groups are different.

The tract-oriented analysis approach described in detail during this section has been used to compare MS and healthy control subjects as described in the paper of chapter 9.

### Part 1: The tract-oriented statistical model

The statistical model enables a compact functional description of the diffusion indices which are parameterized as a function of medial sheet position, using the cm-rep model.

To estimate the model, diffusion indices must first be sampled. Diffusion indices are sampled along the spokes of the cm-rep model introduced in section 3.7. An example of the cm-rep model is depicted in the middle box of Figure 3.10 which shows sampling spokes in red. The spoke lines are used to sample indices on both sides of a medial sheet  $m$  shown in green and the average of these samples are projected onto the medial sheet  $m$ . For the  $i^{th}$  subject, we can express these samples as a function of the sheet position  $t$ ,  $f_i(t) : t \in m$ .

Having completed the sampling for  $n$  subjects resulting in  $f_1 \dots f_n$  anatomically corresponding functions of the diffusion indices, the statistical model is estimated. The model estimation is outlined through eq. (5.7)-(5.9). First the sample correlation function is estimated by

$$c(s, t) = \frac{\sum_{i=1}^n (f_i(s) - \bar{f}(s))(f_i(t) - \bar{f}(t))}{\sqrt{\sum_{i=1}^n (f_i(s) - \bar{f}(s))^2 \sum_{i=1}^n (f_i(t) - \bar{f}(t))^2}}, \quad (5.7)$$

where  $s$  and  $t$  refers to positions on the medial sheet and  $\bar{f}(t)$  is the cross subject mean. The linear model basis  $\xi$  of the statistical model can now be estimated using the eigen decomposition satisfying eq. (5.8)

$$\int c(s, t) \xi(t) dt = \lambda \xi(s). \quad (5.8)$$

With the eigenvectors in  $\xi$  and the eigenvalues in  $\lambda$ , the model parameters of the  $i^{th}$  subject are estimated by

$$b = \int \xi(t) (f_i(t) - \bar{f}(t)) dt. \quad (5.9)$$

The procedure of eq. (5.9)-(5.7) is commonly known as a principal component analysis (PCA) where  $b$  is known as the principal component parameters (the parameters of our statistical model). Exact reconstruction of the observations in  $f_i(t)$  is possible from the parameters of  $b$  using the model expression

$$f(t) = \bar{f}(t) + \sum_{j=1}^n \xi_j(t) \cdot b_j. \quad (5.10)$$

Since  $f_i(t)$  is affected by noise, an exact reconstruction is usually not desirable. Instead it is assumed that the last  $j$  parameters of  $b$ , describing the least amount of signal can be removed. We use the strategy of only retaining model components that have eigenvalues larger than the mean eigenvalue. This is equivalent to Kaiser's rule [80] which is just one way of selecting a suitable number of model parameters.

Another popular choice is the 95 percentile rule where one retains the number of parameters needed to model 95 percent of the data in  $f$ . Normalized eigenvalue plots may also be used to determine an appropriate number of parameters. Figure 5.1 shows such plots for a statistical model based on 25 healthy controls and 35 MS patients of the study presented in the manuscript of chapter 9 which was based on FA and TN diffusion indices. The figure shows the eigenvalue plots of 11 tract-oriented statistical models, based on the sheet-like models of the corpus callosum (CC), the inferior longitudinal fasciculus (ILF), the uncinate fasciculus (UNC), the superior longitudinal fasciculus (SLF), the corticospinal tract (CST) and the inferior fronto-occipital fasciculus (IFO). Both Kaiser's rule and the 95 percent rule are indicated on the plots. It is seen that Kaiser's rule tends to remove more parameters than the 95 percentile rule. Based on Kaiser's rule and depending on the WM tract, we retain between 12-18 model parameters, to form the basis of the statistical decisions made using permutation tests.

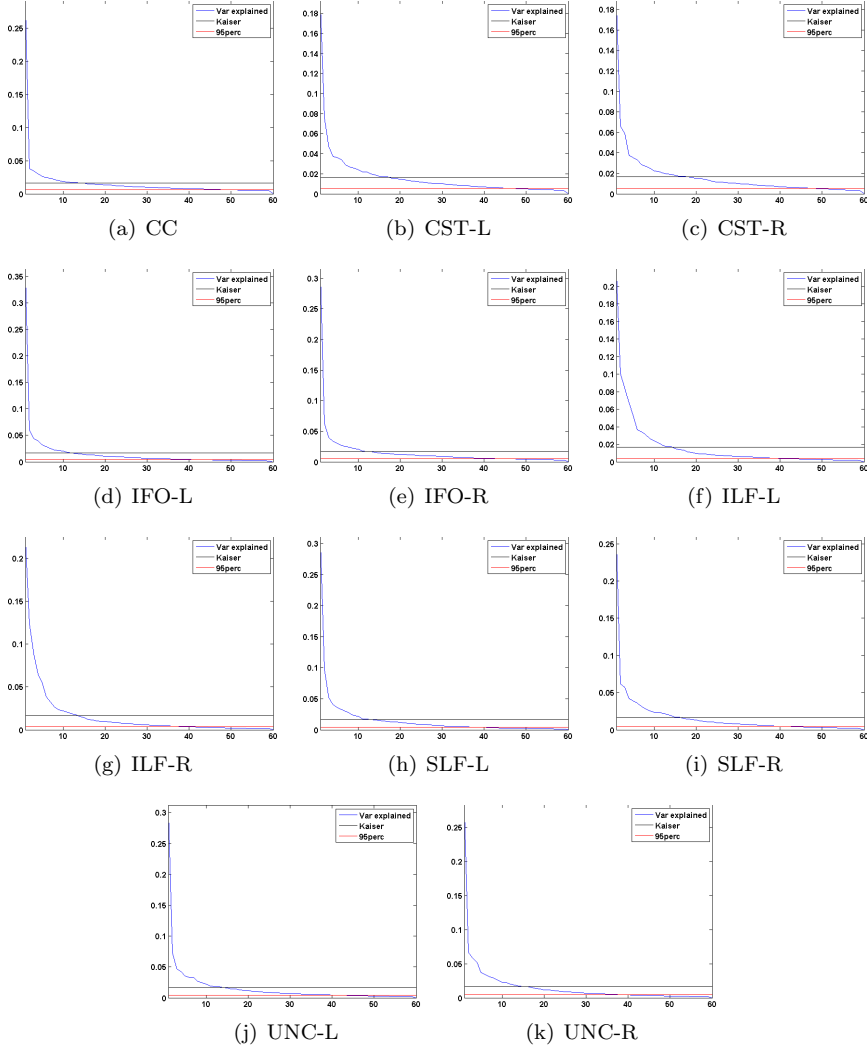


Figure 5.1: Normalized eigenvalue plots (scree plots) are shown for the statistical models of 11 separate WM tracts. The plots show the percentage-wise amount of variation modelled by each parameter of a model. Also shown are two model reduction criteria of Kaiser's rule and the 95 percent rule. Kaiser's rule generally favours smaller models.

## Part 2: Permutation tests using Hotelling's test size

Permutation tests [168] refers to a class of non-parametric tests that use random shuffling of the data to estimate the distribution of a test statistic under the null hypothesis. Permutation tests provide exact significance values since they make no assumptions about the true statistical test distributions however permutation tests are usually also computationally more expensive than standard statistical tests. Permutation tests are useful when we have insufficient information about the distribution of the data or are uncomfortable making assumptions about the distribution.

We use permutation test to obtain p-values for the tract-oriented statistical hypothesis, testing whether the tract specific parameters of eq. (5.9) are significantly different between two groups of subjects. Suppose that  $X_1, \dots, X_m \sim F_X$  and  $Y_1, \dots, Y_n \sim F_Y$  are samples from two independent distributions where each  $X_i$  is a vector of linear model parameters from the  $i^{th}$  subject. To test whether the mean of  $F_X$  is significantly different from that of  $F_Y$ , algorithm 5.1 is used. The algorithm starts by computing an observed test size corresponding to the

---

### Algorithm 5.1 Permutation test - Determining a p-value

---

**Require:** Compute an observed test statistic  $T_{obs}^2$  using eq. (5.6).

**repeat**

    Randomly shuffle the data of two groups,  $X_1, \dots, X_m, Y_1, \dots, Y_n$ .

    Calculate  $T_i^2$  for the  $i^{th}$  shuffle using eq. (5.6).

**until** B shuffles are done

**Require:** Estimate the p-value:  $p = \frac{1}{B} \sum_{i=1}^B I(T_i^2 > T_{obs}^2)$

---

true groupings of the data. Next, a repeated shuffling of data from the two groups, enables the algorithm to draw  $T_i^2$  samples from the null distribution. By generating enough  $T^2$  statistics, the approximate null hypothesis distribution is generated and can be compared to the observed value  $T_{obs}^2$ . This comparison is performed in the final step of the algorithm where the indicator function  $I(T_i^2 > T_{obs}^2)$  counts the number of null hypothesis observations that were larger than the true observation  $T_{obs}^2$ .

# Tissue Segmentation

---

## 6.1 Introduction

The amount of white matter (WM) lesions segmented based on brain magnetic resonance images (MRI) have previously been used as an image marker, for multiple sclerosis (MS) disease assessment [56]. Another usage of lesion segmentations is to examine population-wide topographical distributions of WM damage [28]. Both of these applications rely on volumetric binary lesion segmentations which a trained radiographer may spend hours to delineate. In addition, such manual segmentations may defer widely depending on the level and experience of the radiographer performing the segmentation. Automatic segmentations methods based on statistical models may help to improve the efficiency and consistencies of lesion segmentations.

One of the earliest works on automatic lesion segmentation was by Leemput et al. [155]. He suggested to detect lesions as outliers of a parametric model which is usually based on a Gaussian function with mean and variance parameters specifying the probabilities of the classes, WM, grey matter (GM) and cerebrospinal fluid (CSF). It was further suggested to combine the probabilities of the Gaussian model with a Markov random field (MRF) prior probability that favours segmentations that have spatial clustered voxels of the same class. The optimal solution of this problem was found iteratively through an expectation-

maximization (EM) algorithm which on each iteration updates the parameters of the Gaussian functions and subsequently classifies voxels according to the updated parameters. Since then, a large number of papers have explored similar approaches [182], [60], [166], [169] and tissue classification of brain MRI using MRF priors remain one of the most popular approaches.

We use a MRF inspired approach as well, but replace the Gaussian functions with non-parametric probability density functions. The probabilities functions are obtained from a K-nearest neighbour (K-NN) approach which has previously been shown to achieve state of the art performance [6]. The problem is solved using the iterated conditional modes (ICM) which is a computationally efficient solver. Using ICM allows the approach to be used in a semi automatic manner as a tool that may benefit radiographers. This efficient solver allows radiographers to do on-line adjustment on the smoothness of the segmentations after which they can manually edit segmentations to minimize false positive/negative voxel classifications.

The structure of this chapter is the following. Section 2 will introduce the multi modal features used to segment a brain into tissue classes. Section 3 explains how to perform segmentations based on K-NN, using MRF neighbourhood priors. In section 4, criteria for assessing the quality of the segmentations are described.

These sections form the basis for the paper described in chapter 11. The main findings of the paper are; 1) The inclusion spatial features are beneficial to segmentation while the benefits of including diffusion indices is less clear and 2) that the addition of the MRF neighbouring constraint leads to an improvement of segmentations compared to K-NN and yields favourable results compared to support vector machines (SVMs) [30] and the original implementation of the parametric approach in [155].

## 6.2 Image features

A variety of information could be used as features for the purpose of classifying the tissue type of a voxel. This includes intensity features (MRI) and spatial features (image coordinates) as described next.

## Intensity features

The intensities of three structural MRI are used as input features for the segmentation approach. They are an MPRAGE, a T2 and a FLAIR image. These contain different tissue contrasts, potentially boosting the performance of a classifier. Unfortunately the intensities of the structural images vary across the image domain due to magnetic field in-homogeneity of the MRI scanner. This artefact is removed using the N3 method [137] of Freesurfer which can be downloaded from

<http://surfer.nmr.mgh.harvard.edu/>. The classification approach assumes that the structural images of the same subject are in anatomical correspondence. This is ensured by intensity based registration using a rigid model and the optimality criteria of Mutual Information (MI) which is used to align the T2 and the FLAIR images with the MPRAGE image. Similarly diffusion MRI and the indices of fractional anisotropy (FA) and the mean diffusivity (MD) [41] were aligned with the MPRAGE.

## Spatial features

Spatial feature information such as the  $(x, y, z)$  coordinates of a voxel is useful information since the tissue classes of lesions, WM, GM and CSF occurs in certain regions of the brain. We explore two approaches for obtaining spatial features.

The first approach is based on ideas suggested in [6]. The intensity weighted centre of gravity of each 2D axial slice of the FLAIR image is determined and the coordinates of each axial slice are adjusted with respect to the axial centre of gravity, putting the coordinate at the centre of gravity to  $(0, 0, z)$ . These coordinates can then be used as spatial features. Note that the image coordinates along the longitudinal axis are unchanged by the centroid correction.

The second approach, is based on information contained in the SPM-MNI152 atlas. This T1-weighted image atlas contain WM, GM and CSF probability maps generated on the basis of healthy subjects. These maps encode the probability of observing either of the tissue types in a region of the brain. To use this atlas as a spatial prior, the T1-weighted image is non-rigidly registered (using SPM8) to the MPRAGE image of an MS patient and the deformation field of the non-rigid registration is used to deform the probability maps of WM, GM and CSF into the MPRAGE space. The deformed maps can then be used as spatial features.

## Skull removal

To limit the domain of the tissue segmentation problem the skull is removed from all image features. This is achieved using the SPM-MNI152 atlas and its associated probability maps. A binary mask is constructed in atlas space by a summation of the maps and thresholding of the summary mask. Using image registration the mask is spatially normalized to a subject space. A single morphological erosion is performed on the mask removing the outer boundary of the mask. All voxels not within the binary mask are dis-regarded by the segmentation method.

## 6.3 Markov random field segmentation

A Markov random field (MRF) approach classifies voxels while emphasizing spatially smooth segmentations. This is done by specifying a prior encoding the spatial smoothness and combining the prior with a likelihood probability. These are the components of Bayes formula. Therefore we shall initiate this section by introducing Bayes formula following which we give details on obtaining the likelihood and the prior.

### Bayes formulation

Bayes theorem [15]

$$P(\phi|X) = \frac{P(X|\phi) \cdot P(\phi)}{\sum_{\phi} P(X|\phi) \cdot P(\phi)} \propto P(X|\phi) \cdot P(\phi), \quad (6.1)$$

states that the posterior probability  $P(\phi|X)$  is proportional to the probability of observing  $X$  given the classification  $\phi$ , multiplied with the probability of observing  $\phi$  when nothing is known about  $X$ . These probabilities are commonly referred to as the likelihood and the prior. The denominator term is a normalizing constant which can be ignored. For the purpose of voxel classification  $X$  corresponds to the image features of a voxel and  $\phi$  is classification label.

If an image consists of  $n$  voxels, the posterior probability of observing a classification field across the image domain can be specified as

$$P(\phi_{1...n}|X_{1...n}) = \prod_{i=1}^n P(X_i|\phi_i) \cdot P(\phi_i) \quad (6.2)$$

To determine the most likely classification of eq. (6.2), requires specification of the model form of the likelihood and the prior. The likelihood is traditionally assumed to follow a Gaussian function [155], specified by a mean and variance parameters, or a mixture of Gaussians functions. We take another approach and estimate the likelihood of each voxel using a non-parametric approach where the probabilities arise through a K-NN classification scheme. Using a MRF formulation, the prior is specified to favour classifications that are spatially smooth, meaning it decreases the probability of singular voxel being classified differently from its neighbours.

Details on how to estimate the K-NN likelihood and specify the neighbourhood priors which result in a MRF problem formulation are given next.

### K-Nearest Neighbour likelihood

The Nearest Neighbour (NN) classifies an unseen voxel based on a training dataset but with no assumption about the form of probability function generating the intensities of the data [43].

We let  $X$ , denote an  $n$  dimensional vector of imaging features for a voxel in the training dataset. We write it as  $X = ([x_1, x_2, \dots, x_{n-1}, x_n], \phi)$ , to indicate that for each voxel there is both a feature vector and an associated class label  $\phi$ . A training dataset will consist of  $m$  training examples each with a feature vector and a classification label  $\phi$ . To classify an unseen voxel  $Y = [y_1, y_2, \dots, y_{n-1}, y_n]$ , the expression

$$j = \arg \min_i d(X_i, Y), i = 1, 2, \dots, m, \quad (6.3)$$

is evaluated for all training examples and the class label of  $X_j$  is assigned to the voxel in  $Y$ . We use the Euclidean squared difference  $d(X, Y) = \|X - Y\|^2$ , to find the nearest neighbours.

To turn the NN classifier into a K-NN classifier, the  $K$  nearest neighbours with the smallest Euclidean differences are kept and classification is declared based on the most frequent class label. The K-NN solution is based on the freely available software package FLANN (<http://mloss.org/software/view/143/>) [110] which requires specification of the parameter  $K$ . We have experimented with  $K$  in the range [40 : 220] and found  $K = 100$  to offer good lesions segmentations.

#### The training dataset:

The training dataset consist of feature vectors from four classes each with a distinct label,  $\phi = \{CSF = 1, GM = 2, WM = 3, LES = 4\}$  corresponding to cerebrospinal fluid (*CSF*), gray matter (*GM*), white matter (*WM*) and lesions

(LES). We construct the training dataset to ensure all classes are equally represented by randomly selecting an  $X$  from each class until one of the classes become empty. To ensure equal importance of all imaging features, each feature is mean centered and scaled with respect to variance.

### From K-NN to probabilities:

The output of the K-NN classifications are four, 3D images containing the number of votes in favour of a given class. The Bayesian formulation of eq. (6.2) requires that these images be transformed into voxel-wise probabilities  $P(X_i|\phi_i)$ . They are transformed by dividing the number of votes for a given label by  $K$ . From these probability maps a threshold can be set to obtain binary segmentations of the desired tissue class. The purpose of this threshold is to control the ratio of false/true positive classifications. We choose this threshold as to optimally classify lesions calibrated according to the dice score similarity criteria [45]. Instead of thresholding the lesion probability maps, the threshold is used to scale the lesion probabilities relative to the three other probability maps such that we can continue working with the probability that a voxel takes on a given label. The scaling is done such that the most likely classification of the rescaled probabilities, correspond to the result of thresholding the initial lesion probability map.

## Specifying the MRF through neighborhood priors

A MRF is specified using a Gibbs distribution

$$P(\varphi) = \frac{1}{Z} e^{-\sum_c V_c(\varphi)} \quad (6.4)$$

where  $c$  denotes an index over a number of neighbouring voxels,  $V_c$  denotes the neighbourhood interaction function and  $Z$  is constant, usually ignored.

To form a MRF formulation, the K-NN likelihood is inserted it into eq. (6.2) and combined with a simple neighbourhood prior that follows the Gibbs distribution. The posterior probability of a MRF is

$$P(\phi_{1...n}|X_{1...n}) = \prod_i^n P(X_i|\phi_i) \cdot e^{-\sum_{c \in n(i)} V_c(\phi_i)} \quad (6.5)$$

$$P(\phi_{1...n}|X_{1...n}) = \prod_i^n P(X_i|\phi_i) \cdot e^{-\sum_{j,k,l \in n(i)} \beta(\phi_i, \phi_{jkl})} \quad (6.6)$$

The exponential part of the last equation specifies the multi class neighbourhood interaction function. The local neighbourhood  $n(c)$  of a voxel is defined

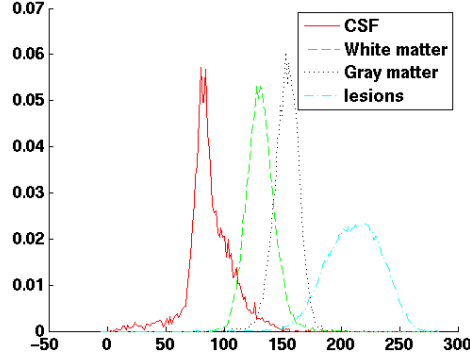


Figure 6.1: Shows the intensity histograms of a FLAIR image derived from four different tissue classes. A considerable amount of class distribution overlap is observed. Our segmentation method resolves some of this ambiguity by using several intensity features, spatial features and MRF neighbourhood priors.

as the 6 nearest neighbours in a 3D regular grid configuration. The interaction function expressed by the exponentiated summation, considers the  $i$ th voxel and penalize if the  $(j, k, l)$  voxels of the local neighbourhood  $n(c)$  differs from the class of the  $i$ th voxel. The penalties are specified by a  $4 \times 4$  matrix  $\beta$  which contain the penalty magnitudes associated with neighbour classification transitions. Using the notation that  $\phi = \{CSF = 1, GM = 2, WM = 3, LES = 4\}$ , it is possible to penalize  $LES$  classes being spatially close to voxels of  $GM$  classes, by setting the value of  $\beta(2, 4)$  and  $\beta(4, 2)$  to something larger than 0. If such voxel neighbourhood configurations occur it will decrease the probability of the segmentation according to eq. (6.5). To avoid penalizing voxel transitions, the matrix entries should be 0. Our specific implementation penalize the transitions of  $Gm \leftrightarrow LES$  and  $CSF \leftrightarrow LES$  using the matrix

$$\beta = \begin{bmatrix} 0 & 0 & 0 & 0.1 \\ 0 & 0 & 0 & 0.1 \\ 0 & 0 & 0 & 0 \\ 0.1 & 0.1 & 0 & 0 \end{bmatrix}. \quad (6.7)$$

The MRI intensity distribution between tissue classes usually have an amount of overlap as shown in Figure 6.1. This intensity overlap often leads to misclassification of tissue and by using the neighbourhood prior some of this ambiguity can be resolved.

## An optimal solution

Having specified the prior and the likelihood, the following maximization is solved

$$I = \arg \max_{\phi_{1\dots n}} P(\phi_{1\dots n} | X_{1\dots n}). \quad (6.8)$$

$I$  denotes an image of the optimal classification labels which are estimated iteratively via the ICM [18] method. One iteration of the ICM consist of a checker-board traversal of the image, first considering the local probability of voxels on the white chess fields, changing the classifications if justified by the posteriors and second considering the voxels coinciding with the black chess fields changing only the classifications if justified by the posteriors. Once the classifications no longer change during iterations convergence is assumed. The ICM approach usually only converges to a local solution. Methods exist such as simulated annealing [85] or graph cuts [23] have the potential of escaping local cost function minima but were not explored.

An example of solving the problem using ICM is shown in Figure 6.2. It shows the posterior probability maps of the *CSF*, *GM*, *WM* and *LES* classes overlaid on a FLAIR image. We note how some of the GM is cut off due to the skull removal. This is of little consequence since we are focused on WM lesion segmentation however if we where interested in using the GM volume as an imaging marker, the skull removal would need to be altered.

## 6.4 Assessment of segmentation quality

### 6.4.1 Similarity scores

To rate the performance of a single segmentation, the similarity index (SI) based on the dice score [45] and the overlap fraction (OF) are used. Both of these measures compare the segmentation results of the proposed method with the segmentations of the radiographers. The performance measures are evaluated according to eq. (6.9)

$$SI = \frac{2|V_{ref} \cap V_{seg}|}{|V_{ref}| + |V_{seg}|}, \quad OF = \frac{|V_{ref} \cap V_{seg}|}{|V_{ref}|}, \quad (6.9)$$

where  $V_{ref}$  is the assumed segmentation of the radiographer and  $V_{seg}$  is the segmentation of the method. The range of these measures are  $[0,1]$  with a higher value indicating that the segmentations of  $V_{ref}$  and  $V_{seg}$  are very similar.

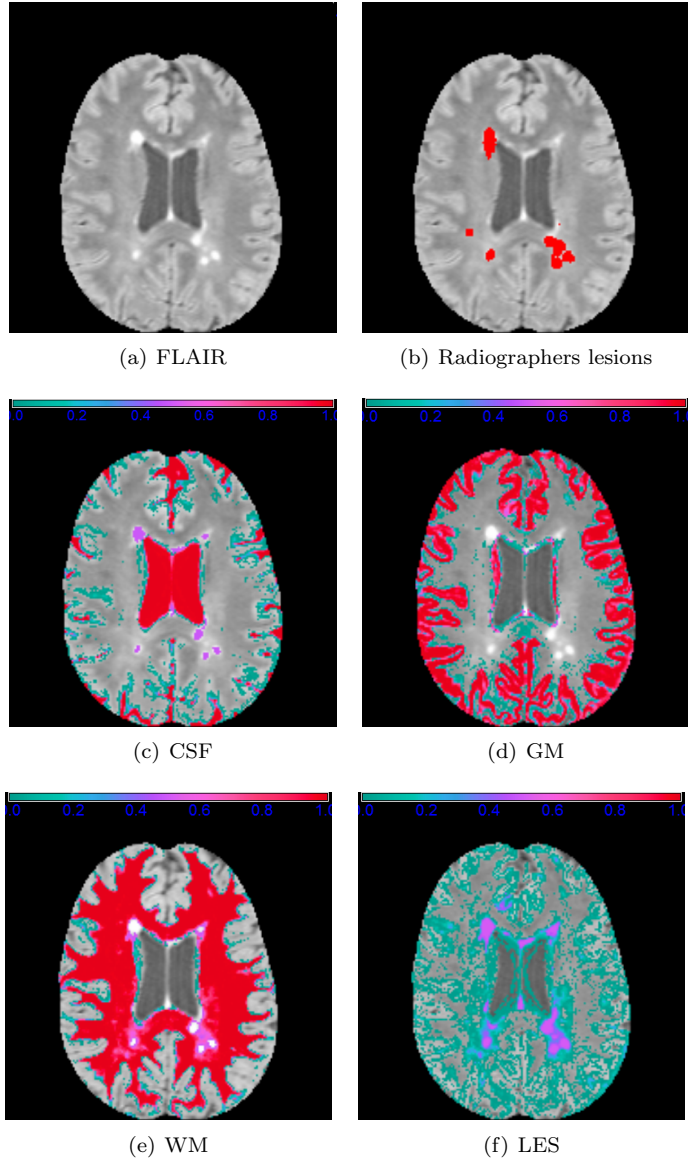


Figure 6.2: Shows the results of tissue segmentation using the KNN+MRF approach, using neurological convention. (a) Shows an axial slice of a FLAIR image while (b) shows the same slice overlaid by lesion masks annotated by a radiographers. Using the same slice (c-f) shows the posterior probability of a voxel belonging to *CSF*, *GM*, *WM* and *LES* after solving eq. (6.8). To supply spatial context to the visualization all have been overlaid on a FLAIR image.

## Cross validation

To rate method performance across multiple subjects one could train the method on all subjects, apply it to segment all subjects and evaluate the average similarity scores with respects to the radiographers segmentations. Such an approach will generally overestimate the performance since the voxels being classified are present in the training dataset. This problem is solved using cross validation. The idea of cross validation is to leave out a subset of data from the training dataset and evaluate performance by classifying the left out subset.

We use leave out cross validation, both to train and test the performance of the method. The total amount of subjects used for this purpose are 15. During the training phase, 10 subjects are included for which 10 leave-one out validations are performed. This results in 10 performance scores which are used to asses method performance as a function of  $K$ ,  $\beta$ . Once these have been fixed, test performance is evaluated by segmenting the five subjects which were initially left out from the training. The average of their segmentation performance scores indicate test performance.

To improve the validity of the results the training and testing validation is repeated three times. Each time with a randomized division of the 15 subjects into training and test sets. See the paper in chapter 11 for further details and results of this validation.

# Contribution Overview

---

This chapter summarizes the main methodological developments and findings presented in the manuscripts of part II.

## 7.1 Correcting geometric distortions of Echo Planar Imaging using demons and reversed phase encoding

Diffusion weighted images (DWIs) acquired using echo planar imaging (EPI) sequences are subject to a number of imaging artefacts. One of these artefacts is the geometric distortions caused by magnetic field inhomogeneities which are particularly large near air-tissue interfaces. The artefact manifests as a local displacement of voxels equivalent to tissue expansion or compression. Correction of the geometric distortion is important to obtain anatomical correct DWIs enabling alignment with structural MRI and prompting more reliable results (biomarkers) of any posthoc analysis of the images.

The work presented in chapter 8 solves the distortion correction problem by implementing a method based on the idea of Chang et al. [31]. It relies on the fact

that reversing the phase encoding direction of an EPI sequence leads to oppositely directed image distortion which can be used to correct distorted images. If one can identify corresponding voxels in two oppositely distorted images of the same subject, it is possible to infer the true location of the voxels by taking the midway distance between the correspondences. We use intensity based image registration to establish these correspondences by estimating the full deformation between two oppositely distorted images. The registration problem is solved using Thirion's demons [147] in a way that accounts for the intensity build up also caused by the distortion artefact. The estimated deformation field is divided by 2 to yield a voxel displacement map for correcting EPI data.

The results of the method are compared to other popular correction techniques such as the field map (FM) [79] and the point spread function (PSF) approach [178].

A comparison of the methods is performed by applying all three methods to the first non-diffusion weighted (b0) of five healthy subjects. To assess the quality of each undistorted b0 image, it is compared to a rigidly aligned minimally distorted MPRAGE. The comparison is performed using mutual information (MI), with higher MI suggesting larger image similarity. To increase specificity of the comparisons, MI was evaluated within smaller regions of interest (ROIs) with the conclusion that our proposed method was consistently amongst the top performing within all ROIs. It did however turn out to be inferior in one of the five patients. Visual inspection of the FM corrected b0 of this patient seemed to be slightly more similar to the MPRAGE than the registration approach, particularly near image boundaries at the frontal lobe. It is however noted that the difference appeared very small but it seems enough to change the MI comparison score. To emphasize how close they were it is noted that the difference in MI was at the third decimal place. The MI was 0.8208 for the registration based approach and 0.8278 for the FM approach. To put this number into context, the patient where the two approaches differ the most achieved an MI of 1.0721 for the FM approach and an MI of 1.1706.

The proposed method was not used in the diffusion MRI (dMRI) MS studies of the thesis since these EPI sequences were not acquired using additional phase reversed images as required by the method. The results of the study indicates that the method could be beneficial in future studies, since it doesn't appear to compromise image quality while reducing scan time in comparison to the FM and PSF approaches.

## **7.2 Tract-oriented statistical group comparison of diffusion in sheet-like white matter**

Identifying specific structures of the brain where the pathology of MS patients differs from healthy subjects could add knowledge about MS and may be useful for developing image based biomarkers for disease assessment.

The paper presented in chapter 9 proposes and validates a method for doing tract-oriented group analysis of diffusion indices in WM tracts with sheet-like shape topology. The analysis consist of building an atlas space where sheet-like models of WM tracts are made of the corpus callosum, the inferior longitudinal fasciculus, the uncinate fasciculus, the superior longitudinal fasciculus, the corticospinal tract and the inferior fronto-occipital fasciculus. Multivariate diffusion indices are sampled on the sheet-like models of the tracts and used to build tract-oriented statistical models. Statistical analysis of the model parameters is used to determine group difference. The usage of sheet-like models makes it possible to do statistical analysis of the diffusion indices on the entirety of WM tracts. This isn't possible using tube-like models which has previously been suggested as the tract based model in work by Goodlett et al. [70].

Since MS is known to significantly alter diffusion indices of WM [36], we demonstrate the methodology on MS patients revealing significant difference compared to a population of healthy subjects. In particular we noted a strong consistent difference between the two groups, in the splenium of the corpus callosum. We were however unable to detect whole-tract differences between the clinically defined, relapse remitting (RR)-MS and secondary progressive (SP)-MS phenotype groups. We expect the approach may be useful in a variety of other studies investigating if the diffusion indices along a sheet-like manifold give rise to significant group difference.

## **7.3 Secondary progressive and relapse remitting multiple sclerosis leads to widespread decreased anatomical connectivity**

Brain disconnection plays a major role in determining the severity of disabilities in MS. We use the method of anatomical connectivity mapping (ACM) to examine how the connectivity reflects the state of MS patients.

The ACM is estimated in way that is particularly suited for group studies. This

approach minimizes the potential of the ACM estimates being biased due to cross subject brain shape and size. A problem described by Bozzali et al. in [24] who proposed linearly scaling the ACM with respect to brain size as a solution to this problem. We suggest to minimize the problem by first estimating the voxel displacement (using image registration) from subject space to a common atlas space and to use the displacement field to deform the multi-tensor volumes from native space into the common atlas space. In this space, whole-brain probabilistic tractography is performed and converted into an ACM. Using this estimation approach, the ACMs of a study will be in approximate anatomical correspondence enabling voxel-based analysis (VBA).

In the manuscript of chapter 10, ACM is used to examine the hypothesis that the phenotypes of RR-MS and SP-MS experience decreased connectivity compared to healthy controls. We find decreased connectivity within the WM of MS patients and from summary WM statistics of the ACMs we note a tendency of SP-MS having lower connectivities compared to RR-MS. VBA between these two phenotypes reveal that ACM can detect differences between them, resulting in significant difference in the bilateral projection fibers of the motor tracts. Complementary to these finding a VBA based on FA was unable to reveal similar significant effects. In addition we find a general increase in correlation between EDSS and ACM compared to the correlation between FA and EDSS. In summary, it is shown that ACM is able to reveal MS disease-related changes that could not otherwise be seen.

## 7.4 Segmenting Multiple Sclerosis Lesions using a Spatially Constrained K-Nearest Neighbour approach

Whole-brain measures of pathologically diseased tissue are used in multiple sclerosis (MS) treatment studies as unspecific markers of disease severity [57]. The T2-weighted lesion load is one of these markers. It has been found to yield moderate disease score correlation with the extended disability status scale (EDSS) and has been used in studies throughout the last 20 years [56], [114], [90], [57]. It is estimated by identifying white matter (WM) lesion voxels from a T2-weighted magnetic resonance image (MRI) and summing the voxel count. Another usage of lesion segmentations is to examine population-wide topographical distributions of WM damage [28]. These applications rely on volumetric binary lesion segmentations. Manually delineating lesions is a tedious and time consuming task. Therefore computerized segmentation methods are considered as highly useful tools for improving efficiency.

The manuscript in chapter 11 suggests a computerized method for segmentation of WM lesions based on multi-modal MRI. The method combines a voxel-wise K-nearest neighbour classification scheme with a prior assumption that segmentations should be smooth.

It investigates the discriminative performance of several image features encompassing structural MRI (MPRAGE, FLAIR, T2), dMRI (fractional anisotropy (FA), mean diffusivity (MD)) and spatial coordinates (centroid corrected coordinates, atlas based tissue probability maps). The combination of MPRAGE, T2, FLAIR, fractional anisotropy and tissue probability maps, are found to give the best segmentation performance with a median Dice score above 0.7, derived from an unseen test dataset. The improvement due to the inclusion of the smoothness prior is found to be minor. The performance of the method is compared to the method of Koen et al. [155] and support vector machines [30] achieving median Dice score 0.453 and 0.48 for the two respective approaches. Compared to the performance of the inter-rater and intra-rater of two radiographers our approach was inferior. Correspondingly, the quality of segmentations is likely to be inadequate in a clinical setting. However the approach could be followed by a post-processing stage of manual lesion editing conducted by radiographers. Each clinician would then be able to select a desired level of segmentation smoothness from which they prefer to do manual editing. Or alternatively the smoothness could perhaps be decided based on phenotype or the EDSS scores of the last neurological exam. Overall the approach has the potential to improve the efficiency of the clinicians (radiographers).

## 7.5 Conclusion

To fulfil the objectives of the thesis, methodology for determining MS biomarkers from MRI images were proposed.

Biomarkers based on dMRI requires correction of image distortions and we showed how a geometric distortion correction can be achieved using an additional phase reverse image acquisition and image registration. This resulted in the same performance as alternative methods but demanding less scan time.

Two dMRI based analysis methods were proposed, intended for group-wise studies between clinically different disease groups and healthy controls. A tract-oriented statistical group comparison of sheet-like WM enabled us to detect whole-tract difference between a group of healthy controls and MS patients on 11 WM fascicles. We were unable to discriminate the RR-MS from the SP-MS using this approach. It was however possible to detect localized differences us-

ing the ACM technique where a group-wise, voxel-based analysis revealed large widespread connectivity differences between the ACM of healthy subjects and MS patients but also between the RR-MS and the SP-MS phenotypes. The fact that we were unable to make such findings based on voxel-based FA analysis and the fact that ACM achieved widely better EDSS disease score correlation compared to FA suggests ACM to be more sensitive towards measuring the disease severity state of MS.

A method for segmenting WM lesions was found to work best with a combination of MRI modalities and a spatial input feature. The method performed better than competing methods but was inferior to that of trained clinicians. As a consequence, the usage of the method in a clinical setting will have to be combined with manual editing of the WM lesion segmentations output by the method.

In conclusion we have applied various analysis method to an MS study enabling us to derive pathology and non pathology specific image markers with the ability of revealing disease-related abnormalities and detecting phenotype differences not seen using traditional dMRI derived indices (FA).

Part II

Contributions



## CHAPTER 8

# **Correcting geometric distortions of Echo Planar Imaging using demons and reversed phase encoding**

---

Published in proceedings of, International Society for Magnetic Resonance in Medicine (ISMRM), 20th annual meeting, pp.2578, Melbourne, 2012.

Correcting geometric distortions of Echo Planar Imaging using  
demons and reversed phase encoding

*M. Lyksborg<sup>1,2</sup>, H. Lundell<sup>2</sup>, N. Reislev<sup>2</sup>, H. R. Siebner<sup>2</sup>, R. Larsen<sup>1</sup>,  
T. B. Dyrby<sup>2</sup>*

*1. Technical University Of Denmark, Kgs. Lyngby, Denmark*

*2. Danish Research Centre for Magnetic Resonance, Hvidovre, Denmark*

## Introduction

Echo Planar Imaging (EPI) sequences are subject to imaging artefacts, caused by subject motion, eddy currents effects and field inhomogeneity distortions (susceptibility) causing a geometric displacement of voxel intensities along the phase encode direction. Inhomogeneity correction is important to obtain an anatomical correct image which can be aligned with structural MR images. To estimate the displacement field that allows correction, we extend an existing technique, based on acquiring a full EPI sequence and one additional EPI image acquired with reversed gradient polarity along the phase encoding direction [2, 6]. The EPI with reversed gradient polarity contains the same intensity information as a corresponding image of the EPI sequence but with distortions causing voxel shifts in the reverse directions. To find the displacement field between two reversely distorted EPI's, an image registration problem is solved as in [2]. We propose to use the simpler, more efficient Thirion's demons algorithm [3, 4] and suggest a different registration pipeline for obtaining the displacement fields and name it phase reversed demons (PRD). The PRD is compared to two other correction methods that require additional MRI sequences, leading to increased scan time. These are the gradient field map (FM) [1] and the point spread function (PSF) [5]. We compare the three methods applied to five subjects. The results are compared visually and quantitatively by estimating the statistical dependence with a structural T1-weighted image. The quantitative results indicate that the (PRD) approach is competitive by being more similar with the structural image but inspection of regions in subjects also demonstrates individual cases where the other methods are favourable.

## Method

**Diffusion data and preprocessing** Five subjects were scanned, acquiring a structural T1-weighted (MPRAGE) (TR=1900 ms and TE=2.32 ms, 224 slices with  $0.9 \text{ mm}^3$  isotropic voxels) and a whole brain diffusion weighted (DWI) EPI using Twice-Refocused spin echo sequence [7] (TR=11440 ms, TE=89 ms, Echo Spacing=0.66 ms, 61 slices, with  $2.3 \text{ mm}^3$  isotropic voxels and GRAPPA=2), consisting of 10 b0 and 61 diffusion weighted images, at b-value  $1500 \text{ mm}^2/\text{s}^2$ . The images were acquired on a Siemens Verio 3T MR scanner using a 32 channel head coil. We correct the DWI using a displacement field, estimated with the three approaches:

**Image registration (PRD)** As mentioned in the introduction, this method requires one additional b0 with same sequence parameters as the b0s of the DWI but with reversed gradient polarity. Thirion's demons estimates the displacement field  $\phi$ , as the minimizing solution to a non-linear sum of squares cost function based on the differences between a displaced b0 image and a b0 image with reversed gradient polarity. To increase numerical stability of the cost function optimization, Thirion's demons incorporate a diffusion prior in a way particularly efficient, compared to other registration implementations as argued in [3]. The displacement field for geometrically correcting EPI images is given by half the estimated displacement field,  $\phi/2$ .

**Avoiding local registration minima's of the cost function** A three stage successive registration is proposed to avoid getting stuck in any local minima's of the cost function. For each of these three stages, the solution of the previous stage is used as a start guess for the next, similarly the influence of the diffusion prior is decreased at each stage. The procedure is: 1) Estimate the field between the two background thresholded/smoothed b0 images. 2) Estimate the field between two double thresholded and smoothed b0 images using a threshold for the background and one for the Cerebral Spinal Fluid (CSF). 3) Estimate the field based on the true intensity images. Note that we only introduce intensity modulation into the image registration cost function during stage 3 of the image registration. Intensity modulation is done by multiplying the corrected EPI images with the factor  $(1 + (\text{Jacobian of the field}))$ .

**The field map (FM)** A double gradient echo sequence was acquired on the scanner to estimate the b0 field inhomogeneity with TR=479 ms, TE1=4.92 ms, TE2=7.38 ms and isotropic voxel resolution of  $3 \text{ mm}^3$ . Using the field map

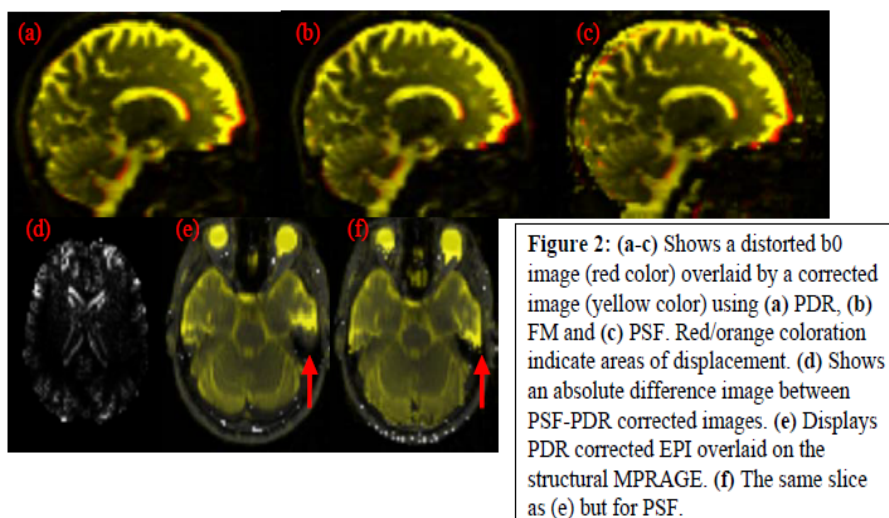
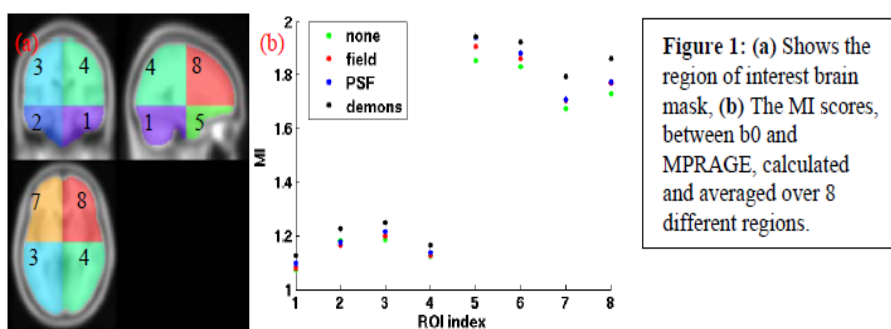
toolbox of SPM8 [1] the displacement field was estimated and re-sliced to DWI resolution.

**The PSF** Point spread function was mapped using the same EPI parameters as the b0-acquisition with an additional sequence parameter PSF rFoV=4, displacement maps were then calculated using online software, see [5].

**Method comparisons** The first b0 of the DWI sequence is corrected using the three methods and compared to the minimal distorted MPAGE, used as the gold standard of an undistorted image. Using mutual information (MI), the MPAGE and its affiliated brain mask shown in Figure 1 were rigidly aligned to the corrected b0 image. The mask consists of eight labelled regions allowing for region wise analysis. Within the mask, intensities were scaled to the range [0 512] and MI estimated using 512 histogram bins. MI is calculated for each subject and for each region of interest across subjects. MI is a suitable criterion that quantifies the dependence between the distributions of the two images with increased dependence suggesting higher similarity.

## Results

The MI calculated within each subject revealed that the PDR method was better in 4 of 5 subjects while the FM was better in the last subject. The comparison of methods based on MI scores is plotted in Figure 1 and show that the PDR perform similarly or better than the other methods in most regions. Figure 2(a-c) allows for a visual comparison of a corrected b0 using the 3 different methods, demonstrating how similar they are. To emphasize where/how the methods actually differ, Figure 2(d) shows an absolute difference between a PSF and PDR corrected axial slice. Largest within mask differences are observed near CSF/tissue edges. Since PDR has increased MI in these regions, this could indicate increased accuracy of the PDR. To emphasize where we found PSF to be preferred, Figure 2 (e-f) compares PSF/PDR in region 5, 6 near the Petrous temporal bone. Arrows indicate where PSF had better performance.



## Discussion

The PRD method demands less additional scan time compared to FM and PSF while achieving similar performance. Because it can be further improved, it is a viable alternative for inhomogeneity correction. We observed needs for improvements in brain region 5 and 6 where it was sometimes worse than PSF but on par with the FM (results not shown). Speaking against PSF is the sensitive to brain masking. For instance in Figure 2 (c) is shown an unmasked image with structures appearing outside the brain. About the MI measure; It is sensitive to choosing appropriate histogram bin sizes which may alter the conclusions. However, we found that conclusions were robust for both 256 and 512 number of bins. We observed magnitude difference in MI in frontal regions 5-8 compared to 1-4, possibly caused by more structural details in the back of the brains.

## Acknowledgement

This research was supported by the Danish Council for Strategic Research.

## References

- [1] Jezzard et al., 1995, MRM. [2] Holland et al., 2010, Neuroimage. [3] Vercauteren et al., 2008, Neuroimage. [4] Thirion, 1998, Med. Image Anal. [5] Zaitsev et al., 2004, MRM. [6] Chang et al., 1992, Med Imaging, [7] Reese et al., 2003, MRM.

## CHAPTER 9

# **Tract-oriented statistical group comparison of diffusion in sheet-like white matter**

---

Published in Proceedings of the 10th IEEE International Symposium on Biomedical Imaging: From Nano to Macro, April 7th-11th, San Francisco, 2013.

# TRACT-ORIENTED STATISTICAL GROUP COMPARISON OF DIFFUSION IN SHEET-LIKE WHITE MATTER

*M. Lyksborg<sup>1,2</sup>, T. B. Dyrby<sup>2</sup>, P. S. Sørensen<sup>4</sup>, M. Blinkenberg<sup>4</sup>, H. R. Siebner<sup>2</sup>,  
D. Alexander<sup>4</sup>, R. Larsen<sup>1</sup>, H. Zhang<sup>4</sup>*

<sup>1</sup>Technical University of Denmark, Informatics and Mathematical Modeling, Kgs. Lyngby, Denmark

<sup>2</sup>Danish Research Centre for Magnetic Resonance, Cph. University Hospital Hvidovre, Denmark

<sup>3</sup>Danish Multiple Sclerosis Research Center, University of Copenhagen, Denmark

<sup>4</sup>Centre for Medical Image Computing, University College London, United Kingdom

## ABSTRACT

Identifying specific structures of the brain where pathology differs between groups of subjects may aid to develop imaging-based markers for disease diagnosis. We propose a new technique for doing multivariate statistical analysis on white matter tracts with sheet like shapes. Previous works assume tube-like shapes, not always suitable for modelling the white matter tracts of the brain. The tract-oriented technique aimed at group studies, integrates the usage of multivariate features and outputs a single value of significance indicating tract-specific differences. This is in contrast to voxel based analysis techniques which outputs a significance per voxel basis, and requires multiple comparison correction.

We demonstrate our technique by comparing a group of controls with a group of Multiple Sclerosis subjects obtaining significant differences on 11 different fascicle structures.

**Index Terms**— Diffusion MRI, Continuous Medial Representation, White Matter Atlas, Multiple Sclerosis

## 1. INTRODUCTION

We propose a method for doing tract-oriented group-wise analysis using multivariate diffusion indices, suitable when a white matter (WM) structure (a tract) can be modelled as a sheet-like manifold. Such techniques may be used for studying diseases and deriving disease related markers from Diffusion Weighted Imaging (DWI), an imaging modality particularly sensitive to WM abnormalities because it can provide markers sensitive to micro-structural changes in WM. This is quantified by the Diffusion Tensor (DT) model, fitted to the DWI of each voxel from which, the principal direction (PD) (the most probable fibre direction), and the scalar diffusion indices, Mean Diffusivity (MD), Fractional Anisotropy (FA) and the Tensor Norm (TN) can be estimated [1].

Voxel Based Analysis VBA [2] and Tract Based Spatial Statistics (TBSS) [3] are among the popular methods for testing group differences based on diffusion indices. Some of the deficiencies that our approach does not suffer from are that VBA usually requires arbitrary smoothing of data, due to problems with inaccurate image registration failing to properly align corresponding structures while also suffering from problems due to multiple voxels comparisons. Being voxel based these methods are unable to answer hypothesis relating to the entirety of a tract.

Goodlet et al. [4] suggested a solution to this problem, by applying functional statistical analysis to diffusion indices restricted to tracts with tube-like shape. This approach gracefully handles problems due to inaccurate registration using a reduced statistical model avoiding the multiple comparison problem by restricting analysis to the model space. Since tracts are generally not tubular, we propose to extend the approach to tracts with sheet-like manifold shape [5].

Our approach builds an atlas space where sheet-like models of tracts are made of the corpus callosum (CC), the inferior longitudinal fasciculus (ILF), the uncinate fasciculus (UNC), the superior longitudinal fasciculus (SLF), the corticospinal fasciculus (CST) and the inferior fronto-occipital fasciculus (IFO). Multivariate diffusion indices are sampled on the tracts and used to build tract-oriented statistical models. Statistical analysis of the model parameter space is used to determine group difference. This approach inherits all the best features of [4] while allowing to analyse a wider range of WM structures. For instance, sheet-like models makes it possible to do statistical analysis of the entire CC.

Since Multiple Sclerosis (MS) is a disease known to significantly alter diffusion indices of WM [6], we demonstrate the methodology on data from an ongoing MS study.

## 2. DATA

Thirty-five MS subjects with a Secondary Progressive (SP) condition (n=14) or a Relapse Remitting (RR) condition (n=21), were included. Control subjects (n=25) were age and gender matched with the MS group. The study was ethically approved.

For each subject, a whole brain diffusion MRI was acquired consisting of 71 sequentially recorded images, including 10 b0 images with no diffusion sensitivity and 61 sensitive to diffusion, with a b-value of  $1200 \text{ s} \cdot \text{mm}^{-2}$  using an isotropic voxel size of  $2.3 \text{ mm}^3$  and an image matrix of size  $96 \times 96 \times 61$ . To make possible retrospective inhomogeneity distortion correction, a field map sequence was acquired.

We retrospectively correct for image artefacts due to motion and eddy current effects by co-registering the DWIs with the first b0 image of the sequence, using a 12 parameter affine model while also accounting for inhomogeneity distortions. The DWIs were re-sliced into the space of the first b0 image.

The DTs are fitted non-linearly using a Levenberg-Marquardt optimizer, resulting in a 4D DT volume.

## 3. METHOD

The proposed method, as shown in Fig. 1, consists of four steps. First, we build a DT atlas to establish the spatial correspondence across study subjects, a prerequisite to group-wise comparison of corresponding WM tracts, and to delineate major tracts. Second, we construct a skeleton-surface-based geometric model of each tract to provide a shape-based coordinate system of the tract interior for efficient sampling of its diffusion properties. Third, we derive a statistical model of each tract that summarizes its diffusion properties with a multivariate function defined on its skeleton surface. The final step applies the statistical model to carry out tract-oriented hypothesis testing that considers each tract as a whole.

### 3.1. Atlas

A DT atlas is built from the control subjects to capture the normal characteristics of WM tracts. The construction uses DTI-TK, implementing a state-of-the-art tensor-based registration [7] and an iterative bootstrap procedure to simultaneously estimate a cohort-specific atlas and the correspondence among the cohort subjects [8]. The MS subjects are subsequently registered to the control DT atlas using DTI-TK.

Finally, tensor-deflection tractography [9] is used to track eleven WM fasciculi, based on recommendations in [10] and streamline termination criteria of  $\text{FA}=0.15$ .

### 3.2. White Matter Models

We derive the skeleton-surface-based geometric model of each segmented tract using deformable modelling with the continuous medial representation (cm-rep) as described in [5]. The cm-rep provides a natural framework to describe the geometry of sheet-like structures. It represents the skeleton of each structure with a 2-D surface mesh  $m$ . Each vertex of the skeleton mesh stores the thickness of the structure at that location, which is collectively known as the radial field  $r$ . Together, it establishes a curvilinear shape-based coordinate system of the entire interior of the structure. The second box in Fig. 1 illustrates the cm-rep using a 2-D example where the 2D skeleton curve  $m$  is coloured in green and the radial field  $r$  is shown as blue circles.

### 3.3. Tract-Oriented Statistical model

The purpose of building a statistical model is to get a compact functional description of diffusion indices parametrized as a function of a sheet-like manifold. Such a model has the benefit of taking care of the inherent high-dimension, low-sample-size problem.

The basis of the statistical model is a linear model used to describe the variation across the population. To build the model, diffusion indices are sampled along the spokes of the cm-rep model, shown in the second box of Fig. 1. The spokes shown in red, are used to sample data on both sides of a manifold and the average of these samples are projected onto the medial sheet  $m$ . For the  $i$ th subject, we can express these samples as a function on the sheet  $f_i(s) : s \in m$ . Based on the sample functions for  $n$  subjects, the sampling correlation is estimated

$$c(s, t) = \frac{\sum_{i=1}^n (f_i(s) - \bar{f}(s))(f_i(t) - \bar{f}(t))}{\sqrt{\sum_{i=1}^n (f_i(s) - \bar{f}(s))^2 \sum_{i=1}^n (f_i(t) - \bar{f}(t))^2}}, \quad (1)$$

	CC	CST-L	CST-R	UNC-L	UNC-R	SLF-L	SLF-R	ILF-L	ILF-R	IFO-L	IFO-R
Cont vs. MS	*	0.0004	0.0009	0.0041	0.0002	0.0025	0.0020	0.0002	0.0002	*	0.00002
RR vs. SP	0.38	0.1960	0.1130	0.0599	0.1931	0.0440	0.6980	0.9860	0.1238	0.7660	0.1040

**Table 1:** Results of permutation test in PCA space testing the equality of group means. The top row indicates which tracts are tested while R, L refers to right or left hemisphere structure. The smallest significance values resolved is larger than 1/50000, thus a significance of \* means smaller than 1/50000.

where  $s$  and  $t$  refers to positions on the manifold and  $\bar{f}(s)$  is the cross subject mean at position  $s$ . The linear model basis  $\xi$  is estimated by an eigen decomposition of the correlation matrix, satisfying eq. (2)

$$\int c(s, t)\xi(t)dt = \lambda\xi(s) \quad (2)$$

This is a Principal Component Analysis (PCA), with the eigenvectors in  $\xi$  and the eigenvalues in  $\lambda$ . The linear component parameters of the  $i$ th subject are estimated using

$$b_i = \int \xi(t)(f_i(t) - \bar{f}(t))dt. \quad (3)$$

Exact reconstruction of  $f_i(s)$  is possible from  $b_i$  but since  $f_i(s)$  is affected by noise, it is assumed that the least influential components can be removed. Only model components with eigenvalues larger than the mean eigenvalue of all the components are kept which is equivalent to Kaisers rule [11].

### 3.4. Group-Wise Comparisons

To do comparisons, Hotelling's squared t-test is used

$$T^2 = \frac{(n_x n_y)}{(n_x + n_y)} (\bar{x} - \bar{y}) S^{-1} (\bar{x} - \bar{y}). \quad (4)$$

The mean model parameters of the two groups are collected in vectors  $\bar{x}$ ,  $\bar{y}$  and the pooled covariance matrix is estimated in  $S$ . We utilize permutation tests [12] to determine the test size distribution under the assumption of a true  $H_0$  hypothesis(equal means) to determine the significance level. The number of permutations fixed at 50000. To asses the importance of spatial location, the linear discriminant score  $S^{-1}(\bar{x} - \bar{y})$  is projected from PCA space to sample space where visualization and interpretation is possible.

## 4. RESULTS

The method was evaluated using the indices of FA and TN and hypothesis tests performed for the CC, the CST, the ILF, the UNC, the SLF and the IFO. The significance of the tracts specific tests are listed in Table 1 and suggest a difference between MS and controls on all tracts while a comparison of the groups RR and SP showed weak evidence of WM difference in the UNC-L and SLF-L.

We find that the first principal component parameter of any tract distinguishes controls from the MS subjects, illustrated in Fig. 2(a). The control group has a tighter distribution, attributed to less variation in the control group compared to the MS group which is reasonable due to the heterogeneous nature of MS. MS subjects are found on the positive axis while controls are on the negative. To further explore this component, Fig. 2(b)-(c) visualizes the change of setting  $b_1$  to plus its standard deviation and reconstructing FA and TN changes on the CC sheet, using eq. (3). The FA, and TN reconstructions are shown on a flattened manifold sheet with the mapping  $\mathbb{R}^3 \rightarrow \mathbb{R}^2$  achieved through Maximal Variance Unfolding [13]. They reveal that controls have a higher FA/lower TN compared to the MS population who experience the reverse relationship since they are on the negative  $b_1$  axis (results not shown). The 10 percent most important samples assessed by the linear discriminant score, are shown in Fig. 2(d)-(e) on the manifold(d) and a flattened representation(e). Several regions appear important in distinguishing the two groups but the most coherent region appears in the Splenium.

## 5. DISCUSSION

We have demonstrated a method for doing tract-oriented group-wise inferences on tracts with sheet-like topology. Results show increased FA and lower TN in the controls when compared to an MS population, confirming previous studies [6]. Testing for RR and SP phenotype differences did not find a significant difference.

Future MS studies may investigate if specific components contain discriminative power within the population as to yield disease markers or attempt to answer which diffusion modalities and in which tracts they best explain the disease course.

## 6. REFERENCES

- [1] P. J. Basser and C. Pierpaoli, "Microstructural and physiological features of tissues elucidated by quantitative-diffusion-tensor mri.," *J.M.R.*, vol. 111, no. 3, pp. 209–219, Jun 1996.
- [2] S. H. Eriksson, F. J. Rugg-Gunn, M. R. Symms, G. J. Barker, and J. S. Duncan, "Diffusion tensor imaging in patients with epilepsy and malformations of cortical development.," *Brain*, vol. 124, no. Pt 3, pp. 617–626, Mar 2001.
- [3] S. M. Smith, M. Jenkinson, H. Johansen-Berg, D. Rueckert, T. E. Nichols, C. E. Mackay, K. E. Watkins, O. Ciccarelli, M. Z. Cader, P. M. Matthews, and T. E. J. Behrens, "Tract-based spatial statistics: voxelwise analysis of multi-subject diffusion data.," *Neuroimage*, vol. 31, no. 4, pp. 1487–1505, Jul 2006.
- [4] C. B. Goodlett, P. T. Fletcher, J. H. Gilmore, and G. Gerig, "Group analysis of dti fiber tract statistics with application to neurodevelopment.," *Neuroimage*, vol. 45, no. 1 Suppl, pp. S133–S142, Mar 2009.
- [5] P. A. Yushkevich, H. Zhang, T. J. Simon, and J. C. Gee, "Structure-specific statistical mapping of white matter tracts.," *Neuroimage*, vol. 41, no. 2, pp. 448–461, Jun 2008.
- [6] O. Ciccarelli, D. J. Werring, C. A. Wheeler-Kingshott, G. J. Barker, G. J. Parker, A. J. Thompson, and D. H. Miller, "Investigation of ms normal-appearing brain using diffusion tensor mri with clinical correlations.," *Neurology*, vol. 56, no. 7, pp. 926–933, Apr 2001.
- [7] H. Zhang, P. A. Yushkevich, and J. C. Gee, "Deformable registration of diffusion tensor mr images with explicit orientation optimization.," *Med Image Comput Comput Assist Interv*, vol. 8, no. Pt 1, pp. 172–179, 2005.
- [8] H. Zhang, B. B. Avants, P. A. Yushkevich, J. H. Woo, S. Wang, L. F. McCluskey, L. B. Elman, E. R. Melhem, and J. C. Gee, "High-dimensional spatial normalization of diffusion tensor images improves the detection of white matter differences: an example study using amyotrophic lateral sclerosis.," *IEEE Trans Med Imaging*, vol. 26, no. 11, pp. 1585–1597, Nov 2007.
- [9] M. Lazar, D. M. Weinstein, J. S. Tsuruda, K. M. Hasan, K. Arfanakis, M. E. Meyerand, B. Badie, H. A. Rowley, V. Haughton, A. Field, and A. L. Alexander, "White matter tractography using diffusion tensor deflection.," *Hum Brain Mapp*, vol. 18, no. 4, pp. 306–321, Apr 2003.
- [10] S. Mori and P. C. M. van Zijl, "Fiber tracking: principles and strategies - a technical review.," *NMR Biomed*, vol. 15, no. 7-8, pp. 468–480, 2002.
- [11] I. T. Jolliffe, "Principal component analysis, 2," April 2002.
- [12] W. J. Welch, "Construction of permutation tests," *Journal of the American Statistical Association*, vol. 85, no. 411, pp. 693–698, 1990.
- [13] K. Q. Weinberger and L. K. Saul, "An introduction to nonlinear dimensionality reduction by maximum variance unfolding," in *AAAI'06: proceedings of the 21st national conference on Artificial intelligence*, 2006, pp. 1683–1686.

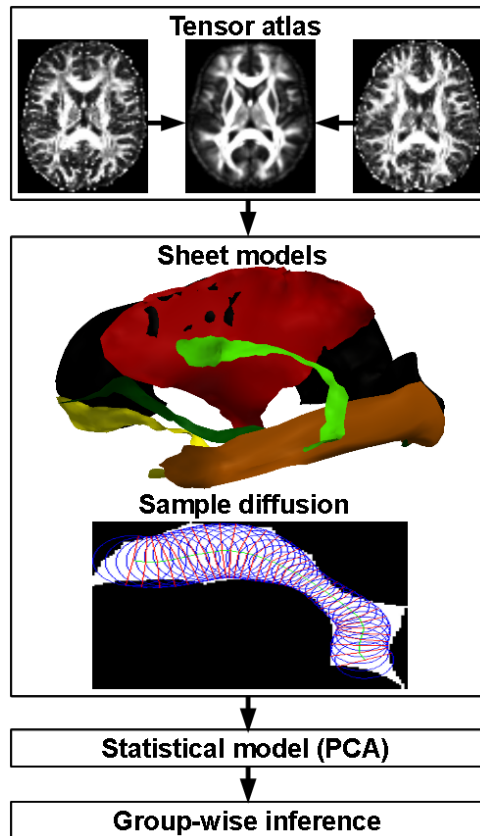


**Fig. 1:** Illustrates the method pipeline of the analysis consisting of; 1) building a tensor atlas and 2) modelling the WM tracts of the corpus callosum in black, the inferior longitudinal fasciculus in brown, the uncinate fasciculus in yellow, the superior longitudinal fasciculus in light green, the corticospinal fasciculus in red and the inferior fronto-occipital fasciculus in dark green. 3) Forming a statistical model from sampling diffusion within the model interior, shown for a 2D example with the medial curve in green, sampling spokes in red and the surface of the model in blue and 4) drawing conclusion with respect to group differences

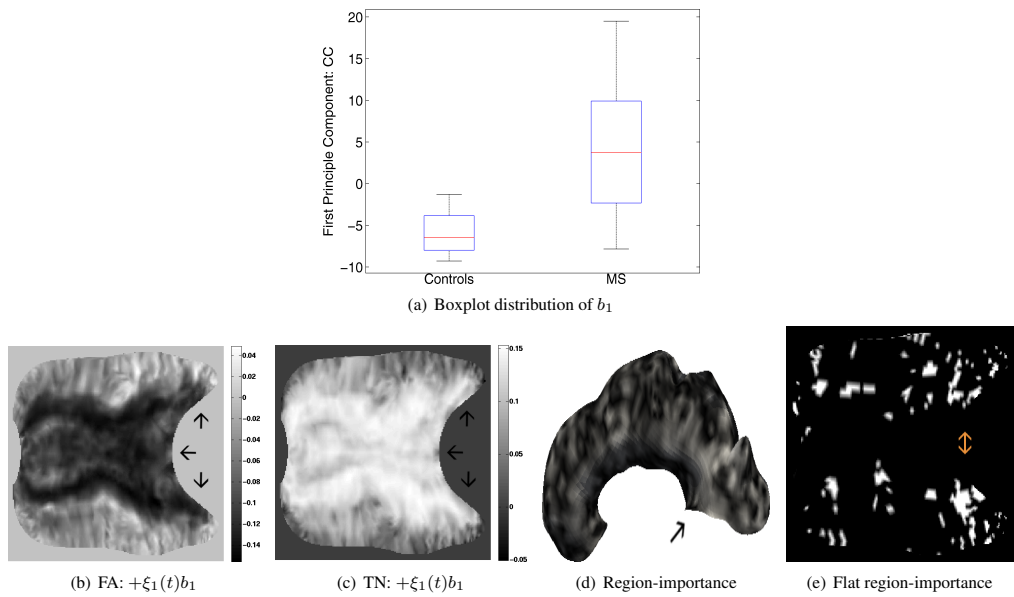


**Fig. 2:** A comparison of controls and MS for the CC. (a) Boxplot distribution of the MS and control subjects projections in PCA space, using the first component. MS subjects lie on the positive and controls on the negative axis. (b)-(c) Varies the first component in the positive directions and reconstruct the impact on FA and TN. Results are displayed on a flattened sheet manifold with splenium indicated by arrows. (d) Shows the region importance on the CC manifold while (e) is a flat representation of the importance but using only the 10 percent most important sampling regions as measured by FA



## CHAPTER 10

# **Secondary progressive and relapsing remitting multiple sclerosis leads to widespread decreased anatomical connectivity**

---

In submission, NeuroImage, March, 2013.

# **Secondary progressive and relapsing remitting multiple sclerosis leads to widespread decreased anatomical connectivity**

Mark Lyksborg<sup>1,2</sup>, Hartwig R. Siebner<sup>1</sup>, Per S. Sørensen<sup>3</sup>, Morten Blinkenberg<sup>3</sup>, Geoff JM. Parker<sup>4</sup>,

Anne-Marie Dogonowski<sup>1</sup>, Ellen Garde<sup>1</sup>, Rasmus Larsen<sup>2</sup>, Tim B. Dyrby<sup>1</sup>

1. Danish Research Centre for Magnetic Resonance, Copenhagen University Hospital Hvidovre, Denmark

2. Department of Applied Mathematics and Computer Science, DTU Compute, Technical University of Denmark, Kongens Lyngby, Denmark

3. Danish Multiple Sclerosis Center, Copenhagen University Hospital Rigshospitalet, Denmark

4. Centre for Imaging Sciences, Biomedical Imaging Institute, University Of Manchester, United Kingdom & Bioxydyn Limited, Manchester, United Kingdom

**Corresponding author: Mark Lyksborg**

**E-mail:** [markl@drcmr.dk](mailto:markl@drcmr.dk) and [mlyk@imm.dtu.dk](mailto:mlyk@imm.dtu.dk)

**Address:**

Danish Research Centre for Magnetic Resonance,  
Copenhagen University Hospital Hvidovre, section 714,  
Kettegaard Alle 30, 2650 Hvidovre, Denmark

## Abstract

Multiple sclerosis (MS) damages central white matter pathways which has considerable impact on disease-related disability. To identify disease-related alterations in anatomical connectivity, 34 patients (19 with relapsing remitting MS (RR-MS), 15 with secondary progressive MS (SP-MS) and 20 healthy subjects underwent diffusion magnetic resonance imaging (dMRI) of the brain. Based on the dMRI, anatomical connectivity mappings (ACM)s were estimated, as the values of an ACM quantify the connectedness shared by each voxel with all other brain voxels. To avoid biases caused by inter-individual brain-shape differences, they were estimated in a spatially normalized space. The ACM results of voxel-based analyses were compared with similar analyses based on fractional anisotropy (FA), also obtained from dMRI. In both RR-MS and SP-MS patients, large portions of the cerebral white matter revealed decreases in ACM and FA when compared with healthy controls. Patients with SP-MS exhibited reduced ACM values relative to RR-MS in the motor projection tracts, specifically in the corona radiata, whereas there were no consistent decreases in FA between SP-MS and RR-MS patients. Regional ACM statistics exhibited moderate correlation with clinical disability as assessed by the expanded disability status scale (EDSS). The correlation between these statistics and disability was either similar to or stronger than the correlation found between FA statistics and the EDSS scale. Together, the results highlight the potential of ACM to identify alterations of the anatomical connectivity in MS as well as the potential of ACM to study the relationship between these alterations, the clinical phenotype, and impairment.

**Keywords:** multiple sclerosis, phenotype, probabilistic tractography, anatomical connectivity mapping, clinical disability, diffusion magnetic resonance imaging

# 1. Introduction

Multiple sclerosis (MS) is an auto-immune disease that diffusely affects the structural and functional integrity of white matter (WM) tracts, contributing to disease-related disability. Regional structural abnormalities can be readily detected with magnetic resonance imaging (MRI) which explains the pivotal role of conventional MRI techniques for early diagnosis of MS (Rocca et al., 2012). However, the WM lesions as demonstrated by T2-weighted MRI only show a weak correlation with disease-related disability (Filippi et al., 1994; Filippi and Rocca, 2007). The poor relation between clinical disability and lesion loads as revealed by T2-weighted MRI has motivated the search for other MRI markers which may reflect more closely the disease-related structural changes leading to disability.

Diffusion magnetic resonance imaging (dMRI) is an imaging modality sensitive to the mobility of water molecules. It is sensitive to disease-induced changes in microstructure because the regional diffusion process of water is determined by the microstructural boundaries of the brain tissue. To characterize the regional diffusion properties and to estimate the most probable axonal fiber direction of a voxel region, diffusion tensor imaging (DTI) can be used (Basser, 1995). The DTI model enables the estimation of simple scalar diffusion indices such as the mean diffusivity (MD), fractional anisotropy (FA) (Basser and Pierpaoli, 1996) and many others, which have been successfully applied to study microstructural abnormalities in patients with MS, showing reduced FA (increased MD) in both MS lesions and normal appearing white matter (NAWM) (Werring et al., 1999; Ciccarelli et al., 2001; Gallo et al., 2005), presumably reflecting axonal damage (Ciccarelli et al., 2003). Further, regional changes in the diffusion indices have been linked to disease-related disability (Ozturk et al., 2010) and to specific clinical phenotypes (Preziosa et al., 2011).

While DTI-derived indices are assumed to reflect local microstructural properties, other measures such as anatomical connectivity mapping (ACM) assess to which degree a voxel is connected with the rest of the brain. ACM provides a voxel-specific measure of whole-brain anatomical connectivity by initiating probabilistic streamlines from all voxels within a whole-brain mask and counting the number of streamlines passing through each voxel within the mask, as was first proposed by (Embleton et al., 2007). ACM has recently been applied to identify regions showing reduced whole-brain anatomical connectivity in patients with Alzheimer's disease (Bozzali et al., 2011) and in patients with a relapsing remitting (RR) course of MS (Bozzali et al., 2013). The latter study revealed reduced anatomical connectivity in the thalamus and caudate nucleus but not in the cerebral WM of the MS group relative to a healthy control group. In addition, regional ACM values in the corpus callosum, right hippocampus and cerebellum showed a positive linear relationship with individual scores of the Paced-Auditory-Serial-Addition-Test (PASAT) (Rao et al., 1989), suggesting that the anatomical connectedness of these regions might be particularly relevant to measuring cognitive function in MS.

Here we apply ACM to study the disruption of anatomical connectivity in relapsing remitting MS (RR-MS) and secondary progressive MS (SP-MS). We minimized the influence of inter-subject anatomical differences by estimating ACM in a common stereotactic space. Given the diffuse pathology of MS, we hypothesized ACM to reveal widespread reductions in the cerebral WM compared with healthy controls and that these reductions will differ depending on the clinical form of MS. We further hypothesized an ACM reduction in motor-related tracts. The reduction should be

apparent when comparing patients to healthy controls and when comparing RR-MS patients to SP-MS patients. The basis of the ladder hypothesis is that the SP-MS patients in our study exhibit an increased motor disability compared to RR-MS patients, as measured by a higher extended disability status scale (EDSS) score (Kurtzke, 1983) where the EDSS score is known to be highly influenced by motor disability.

## **2. Materials and Methods**

### **2.1 Subjects**

Thirty-four patients suffering from MS fulfilling the revised McDonald criteria (Polman et al., 2005) participated in this study (Table 1) of whom 19 patients had been diagnosed with the RR-MS disease course, while 15 patients had been diagnosed with the SP-MS disease course. Patients were recruited from The Danish Multiple Sclerosis Center (at Rigshospitalet, Copenhagen, Denmark) and only clinically stable patients who had not experienced a relapse in the three months preceding the MRI measurement were included in the study. MS patients with neurological co-morbidity and with signs of depression or other psychiatric disorders were excluded from the study. All patients were neurologically examined and clinical disability was rated using the EDSS score (Kurtzke, 1983). The patients were treated with disease-modifying drugs (Interferon-beta, glatiramer acetate, natalizumab). Twenty healthy subjects without a history of neurological or psychiatric disease were included as control subjects. The study was approved by the Scientific Ethical Committee of the municipalities of Copenhagen and Frederiksberg (protocol no. KF01 – 131/03 with addendum) and all subjects gave written informed consent.

### **2.2. Magnetic resonance imaging**

All MRI data were acquired on a Siemens TRIO 3 tesla scanner using an eight-channel surface head-coil (In vivo, FL, USA). The structural MRI protocol included a three-dimensional T1-weighted image using a magnetization prepared rapid gradient echo (MPRAGE) sequence with a repetition time (TR) of 11400 ms, echo time (TE) of 2.32 ms, flip angle (FLA) of  $9^\circ$  and a matrix of  $182 \times 218 \times 182$ , resulting in a  $1 \text{ mm}^3$  isotropic resolution. Also acquired was a three-dimensional T2-weighted image (T2) with a TR of 3000 ms, TE of 354 ms, FLA= $180^\circ$  and a matrix of  $196 \times 256 \times 192$ , resulting in a  $1.1 \text{ mm}^3$  isotropic resolution and a three-dimensional T2-weighted fluid attenuation inversion recovery (FLAIR) image using the sequence parameters, TR=6000 ms, TE=353 ms, FLA= $180^\circ$  and a matrix of  $220 \times 256 \times 192$  ( $1.1 \text{ mm}^3$  resolution).

Diffusion MRI (dMRI) was acquired using a twice-refocused spin echo sequence (Reese et al., 2003) (TR=8200 ms, TE =100 ms, in-plane matrix =  $96 \times 96$ ; 61 slices) resulting in  $2.3 \text{ mm}^3$  isotropic voxel resolution. For each subject, ten non-diffusion weighted images (b0) and 61 diffusion weighted images (DWIs) were acquired using a b-factor of  $1200 \text{ s/mm}^2$ . In addition, a field map was obtained used a double gradient echo sequence (TR=479 ms, TE<sub>short</sub>=5.19 ms, TE<sub>long</sub>=7.65 ms, FLA= $60^\circ$ , matrix= $128 \times 128$ ; 47 slices) resulting in a voxel resolution of  $2 \times 2 \times 3 \text{ mm}^3$ .

## 2.3. Preprocessing

The DWIs were simultaneously corrected for eddy currents and motion by co-registering them with the first of the ten b0 images using a 12 parameter affine transformation (Collignon et al., 1995). To correct for susceptibility artefacts, a voxel displacement map was estimated based on the individual field maps and the field map correction approach, available through SPM8 (<http://www.fil.ion.ucl.ac.uk/spm/>) (Jezzard and Balaban, 1995). The voxel displacement map and the affine model displacements were combined and the DWIs re-sliced into the space of the first b0 image using tri-cubic interpolation. After re-slicing the DWIs, the gradient directions of the DWIs were updated by applying the rotational part of the affine model to the gradient directions (Alexander et al., 2001).

Based on T2, FLAIR and MPRAGE modalities WM lesions were segmented using an automated segmentation method described by (Dyrby et al., 2008). A radiographer manually adjusted the segmented lesions, resulting in a binary lesion mask for each MS subject. The FLAIR image was co-registered with the first b0 image of the dMRI and both the FLAIR and the lesion mask re-sliced into the space of the b0 image, using tri-cubic and nearest-neighbour interpolation for the respective images.

## 2.4 Anatomical Connectivity Mapping (ACM)

### 2.4.1 Fiber reconstruction: The multi-tensor

The multi-tensor model by (Tuch et al., 2002) was chosen as the multi-fiber model and the parameters of the model were fitted using a Levenberg-Marquardt optimization available through the Camino software (<http://cmic.cs.ucl.ac.uk/camino/>) (Cook et al., 2006). The maximum number of tensors was fixed to two per voxel, as the findings reported in (Tuch et al., 2002) suggest this to be the maximum number of resolvable fibers using b-factor near  $1000 \text{ s/mm}^2$ . To determine the number of fibers in a voxel, we used the classification approach proposed by (Alexander et al., 2002), also from Camino.

### 2.4.2 Spatial normalization of the multi-tensors

To ensure ACMs with cross-subject comparability, it is important to prevent cross-subject brain shape variability from biasing the connectivity values of the ACM. To avoid this, the tensor models were spatially normalized into a common space (Alexander et al., 2001; Cercignani et al., 2012) prior to calculating the ACM, as opposed to calculating the ACM in native space and then normalizing the ACM, as was done in previous cross-subject ACM studies (Bozzali et al., 2011; Bozzali et al., 2013). The optimal spatial normalization was found by matching the FA map of each subject with the FMRIB58\_FA atlas (58 healthy subjects) (Smith et al., 2004), using the FSL image registration routines flirt and fnirt (<http://www.fmrib.ox.ac.uk/fsl/>) (Jenkinson and Smith, 2001). To prevent severe MS pathology from influencing the spatial normalization, the option of cost function masking was enabled, using lesion masks to ensure that the spatial normalization is derived solely from tissue outside of lesions. The result of the spatial normalization was used to transform both the FA images and the multi-tensors of the subjects. To ensure proper orientation of the tensors after spatial normalization, the preservation of principal direction (PPD) algorithm (Alexander et al., 2001) was

used to re-orient each single tensor of the multi-tensor. The FA and multi-tensor volumes were re-sliced to 2 mm<sup>3</sup> isotropic resolutions matching the FMRIB58\_FA Atlas.

#### 2.4.3 Probabilistic whole-brain tractography

The values of an ACM reflect the connectivity/dis-connectivity that each individual voxel has with the rest of the brain and are estimated using probabilistic tractography (Parker and Alexander, 2003). The ACM is estimated by repeating probabilistic tractography for every seed voxel of the brain and counting the number of streamlines passing through each individual voxel. Besides the probabilistic tractography method, the ACM estimation also requires the specification of a brain mask specifying the seed voxels.

The binary brain mask of seed voxels was derived from the FMRIB58\_FA atlas where  $FA \leq 0$  voxels are identified as background. This whole-brain mask is used both as a seed mask and as a streamline stopping criteria. We used the probabilistic tractography method by (Parker and Alexander, 2003) and available in Camino (Cook et al, 2006), to propagate streamlines where the fiber orientation distribution function (fODF) of each voxel was simulated using the Bingham distribution at a signal-to-noise ratio (SNR) of 16. Probabilistic tracking is performed using, an interpolated tracking approach with a tracking step size of 1/10 the voxel size and using two streamline stopping criteria; the brain mask and if a streamline turns more than 180 degrees over the extent of a voxel, the latter criteria preventing a streamline from doubling back on itself.

#### 2.4.4 Number of streamlines

To minimize the uncertainty associated with voxel-wise connectivity estimates of an ACM it is important to choose a sufficiently large number of streamlines. We therefore estimated the average uncertainty of an ACM voxel as a function of the number of streamlines in five healthy subjects. Individual subject ACMs were estimated five times for a fixed number of streamlines (i.e., 10, 50, 100, 150, 300, 500, 700 streamlines per seed voxels) and the voxel-wise coefficient of variation (CV) was calculated (Dobson, 2002). For a given number of streamlines, the average CV across all voxels within the seed mask reflects the estimation uncertainty (the precision of an ACM estimate). By increasing the number streamlines while repeatedly estimating the average CV, we obtained the CV uncertainty measure as a function of streamlines. The average CV function is inversely proportional to the average SNR, and for the sake of completeness we supply both.

### 2.5 Group-wise statistical analysis

#### 2.5.1 Between-group comparison

Two voxel-based, group-wise hypotheses were tested. The first hypothesis was that ACM reveals decreased connectivity of the cerebral WM (FMRIB58\_FA > 0.25), in a group of RR-MS and a group of SP-MS patients who are compared with a group of healthy subjects. The second hypothesis was that SP-MS patients (high range EDSS) have decreased connectivity relative to RR-MS patients (low range EDSS).

The hypotheses were investigated by fitting a general linear model (GLM), including group, age, gender and atrophy as independent covariates and the ACM values as the dependent variable. Prior to fitting voxel-wise GLMs, the ACM data were smoothed using a Gaussian kernel with a full-width half-maximum value of 4 mm. After fitting the GLMs, the GLM parameters were examined using one-tailed two sample t-tests with the assumption of unequal variance, testing for voxel-wise significant differences between the group parameters of the GLM.

The same voxel-based, group-wise analyses were repeated using the DTI-derived indices of FA. The additional FA-based analyses enabled us to compare the outcome of analyses based on a measure reflecting the microstructural tissue properties (FA) with analyses based on whole-brain connectivity (ACM).

To estimate the atrophy covariate of each subject, a WM mask (FMRIB58\_FA>0.25) containing unit values was modulated with the determinant of the Jacobian of the deformation field used to spatially normalize from subject to atlas space. The determinant reflects the amount of expansion/contraction experienced by a voxel and is thus proportional to atrophy. This estimation approach corresponds to the voxel-based morphometry (VBM) approach described in (Ashburner and Friston, 2000; Good et al., 2001). To remove the influence that overall brain size may have on the determinant of the Jacobian, it was scaled using the intra cranial volume (ICV) calculated as the sum of WM, grey matter (GM) and cerebrospinal fluid (CSF) segmentations, estimated using the SIENAX (Smith et al., 2002b) segmentation routine of FSL 4.0.

To account for the problem of multiple comparisons (Logan et al., 2008; Miller, 1977), we adopted a small volume correction (SVC) approach (Worsley et al., 1996). The bilateral motor projection tracts, projecting from the pontine crossing tract region towards the motor cortex and the bilateral association tract of the superior longitudinal fasciculus were defined as WM regions of interest (ROI) for this purpose. We reasoned that these WM tracts would be particularly sensitive to disease-related reductions in the ACM of patients with MS. To specify the voxels corresponding to these ROIs, we used the expert delineations of the JHU-ICBM-DTI-81 atlas (S Mori and Nagae-Poetscher, 2005) which are in correspondence with the FMRIB58\_FA space. The bilateral motor projection tracts were assumed to coincide with the subset of atlas delineations, consisting of the pontine crossing tract, the internal capsule, the cerebral peduncle, the corticospinal tract, and the corona radiata. The bilateral superior longitudinal fasciculi were given by the corresponding atlas delineation. Within these ROIs, the SVC method of SPM8 was used to correct for multiple non-independent comparisons, yielding a family wise error (FWE) corrected p-value. The threshold for achieving statistical significance was set to 0.05.

### 2.5.2 Within-group correlation analyses

For these analyses, we expected that regional reduced anatomical connectivity in the motor projection tracts might be closely related to inter-individual variations in clinical disability. The analyses were conducted by estimating a regional median ACM statistic within the aforementioned WM ROIs of the atlas, which were correlated with the EDSS scores using Pearson's correlation coefficient. For the sake of comparison, the linear correlation was also calculated for the median FA of the ROIs. These analyses were supplemented by GLM analyses using models adjusted for confounding covariates. We

fit the GLM using EDSS as the outcome measure, and using the median statistic, age and gender as explanatory covariates. The fitting correlation of the GLM and its coefficient of determination  $r^2$  (Dobson, 2002) were used as supplementary indicators of the disease-related information inferred from the ACM and FA respectively.

White matter lesion load is often used as an imaging marker in MS treatment studies (Filippi et al., 2011). For comparison we therefore estimated the individual lesion loads normalized to the skull size using the SIENAX routine of FSL 4.0 (Smith, 2002a) and correlated inter-individual variations in lesion load with inter-individual variations in the EDSS score.

### **3. Results**

#### **3.1 Number of streamlines**

ACM estimation using probabilistic tractography with different numbers of streamlines per voxel revealed a decreasing SNR benefit as the number of streamlines increases (Table 2). SNR became stable in the range 300 to 700 streamlines, prompting us to choose 500 streamlines per seed voxel to yield asymptotically stable ACM estimates. Depending on the desired average SNR, an acceptable ACM may be estimated with fewer streamlines.

#### **3.2 Reduced connectivity in patients**

Patients with RR-MS and SP-MS showed widespread voxel-based ACM reductions in cerebral WM compared to healthy subjects (Figs. 1(a) and 1(c)) and applying SVC in the ROIs of the pre-defined bilateral WM tracts of interest (the motor projection tracts and the superior longitudinal fascicle) resulted in widespread FWE-corrected and significant voxels in all ROIs (FWE results not shown). This widespread reduction in anatomical connectivity was also reflected by a significantly lower median ACM statistic estimated within the cerebral WM of the RR-MS and SP-MS groups, compared with healthy control subjects ( $p$ -value $<0.0001$ , one-tailed two-sample  $t$ -test; Fig. 2(a)). While both patient groups displayed voxel-wise decreased ACM values in the cerebral WM, there were overall more voxels showing an ACM reduction in patients with SP-MS relative to patients suffering from RR-MS (Fig. 1 (a) and 1(c)).

Patients with RR-MS and SP-MS also demonstrated widespread decreases in FA (Figs. 1(b) and 1(d)), resulting in significant FWE-corrected voxels in the pre-defined ROIs (FWE results not shown). Accordingly, the median FA statistics of the cerebral WM were significantly reduced in patients with RR-MS and SP-MS ( $p$ -value $<0.0001$ , two-sample  $t$ -test; Fig. 2(b)). In summary, the results show that both RR-MS and SP-MS are associated with widespread decreases in ACM and FA and further suggest that when using global summary statistics, FA and ACM appear equally informative about the clinical phenotypes.

#### **3.3 Decreased connectivity of SP-MS relative to RR-MS**

When investigating the hypothesis of decreased anatomical connectivity of the SP-MS patients compared to RR-MS patients, we found the median ACM statistics across the cerebral WM to be

decreased in patients with SP-MS relative to patients with RR-MS ( $p = 0.027$ , two-sample t-test; Fig. 2(a)). Median FA statistics were not significantly different between the two groups ( $p = 0.126$ , two-sample t-test; Fig. 2(b)). Voxel-based analysis revealed localized decreases of the ACM values in patients with SP-MS relative to RR-MS (Fig. 3(a)). Within the aforementioned bilateral WM tracts of interest, we identified a large number of voxels where ACM values were significantly reduced in SP-MS patients relative to patients with RR-MS (Fig. 3(a); Table 3). Table 3 lists the location of these spatially coherent significant voxels. According to the JHU-ICBM-DTI-81 atlas, a large number of voxels able to survive the SVC analysis were located in the left and right posterior corona radiata, the pontine crossing tract, the internal capsule and the corticospinal tract as well as the right superior longitudinal fasciculus. In contrast, the same voxel-based group comparison based on FA, revealed no FWE-corrected significant differences between SP-MS and RR-MS and thus this is not reported in Table 3. For comparison, the uncorrected voxel-based t-test analyses based on FA are depicted in Fig. 3(b), underlining the difference in results between ACM and FA based analyses.

In addition to the pre-defined WM tract ROIs, Fig. 3(a) also reveals regions of decreased ACM in the splenium and genu of the corpus callosum. In addition to being near GM/WM boundaries which might indicate partial volume contamination, these differences did not survive whole-brain correction for multiple comparisons and may therefore be perceived as statistical trends.

### 3.4 Correlations between ACM and clinical disability

The region-specific median ACM statistics of the bilateral WM tracts of interest showed significant correlations with the individual EDSS scores, displayed in Table 4, containing analysis results of the previously identified WM regions (Table 3). Correlation based on the corresponding FA statistics generally did not result in the same significance (Table 4). Using a GLM adjusted for age and gender effects instead, significant EDSS correlations were found both for ACM and FA (Table 4). Based on the adjusted GLM, the magnitude of correlations between the ACM statistics and EDSS scores, as well as the amount of variance explained by the GLM, were generally higher than using FA statistics. Especially the median ACM statistics of right posterior corona radiata, right superior longitudinal fasciculus and the pontine crossing tract showed a stronger correlation with the EDSS scores than the corresponding median FA statistics (Fig. 4).

Pearson's linear correlation coefficient between skull-normalized lesion load and the EDSS was 0.316 ( $p\text{-value} < 0.05$ ), while the GLM adjusted for age and gender had fitting correlation 0.59 ( $p\text{-value} < 0.01$ ) and the coefficient of determination value  $r^2 = 0.354$ , equivalent to the mid-range statistical performance listed in Table 4.

## 4. Discussion

Based on the technique of ACM, we found widely reduced anatomical connectivity in the cerebral WM of patients with RR-MS and SP-MS compared to healthy subjects. SP-MS patients showed voxel-wise reduced ACM values relative to RR-MS in the motor projection tracts, while no consistent decreases were found based on FA. Finally, regional ACM statistics correlated moderately with clinical disability as reflected by the EDSS score.

#### **4.1. Reduced connectivity in patients**

Voxel-based and ROI-based analyses provided converging evidence for a reduction in the ACM values of MS patients, compared to a group of healthy subjects. The voxel-wise reductions of ACMs were found in large parts of the cerebral WM, showing that MS diffusely affects the structural connectivity of the brain as reflected by ACM.

Previously, ACM has been investigated in patients with RR-MS (Bozzali et al., 2013). In that study, ACM changes were found in the subcortical GM nuclei but not in WM. We showed that MS is also associated with a widespread change of anatomical connectivity in WM. Critically, the ACM values of cerebral WM were substantially decreased, not only in more severely affected patients with SP-MS, but also in patients with the RR-MS disease course, who were generally less impaired than patients with SP-MS.

Several pathological processes may have contributed to reducing the ACM in patients with MS. Axonal damage, Wallerian degeneration, local inflammation and demyelination, all contribute to changing the ACM values, since these pathologies are believed to alter the diffusion process, leading to changes in the principal directional uncertainty of the fODF. The decreased ACM values of MS patients widely summarizes these pathological processes, since a connectivity value of an ACM voxel obtains its value based on streamlines that may have passed through areas of the WM tract with different underlying pathology. As a consequence ACM values do not reflect any tissue-specific pathology process, but rather reflect the accumulated effects of pathologies present along a WM tract.

In addition to voxel-wise ACM reductions, MS patients also exhibited widespread decreases in FA, suggesting that both ACM and FA are sensitive to measuring MS-related changes, although they may not have the same interpretation. The decrease in FA, agrees with the findings of (Preziosa et al., 2011) reporting widely decreased FA within the major WM tracts of MS patients.

#### **4.2. Decreased connectivity of SP-MS relative to RR-MS**

Despite the widespread voxel-wise reductions in FA and ACM, suggesting similar discriminative power between healthy controls and MS, the information of FA and ACM values are quite different. A decrease of an ACM voxel generally reflects accumulated pathology of the whole brain, whereas an FA decrease is specific to a localized pathologic state. This difference explains why group-wise, voxel-based comparisons based on ACM resulted in significant differences between SP-MS and RR-MS patients, while we were unable to find differences using FA. Additionally, the median ACM statistic of the entire cerebral WM was significantly lower in patients with SP-MS than in patients with RR-MS. Together, these findings highlight the potential use of ACM to capture alterations in the connectivity pattern which are characteristic to the different clinical forms of MS.

The significant voxel-based ACM decreases were largely found within the bilateral motor projection tracts. The structural anatomy of these tracts is expected to considerably impact patients' EDSS score, a score which is known to be strongly related with motor impairment. The strongly localized ACM reductions in patients with SP-MS are plausible as the patient group with RR-MS had less motor

impairment as reflected by their EDSS scores. Additionally ACM decreases of SP-MS were found in the superior longitudinal fasciculus which could be motor-related but might also be related to differences in distinct cognitive functions between both groups. Since we did not expose patients to cognitive tests, we cannot comment on this possibility.

### **4.3. Correlation between ACM and clinical disability**

Region-specific median ACM statistics calculated within WM ROIs correlated with MS disability as indicated by the EDSS score which is a summary measure of disability in eight functional systems, but weighted towards ambulation (Kurtzke, 1983). Negative correlations were found between the median ACM statistics and individual EDSS scores of the MS group. In contrast to our results, the study by (Bozzali et al, 2013) found no voxel-based correlation between ACM and the EDSS scores in patients with RR-MS. We attribute these negative findings to the fact that they examined voxel-based correlations, the smaller range of inter-subject variation in EDSS scores and the smaller sample size in that study as compared with our study which covers a larger EDSS range. There are also methodological differences in the ACM estimation which could cause differences between the results.

Correlation analyses did not reveal any significant correlations between the median FA statistics and individual EDSS scores. However, when applying a GLM that adjusted for between-subject differences of age and gender, we found a linear relationship with clinical disability for both the median ACM and median FA. Using the GLM, the explanatory power of the linear relation was generally stronger for the median ACM statistics as opposed to the corresponding FA statistics. The median ACM in the right posterior corona radiata, right superior longitudinal fasciculus and the pontine crossing tract correlated more strongly with the EDSS scores than the corresponding median FA. Conversely, there was no WM tract ROI where the correlation was stronger for FA, a statement which is upheld also for the WM ROIs which have not been included in the table. Since ACM and FA provide complementary information, it is possible that a combined measure that integrates the structural information provided by FA and ACM might be most sensitive to disability and disease progression. Adding to the discussion, we should also note that the GLM based on lesion loads, was able to explain an amount of variance similar to the median ACM values in Table 4.

These findings suggest that ACM may be used to relate regional anatomic disconnection with disease-related disabilities. A similar finding was made in a study involving amyotrophic lateral sclerosis patients, in which a tract-specific probabilistic index of the cortico-pontine motor tract was found to achieve better disease score correlation than FA (Ciccarelli et al., 2006). Accordingly, (Bozzali et al., 2013) demonstrated that ACM values in the anterior body of the corpus callosum correlated with the number of correct responses in the Pace Auditory Serial Addition Test (PASAT) in patients with RR-MS. Together, these findings suggest that ACM has the potential to unravel interesting relations between altered anatomical connectivity and disease-related disabilities. In this context, the use of specific motor or cognitive tests, for instance measurements of ankle dorsiflexion and hip flexion strength (Reich et al., 2008), may be used to inform future ACM studies in patients with MS to find out how altered anatomical connectivity in specific tracts affect specific motor and cognitive functions.

#### **4.4. Methodological considerations**

When ACM is applied to patients with MS, probabilistic tractography needs to measure isotropic diffusion components in the affected brain tissue due to inflammation, demyelination, gliosis, and axonal injury. We combined the multi-tensor model with the Bingham distribution (Bingham, 1974), used with the probabilistic tracking method of (Parker and Alexander, 2003) in order to capture these effects. Additionally, we used a conservatively large number of streamlines per voxel (500 streamlines). Although previous studies have based ACM estimations on just 10 streamlines (Bozzali et al., 2011; Bozzali et al., 2013; Embleton et al., 2007), our SNR investigations suggested that such a low number of streamlines may lead to under sampling of the ACM connectivity distributions.

We introduced a spatially normalized ACM technique, suited for group studies to account for the integrated pathology occurring along WM tracts of MS patients. Our approach is conceptually similar to the atlas building approach of (Cercignani et al., 2012) and in contrast to previously published ACM studies by (Bozzali et al., 2011; Bozzali et al., 2013), it ensures that the connectivity estimates of ACM become minimally dependent on the individuals brain shape and size variation.

### **5. Conclusion**

We successfully applied a modified version of ACM, optimized for between-group comparisons to detect consistent differences in anatomical WM connectivity between two clinical sub-groups of MS. We were able to relate alterations in the ACM of WM with disease-related disability and showed that ACM provides complementary information to conventional DTI-based indices of microstructure such as FA. However further large scale studies are warranted to explore the potential of ACM to map the magnitude and spatial distribution of anatomical disconnection in brain diseases and relate these connectivity changes with disease-related disabilities.

### **6. Acknowledgements**

The project was supported by the Danish Council for Strategic Research (grant-nr. 2142-08-0039), the Danish Multiple Sclerosis Society (grant-nr. R266-A14682), and the Lundbeck Foundation (Grant of Excellence: Mapping, Modulation & Modelling the Control of Actions, grant-no. R59-A5399).



## Bibliography

- Alexander, D. C., Pierpaoli, C., Basser, P. J., and Gee, J. C., 2001. Spatial transformations of diffusion tensor magnetic resonance images. *IEEE Trans Med Imaging*. 20(11), 1131-1139.
- Alexander, D.C., Barker, G., and Arridge, S., 2002. Detection and modelling of non-gaussian apparent diffusion coefficient profiles in human brain data. *Magnetic Resonance in Medicine*. 48(2), 331-340.
- Ashburner, J. and Friston, K. J., 2000. Voxel-based morphometry—the methods. *Neuroimage*. 11(6), 805-821.
- Basser, P. J., 1995. Inferring microstructural features and the physiological state of tissues from diffusion-weighted images. *NMR Biomed*. 8(7-8), 333-344.
- Basser, P. J. and Pierpaoli, C., 1996. Microstructural and physiological features of tissues elucidated by quantitative-diffusion-tensor mri. *J Magn Reson B*. 111(3), 209-219.
- Bingham, C., 1974. An antipodally symmetric distribution on the sphere. *The Annals of Statistics*. 2(6), 1201-1225.
- Bozzali, M., Parker, G. J. M., Serra, L., Embleton, K., Gili, T., Perri, R., Caltagirone, C., and Cercignani, M., 2011. Anatomical connectivity mapping: a new tool to assess brain disconnection in alzheimer's disease. *Neuroimage*. 54(3), 2045-2051.
- Bozzali, M., Spanò, B., Parker, G., Giulietti, G., Castelli, M., Basile, B., Rossi, S., Serra, L., Magnani, G., Nocentini, U., Caltagirone, C., Centonze, D., and Cercignani, M., 2013. Anatomical brain connectivity can assess cognitive dysfunction in multiple sclerosis. *Mult Scler*. Epublished.
- Cercignani, M., Embleton, K., Parker, G. J. M., and Bozzali, M., 2012. Group-averaged anatomical connectivity mapping for improved human white matter pathway visualisation. *NMR Biomed*. 25(11), 1224-1233.
- Ciccarelli, O., Werring, D. J., Wheeler-Kingshott, C. A., Barker, G. J., Parker, G. J., Thompson, A. J., and Miller, D. H., 2001. Investigation of ms normal-appearing brain using diffusion tensor mri with clinical correlations. *Neurology*. 56(7), 926-933.
- Ciccarelli, O., Werring, D. J., Barker, G. J., Griffin, C. M., Wheeler-Kingshott, C. A. M., Miller, D. H., and Thompson, A. J., 2003. A study of the mechanisms of normal-appearing white matter damage in multiple sclerosis using diffusion tensor imaging—evidence of wallerian degeneration. *J Neurol*. 250(3), 287-292.
- Ciccarelli, O., Behrens, T. E., Altmann, D. R., Orrell, R. W., Howard, R. S., Johansen-Berg, H., Miller, D. H., Matthews, P. M., and Thompson, A. J., 2006. Probabilistic diffusion tractography: a potential tool to assess the rate of disease progression in amyotrophic lateral sclerosis. *Brain*, 129(7), 1859-1871.
- Collignon, A., Maes, F., Delaere, D., Vandermeulen, D., Suetens, P., and Marchal, G., 1995. *Automated multi-modality image registration based on information theory*. *Information Processing in Medical Imaging*. 3(6), 263-274.
- Cook, P. A., Bai, Y., Nedjati-Gilani, S., Seunarine, K. K., Hall, M. G., Parker, G. J., and Alexander, D. C., 2006. Camino: Open-source diffusion-mri reconstruction and processing. In *Proc. Intl. Soc. Mag. Reson. Med*. 14.
- Dobson, A. J., 2002. *An Introduction to Generalized Linear Models*. Chapman & Hall/CRC.

Dyrby, T. B., Rostrup, E., Baaré, W. F. C., van Straaten, E. C. W., Barkhof, F., Vrenken, H., Ropele, S., Schmidt, R., Erkinjuntti, T., Wahlund, L.-O., Pantoni, L., Inzitari, D., Paulson, O. B., Hansen, L. K., Waldemar, G., and , L. A. D. I. S. s. g., 2008. Segmentation of age-related white matter changes in a clinical multi-center study. *Neuroimage*, 41(2), 335-345.

Embleton, K. V., Morris, D. M., Haroon, H. A., Ralph, M. A. L., and Parker, G. J., 2007. Anatomical connectivity mapping. In *Proc. Intl. Soc. Mag. Reson. Med.* 15.

Filippi, M., Horsfield, M. A., Morrissey, S. P., MacManus, D. G., Rudge, P., McDonald, W. I., and Miller, D. H., 1994. Quantitative brain mri lesion load predicts the course of clinically isolated syndromes suggestive of multiple sclerosis. *Neurology*. 44(4), 635-641.

Filippi, M. and Rocca, M. A., 2007. Conventional mri in multiple sclerosis. *J Neuroimaging*. 17 Suppl 1, 3S-9S.

Filippi, M., Rocca, M. A., De Stefano, N., Enzinger, C., Fisher, E., Horsfield, M. A., Inglese, M., Pelletier, D., and Comi, G., 2011. Magnetic resonance techniques in multiple sclerosis: the present and the future. *Arch Neurol*. 68(12), 1514-1520.

Gallo, A., Rovaris, M., Riva, R., Ghezzi, A., Benedetti, B., Martinelli, V., Falini, A., Comi, G., and Filippi, M., 2005. Diffusion-tensor magnetic resonance imaging detects normal-appearing white matter damage unrelated to short-term disease activity in patients at the earliest clinical stage of multiple sclerosis. *Arch Neurol*. 62(5), 803-808.

Good, C. D., Johnsrude, I. S., Ashburner, J., Henson, R. N., Friston, K. J., and Frackowiak, R. S., 2001. A Voxel-Based morphometric study of ageing in 465 normal adult human brains. *NeuroImage*. 14(1), 21-36.

Jenkinson, M. and Smith, S., 2001. A global optimisation method for robust affine registration of brain images. *Medical Image Analysis*. 5(2), 466-475.

Jezzard, P. and Balaban, R. S., 1995. Correction for geometric distortion in echo planar images from b0 field variations. *Magn Reson Med*. 34(1), 65-73.

Kurtzke, J. F., 1983. Rating neurologic impairment in multiple sclerosis: an expanded disability status scale (edss). *Neurology*. 33(11), 1444-1452.

Logan, B. R., Geliazkova, M. P., and Rowe, D. B., 2008. An evaluation of spatial thresholding techniques in fmri analysis. *Hum Brain Mapp*. 29(12), 1379-1389.

Miller, Rupert G., J., 1977. Developments in multiple comparisons 1966-1976. *Journal of the American Statistical Association*. 72(360), 779-788.

Ozturk, A., Smith, S. A., Gordon-Lipkin, E. M., Harrison, D. M., Shiee, N., Pham, D. L., Caffo, B. S., Calabresi, P. A., and Reich, D. S., 2010. Mri of the corpus callosum in multiple sclerosis: association with disability. *Mult Scler*. 16(2), 166-177.

Parker, G. J. M. and Alexander, D. C., 2003. Probabilistic monte carlo based mapping of cerebral connections utilising whole-brain crossing fibre information. *Inf Process Med Imaging*. 18, 684-695.

Polman, C. H., Reingold, S. C., Edan, G., Filippi, M., Hartung, H.-P., Kappos, L., Lublin, F. D., Metz, L. M., McFarland, H. F., O'Connor, P. W., Sandberg-Wollheim, M., Thompson, A. J., Weinshenker, B. G., and Wolinsky, J. S., 2005. Diagnostic criteria for multiple sclerosis: 2005 revisions to the "mcdonald criteria". *Ann Neurol*. 58(6), 840-846.

Preziosa, P., Rocca, M. A., Mesaros, S., Pagani, E., Stosic-Opincal, T., Kacar, K., Absinta, M., Caputo, D., Drulovic, J., Comi, G., and Filippi, M., 2011. Intrinsic damage to the major white matter

tracts in patients with different clinical phenotypes of multiple sclerosis: a voxelwise diffusion-tensor mr study. *Radiology*. 260(2), 541-550.

Rao, S. M., Leo, G. J., Haughton, V. M., St Aubin-Faubert, P., and Bernardin, L., 1989. Correlation of magnetic resonance imaging with neuropsychological testing in multiple sclerosis. *Neurology*. 39(2), 161-166.

Reese, T. G., Heid, O., Weisskoff, R. M., and Wedeen, V. J., 2003. Reduction of eddy-current-induced distortion in diffusion mri using a twice-refocused spin echo. *Magn Reson Med*. 49(1), 177-182.

Reich, D. S., Zackowski, K. M., Gordon-Lipkin, E. M., Smith, S. A., Chodkowski, B. A., Cutter, G. R., and Calabresi, P. A., 2008. Corticospinal tract abnormalities are associated with weakness in multiple sclerosis. *AJNR Am J Neuroradiol*. 29(2), 333-339.

Rocca, M. A., Messina, R., and Filippi, M., 2012. Multiple sclerosis imaging: recent advances. *J Neurol*. 260(3), 929-935

S Mori, S Wakana, P. V. Z. and Nagae-Poetscher, L. (2005). *MRI Atlas of Human White Matter*. Elsevier.

Smith, S. M., 2002a. Fast robust automated brain extraction. *Hum Brain Mapp*. 17(3), 143-155.

Smith, S. M., Zhang, Y., Jenkinson, M., Chen, J., Matthews, P. M., Federico, A., and De Stefano, N., 2002b. Accurate, robust, and automated longitudinal and cross-sectional brain change analysis. *Neuroimage*. 17(1), 479-489.

Smith, S.M., Jenkinson, M., Woolrich, M., Beckmann, C., Behrens, T., Johansen-Berg, H., Bannister, P., Luca, M. D., Drobnjak, I., Flitney, D., Niazy, R., Saunders, J., Vickers, J., Zhang, Y., Stefano, N. D., Brady, J., and Matthews, P., 2004. Advances in functional and structural mr image analysis and implementation as fsl. *Neuroimage*. 23, 208-219.

Tuch, D. S., Reese, T. G., Wiegell, M. R., Makris, N., Belliveau, J. W., and Wedeen, V. J., 2002. High angular resolution diffusion imaging reveals intravoxel white matter fiber heterogeneity. *Magn Reson Med*. 48(4), 577-582.

Werring, D. J., Clark, C. A., Barker, G. J., Thompson, A. J., and Miller, D. H., 1999. Diffusion tensor imaging of lesions and normal-appearing white matter in multiple sclerosis. *Neurology*. 52(8), 1626-1632.

Worsley, K. J., Marrett, S., Neelin, P., Vandal, A. C., Friston, K. J., and Evans, A. C., 1996. A unified statistical approach for determining significant signals in images of cerebral activation. *Hum Brain Mapp*. 4(1), 58-73.

## Tables

**Table 1:** Clinical and demographics of the study population.

Characteristics	Healthy (n=20)	RR-MS (n=19)	SP-MS (n=15)	p-value Healthy-RR	p-value Healthy- SP	p- value SP-RR
Age (years)	44.60±9.87 (25, 68)	39.45±8.98 (24, 56)	49.34±11.31 (29, 64)	0.10	0.19	0.01
Gender	13m / 7f	6m / 13f	6m / 9f	NA	NA	NA
EDSS	NA	3.05±1.4 (0, 4.5)	5.36±1.14 (3.5, 7)	NA	NA	< 0.001
Lesion loads (milliliters)	NA	21.78±15.93 (3.03, 64.65)	32.70±19.41 (3.69, 60.66)	NA	NA	0.05

**Description:** Lists the mean  $\pm$  standard deviations, the range of the population characteristics (in parenthesis) and the significance values (p-value) of group-wise comparison based on two-sample, two-tailed t-test. The lesion loads are un-normalized loads. NA means not applicable.

**Table 2:** Uncertainty associated with ACMs for increasing number of streamlines.

Number of streamlines	10	50	150	300	500	700
Average CV	0.049	0.023	0.014	0.012	0.011	0.012
Average SNR	20.32	44.21	69.44	85.84	87.42	85.54

**Description:** Shows the average voxel-wise coefficient of variation (CV) and the average signal to noise ratio (SNR) each of these CV/SNR volumes are evaluated from a five-time repeated estimation of the same ACM following which they are averaged for five healthy subjects.

**Table 3:** Regions of significantly decreased ACM of SP-MS relative to RR-MS patients.

Region of interest	Nvox	P <sub>FWE-peak</sub>	MNI-coordinates (x, y, z) - in mm
Pontine crossing tract	41	0.0001	(1, -31, -31)
R-superior longitudinal fasciculus	114	0.004	(41, 13, 31)
L-posterior corona radiata	41	0.005	(-27, -35, 25)
R-posterior corona radiata	18	0.005	(29, 59, 23)
R-superior corona radiata	29	0.006	(25, 3, 21)
R-corticospinal tract	34	0.01	(5, 23, 31)
L-retrolenticular internal capsule	16	0.03	(-35, -37, 7)
R-retrolenticular internal capsule	56	0.038	(27, 29, 9)

**Description:** **Region of interest** is the name of a WM ROI, in the JHU-ICBM-DTI-81 atlas with R/L referring to a hemisphere. **Nvox** are the number of voxels in a region surviving the corrected threshold. **P<sub>FWE-peak</sub>** is the SVC significance of the peak t-test voxel. **MNI-coordinates** are the coordinates of the t-test peak voxel. The horizontal line indicates **P<sub>FWE-peak</sub>** smaller than 0.01 or between 0.01-0.05.

**Table 4:** Region-specific median ACM/FA disease score correlations and GLM analyses.

Region of interest	Pearson's correlation		GLM with correction for age and gender		r <sup>2</sup>	
	ACM	FA	ACM	FA	ACM	FA
Pontine crossing tract	-0.458 (**)	-0.218	0.574 (**)	0.487 (**)	0.329	0.237
R-superior longitudinal fasciculus	-0.468 (**)	-0.301	0.573 (**)	0.507 (**)	0.328	0.257
L-posterior corona radiata	-0.354 (*)	-0.304	0.518 (**)	0.525 (**)	0.270	0.276
R-posterior corona radiata	-0.620 (**)	-0.099	0.699 (**)	0.531 (**)	0.489	0.282
R-superior corona radiata	-0.173	-0.205	0.509 (**)	0.497 (**)	0.259	0.247
R-corticospinal tract	-0.281	-0.164	0.498 (**)	0.499 (**)	0.248	0.249
R-retrolenticular internal capsule	-0.529 (**)	-0.256	0.656 (**)	0.521 (**)	0.431	0.271
L-retrolenticular internal capsule	-0.515 (**)	-0.207	0.594 (**)	0.537 (**)	0.352	0.289

**Description:** **Region of interest** is the name of a WM ROI delineated in the JHU-ICBM-DTI-81 atlas with R/L referring to a hemisphere. **Pearson's correlation**, list the correlation coefficients between the median ACM or the median FA and the EDSS disease scores; (\*) means, p-value<0.05 and (\*\*), p-value<0.01. **GLM with correction** list the correlation between EDSS and the disease score prediction based on a general linear model (GLM) including covariates of age, gender and either the median ACM or median FA. **r<sup>2</sup>** is the coefficient of determination summarizing the percentage of variance explained by the GLM.

## Figures

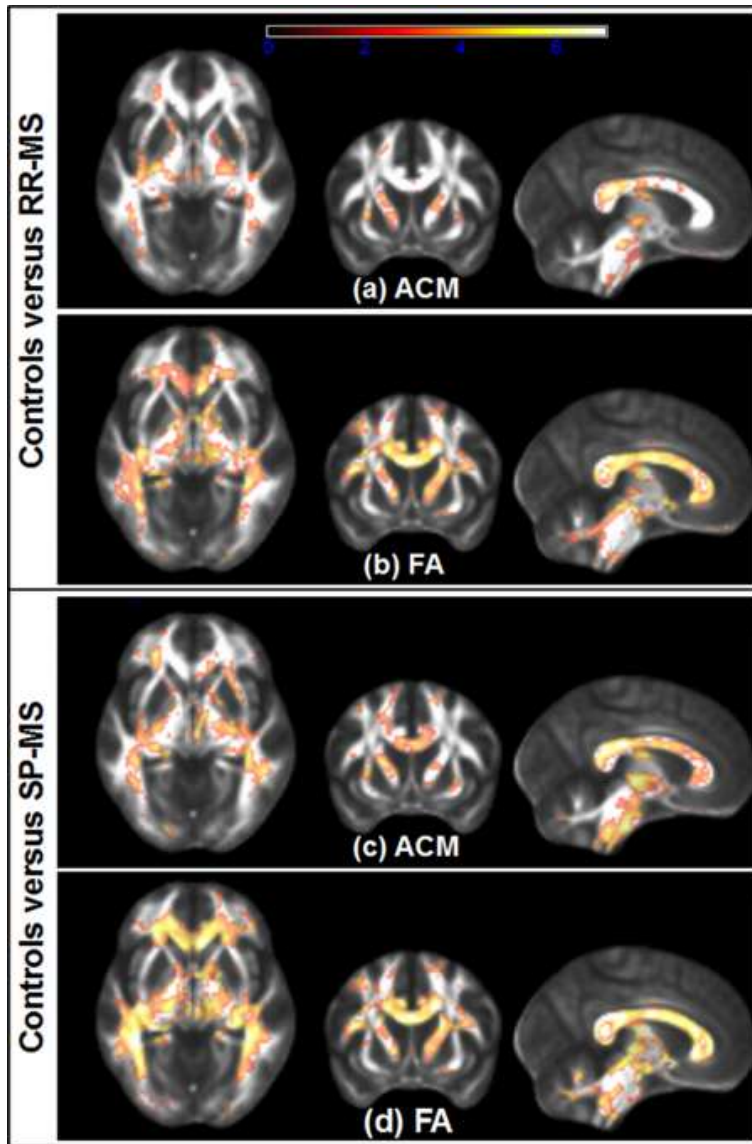


**Fig. 1:** The axial, coronal and sagittal slices of (a)-(d) are shown in neurologic convention. Slices in (a) show the uncorrected voxel-based t-tests, thresholded at significance level 0.005, used to test if the ACMs of RR-MS patients are decreased compared to healthy controls while (b) shows the corresponding, thresholded t-test based on FA. (c) and (d) shows the results of similar group comparisons between SP-MS patients and healthy controls with the voxel-based t-tests derived from ACM depicted in (c) and the t-tests based on FA shown in (d). The background images of (a)-(d) are from the FMRIB58\_FA atlas.

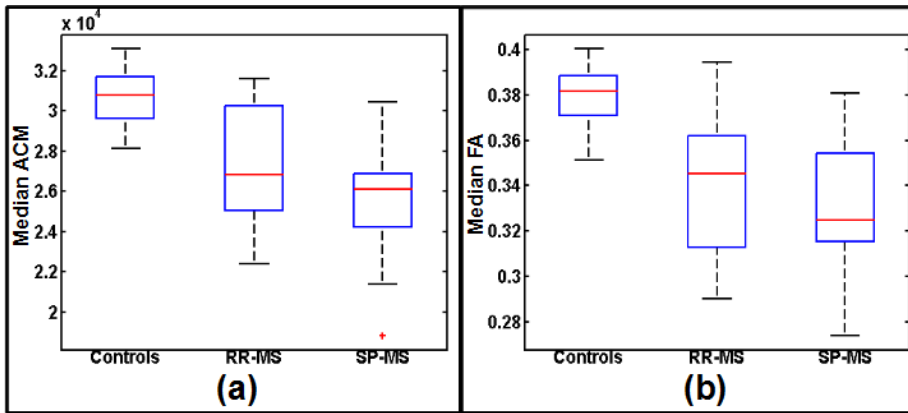


**Fig. 2:** Shows the distribution of the median ACM values within the major cerebral WM. (a) The box plots give the distributions of median ACM values within the cerebral WM region (FMRIB58\_FA>0.25) for healthy controls, RR-MS and the SP-MS patients. (b) The box plots show the corresponding distributions of the median FA values for the entire cerebral WM region.

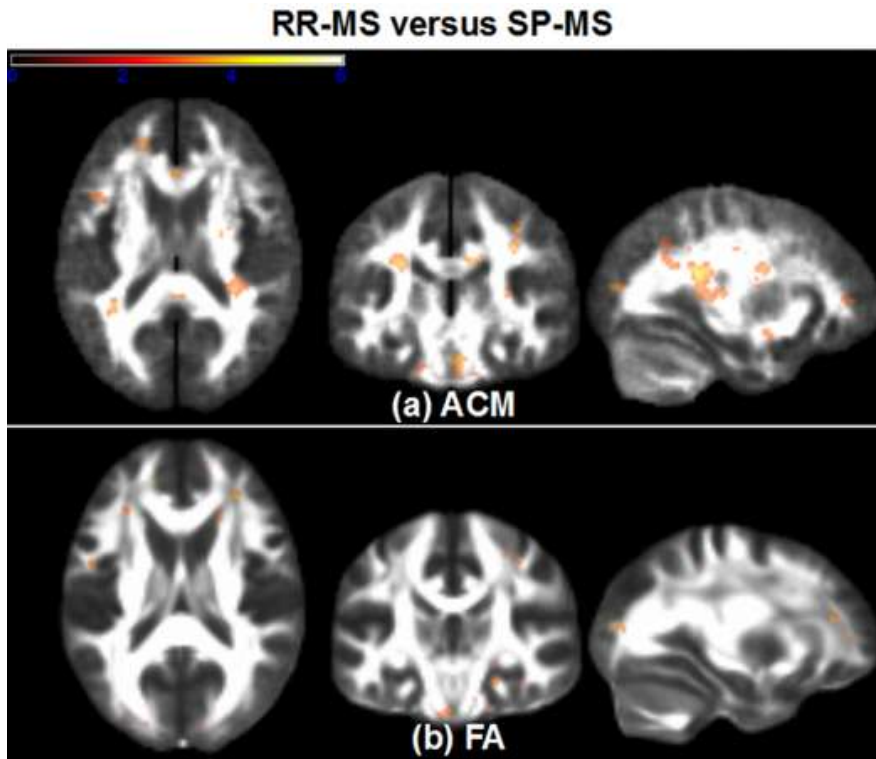


**Fig. 3:** (a) Shows clusters of t-test voxels, thresholded at an uncorrected significance of 0.005, used to test whether the SP-MS patients have significantly reduced connectivity compared to RR-MS patients. The thresholded t-tests voxels are overlaid on the mean ACM and reveal significance at the left posterior corona radiate (coronal slice), the pontine crossing tract (coronal slice) and the right posterior corona radiata (axial and sagittal slice). Similarly, (b) shows the result of testing where the SP-MS patients have a decreased FA compared to the RR-MS patients and only a few significant voxels are found. The t-tests depicted in (a) and (b) have been overlaid the FMRIB58\_FA atlas.

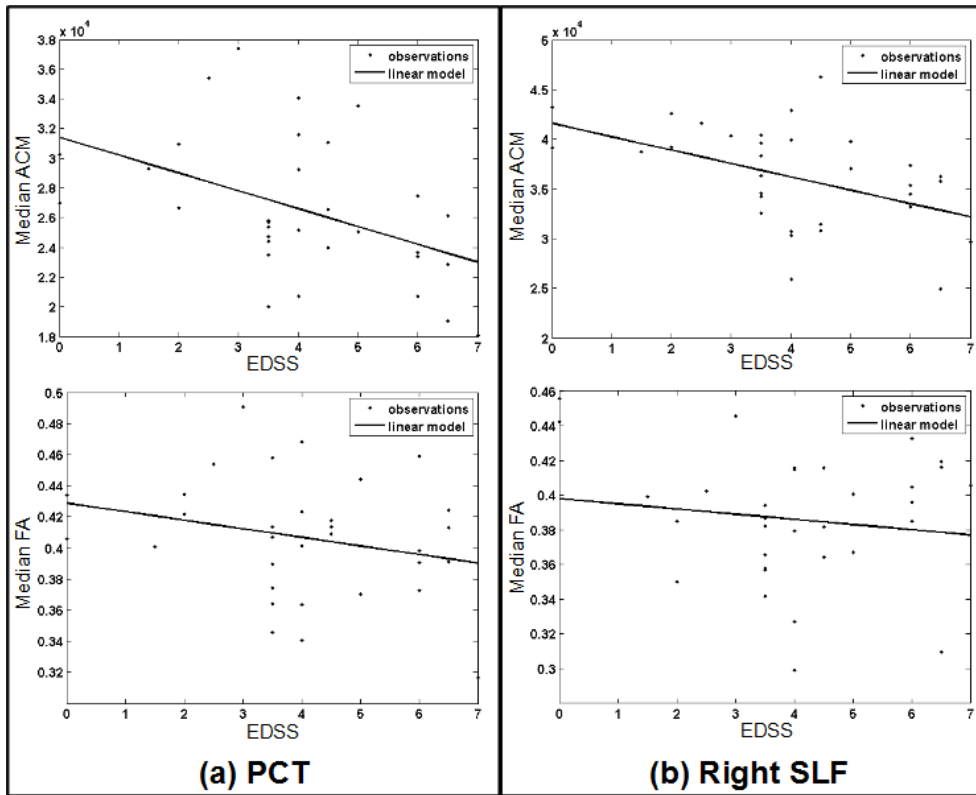


**Fig. 4:** Shows the region-specific median ACM plotted against the EDSS score and the region-specific median FA plotted against EDSS where ACM and FA are sampled from within the same WM ROI of the JHU-ICBM-DTI-81 atlas. The plots also show the GLM (straight line), fitted using the median FA/ACM as depend covariates and the EDSS as the independent. Subfigure (a) shows a cross-subject plot of the median ACM and median FA obtained from the pontine crossing tract (PCT) ROI. Similarly, (b) shows the median ACM and median FA plots based on the right superior longitudinal fasciculus (SLF) ROI.

## CHAPTER 11

# **Segmenting Multiple Sclerosis lesions using a spatially constrained K-Nearest Neighbour approach**

---

Published in Proceedings of the 9th international conference on Image Analysis and Recognition - Volume Part II (ICIAR'12), Springer-Verlag, 156-163,2012.

# Segmenting Multiple Sclerosis Lesions using a Spatially Constrained K-Nearest Neighbour approach

Mark Lyksborg<sup>1</sup>, Rasmus Larsen<sup>1</sup>, Per Soelberg Sørensen<sup>3</sup>, Morten Blinkenberg<sup>3</sup>, Ellen Garde<sup>2</sup>, Hartwig R. Siebner<sup>2</sup>, and Tim Bjørn Dyrby<sup>2</sup>

<sup>1</sup> Technical University of Denmark, Informatics and Mathematical Modeling, DK

<sup>2</sup> Danish Research Centre for Magnetic Resonance, Copenhagen University Hospital Hvidovre, DK

<sup>3</sup> Danish Multiple Sclerosis Research Center, University of Copenhagen, DK

**Abstract.** We propose a method for the segmentation of Multiple Sclerosis lesions. The method is based on probability maps derived from a K-Nearest Neighbours classification. These are used as a non parametric likelihood in a Bayesian formulation with a prior that assumes connectivity of neighbouring voxels. The formulation is solved using the method of Iterated Conditional Modes (ICM). The parameters of the method are found through leave-one-out cross validation on training data after which it is evaluated on previously unseen test data. The multi modal features investigated are 3 structural MRI modalities, the diffusion MRI measures of Fractional Anisotropy (FA), Mean Diffusivity (MD) and several spatial features. Results show a benefit from the inclusion of diffusion primarily to the most difficult cases. Results shows that combining probabilistic K-Nearest Neighbour with a Markov Random Field formulation leads to a slight improvement of segmentations.

## 1 Introduction

The amount of lesions occurring within the White Matter of brain MRI images is commonly used as a biomarker of Multiple Sclerosis (MS) disease progression [1]. In this paper, the biomarker corresponding to the sites of White Matter lesions is determined based on supervised learning.

The main ideas inspiring the work presented in this paper are [3, 5, 6, 7]. In [3] it was suggested to detect lesions as outliers of a statistical model which models the classes White Matter (WM), Grey Matter (GM) and Cerebrospinal Fluid (CSF). The authors suggested to incorporate a Markov Random Field (MRF) to enforce neighbourhood context with initial class labels coming from a parametric statistical model. Similarly we use a MRF solved using Iterated Conditional Modes (ICM) [6] as has also been studied in the context of lesion segmentation in [7] but we take a different approach than [3, 7] in obtaining the initial class labelling and their probabilities. These are based on a non-parametric model from [5] who estimated probability maps from the technique

of K-Nearest Neighbour (K-NN) using MRI modalities combined with the spatial information pertaining to the subjects own coordinate system. The derived K-NN probability maps are finally introduced in a Bayesian formulation using a prior which imposes the constraints of smooth image segmentation.

We investigate the possibility of including two different spatial/coordinate indices and two different Diffusion Tensor Imaging (DTI) [8] indices, namely the FA and MD as segmentation features. The FA and MD are two complementary diffusion indices, measuring the free motion of water molecules within a voxel and have shown to be sensitive towards measuring WM tissue disintegration [2].

It is demonstrated through use of a Similarity Index(SI) [9] and a division of the imaging material into training and validation data, that diffusion MRI yields an improvement to the lesion classification and that the inclusion spatial features are beneficial. Finally the addition of class neighbouring constraint leads to a further improvement of segmentations.

## 2 Data

The MRI images were acquired on a 3 Tesla Siemens scanner. The following modalities were acquired, a T1 weighted MPRAGE image with an isotropic voxel size of  $1mm^3$ , a T2 weighted image and a FLAIR image both having voxel size  $1.1mm^3$ . A Diffusion Weighted Image (DWI) series was acquired using a Twice-Refocused Spin Echo sequence [10] with a b value of  $1200\text{ }mm^{-2}$ , consisting of 71 image volumes of which 61 are diffusion weighted and 10 were acquired with no weighting. The DWI images have the voxel size of  $2.3mm^3$ .

Imaging material from 15 patients was collected and based on FLAIR a radiographer drew lesions in all patients to be used as training data and as a gold standard for measuring segmentation performance. Similarly WM, GM and CSF regions were annotated.

## 3 Preprocessing

RF-inhomogeneity the structural MRI was reduced using the N3 method [11] of Freesurfer and available for download at (<http://surfer.nmr.mgh.harvard.edu/>).

Subject motion was corrected in two steps. First, the T2 and FLAIR modalities were rigidly transformed to the MPRAGE, using the criteria of Mutual Information (MI) and cubic interpolation with SPM8 [12]. Second, the DWI volumes were aligned to each other, EPI corrected [13] and transformed into the space of MPRAGE. The rotational part of the transformations are extracted and gradient directions compensated using the approach in [14]. The DTI model and the derived measures of Fractional Anisotropy (FA) and Mean Diffusivity (MD) were estimated via the Camino software [15].

We investigate 2 possibilities for including spatial feature information.

1) We subtract the 2 axial intensity weighted centre of gravity, from the image coordinates of the FLAIR modality. The longitudinal coordinate remains unmodified. This results in 3 spatial features.

2) The SPM-MNI152 atlas and its WM, GM and CSF probability maps are non-rigidly warped towards the MPRAGE modality of an MS subject. The 3 warped probability maps are included as features and are expected to serve as strong spatial priors given that we only expect lesions in healthy WM regions.

## 4 Method

### 4.1 K-Nearest Neighbour

The idea of a Nearest Neighbour (NN) classification is to classify a voxel based on a supervised dataset (the training data) but with no assumption about the underlying probability function of the data [16]. We denote  $X$  as the feature vector with  $n$  channels so for instance  $X = ([x_1, x_2, \dots, x_{n-1}, x_n], \phi)$ . A training dataset will consist of  $m$  training examples each with a feature vector and a classification label  $\phi$ .  $X_j$  is declared a nearest neighbour to the unseen feature vector  $Y = [x_1, x_2, \dots, x_{n-1}, x_n]$  if

$$j = \underbrace{\operatorname{argmin}_i}_{i} d(X_i, Y), \quad i = 1, 2, \dots, m, \quad (1)$$

where  $d(X, Y) = \|X - Y\|^2$ . To turn the NN classifier into a K-NN classifier, the  $K$  features with the smallest Euclidean differences are kept and classification is usually declared based on the majority vote from features with the same label  $\phi$ . We segment the brain into four classes each with a distinct label,  $\phi = \{CSF, GM, WM, LES\}$  where  $LES$  is the lesion label. The value of  $K$  affects the strength of the classifier and its choice will depend on the class separation in feature space. We construct the training dataset to ensure all classes are equally represented by randomly selecting an  $X$  from each class until the first class become empty. To ensure equal importance of all features, each feature is mean centred and scaled with respect to variance. The K-NN problem is now solved using the freely available software package FLANN [17].

The output of the K-NN classifications are four, 3D images containing the number of votes for a given class. These are transformed into probability maps, with a probability being the number of votes for a given label divided by  $K$ . A threshold can be used to obtain binary segmentations. This threshold has to be chosen to optimally classify lesions. We use it to scale probabilities such that we can continue working with the probability that a voxel takes on a given label.

### 4.2 Including neighbourhood context

Since K-NN only sees one voxel at the time it cannot emulate human behaviour of seeing spatial context. We thus suggest to modify the K-NN probabilities to respect spatial class coherence. It is enforced through a Markov Random Field (MRF) formulation. Lets denote the outcome of labelling an image as a stochastic variable  $\phi_i$ ,  $i = 1 \dots n$ , limited to take on the discrete values of

$\phi = \{CSF = 1, GM = 2, WM = 3, LES = 4\}$ . An MRF is specified using a Gibbs distribution

$$P_\phi = \frac{1}{Z} e^{-\sum_c V_c(\phi)} \quad (2)$$

where  $c$  denotes an index over all voxels and  $V_c$  the neighbourhood interaction potential function.  $Z$  is a normalization constant which can safely be ignored. The expression in Eq. (2) plays the role of a prior when used with Bayes rule

$$P_{\phi|Y} = \frac{P_{Y|\phi} \cdot P_\phi}{P_Y} \propto P_{Y|\phi} \cdot P_\phi \quad (3)$$

which gives a posterior probability of labelling given data. In previous applications [3] the likelihood  $P_{Y|\phi}$  is often based on a Gaussian probability function. Here the probability maps estimated from the K majority voting are proposed instead. If we choose a simple interaction potential considering only 6 neighbours in 3D, we can combine Eq. (2) and (3) into

$$P_{\phi|Y} = P_{Y|\phi} \cdot e^{-\sum_c \sum_{i,j,k \in n(c)} \beta(\phi, \phi_{ijk}) \cdot [1 - \delta(\phi, \phi_{ijk})]}. \quad (4)$$

This multi class prior is known as the Potts model [6] where  $\beta$  is a 4x4 matrix of entries penalising neighbourhood transitions. For instance  $\beta$  is larger than zero for  $LES \rightarrow GM$  neighbour transitions. Hereby encoding the assumption that lesions voxels are usually not neighbours to gray matter voxels. The entry for the transition  $LES \rightarrow WM$  is set to zero since this neighbourhood is expected and should not be penalised. The notation  $n(c)$  defines the neighbour indices which are of the simplest form consisting of 6 neighbours in 3D and  $\delta$  is the Kronecker delta function evaluating to 0 or 1. Equation (4) is solved using ICM ensuring only a local optimum.

## 5 Experiments and Results

### 5.1 Optimal K and threshold

To determine the optimal value of  $K$  and the probabilistic *threshold*, leave-one-out cross validations are made for different combinations of  $K$  and *thresholds* while some subjects are left out to perform test validation upon. We vary  $K$  from 40 – 220 in steps of 20 and divide the interval  $[0.55, 1]$  into 45 distinct and equidistantly spaced thresholds. Since 15 subjects is a low number to train the model and test on, 3 nested cross validation were performed instead by splitting the data 3 times, into a training set of 10 and a test sets of 5 subjects. Some overlap exist between the training data but none between the 3 times 5 test data. This yield a total of 30 cross validations and 15 test subjects that have not been seen by the model. To measure performance, the Similarity Index (SI) [9], also known as the Dice score and the Overlap Fraction(OF) are used. They are estimated according to Eq. (5)

$$SI = \frac{2|V_{ref} \cap V_{seg}|}{|V_{ref}| + |V_{seg}|}, \quad OF = \frac{|V_{ref} \cap V_{seg}|}{|V_{ref}|}, \quad (5)$$

where  $V_{ref}$  is the segmentation of the radiographer and  $V_{seg}$  is the segmentation of the method.

The results of running one such cross validation experiment with the probabilistic K-NN using a training set with a total of approximately  $10^6$  feature vectors divided amongst the 4 classes and using the features of MPRAGE, T2 and FLAIR is shown in Fig. 1. The plot shows the median SI surface for the 10 cross validations as a function of  $K$  and threshold. In this case the best solution is found at  $K = 100$  and  $threshold = 0.96$ . This threshold is consistent across the 3 nested validations while the best performing  $K$  was 80 and 100 for the two other validations. The general observation is that decreasing  $K$  gave decreasingly worse performance. The average of 3 median SI score serve as a baseline for improvement using more features and is listed under the MTF abbreviation in Table 1.

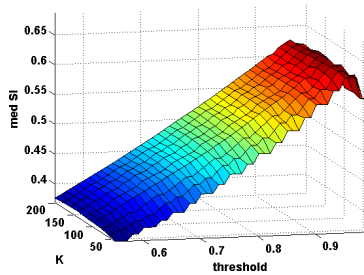


**Fig. 1.** Shows the median SI over 10 leave-one-out validations as a function of threshold and the number of nearest neighbours  $K$

## 5.2 Feature selection

To find the most appropriate features for segmentations we investigate a subset of combinations. In all experiments MPRAGE, T2 and FLAIR are included as baseline features, as it has been demonstrated in [18] that lesion segmentations can benefit from including all three. Each additional feature is included in turn. Instead of repeatedly showing curves corresponding to Fig. 1, we compile the best results for each feature combination in Table 1. It shows both the training and test results using the probabilistic K-NN. The best SI was found to be using MPRAGE, T2, FLAIR, the normal probability maps and FA. The contribution of FA is comparably small and was found to be largest in patients with the small lesion loads. We further observe that test scores with probability maps are generally better compared to centroid corrected coordinates. This suggest that centroid corrected features are overly biased towards training data compared to normal probability maps.

## 5.3 Improving segmentations using ICM

Having identified a feature combination, its  $K$  and the  $threshold$ , Eq. (4) is solved. Suitable values of  $\beta$  are identified by fixing all previously mentioned

**List of feature abbreviations used for Table 1**

MTF	MPRAGE, T2 and FLAIR
FA	Fractional Anisotropy
MD	Mean Diffusivity
xyz	Slice wise mass-centroid corrected coordinates
M	Normal WM, GM and CSF probability maps, from MNI

Features	Leave-one-out validation				Test results			
	med SI	min SI	max SI	med OF	med SI	min SI	max SI	med OF
MTF	0.644	0.303	0.838	0.668	0.618	0.394	0.825	0.688
MTF, MD	0.661	0.337	0.839	0.693	0.643	0.418	0.834	0.698
MTF, FA	0.656	0.360	0.840	0.694	0.648	0.406	0.835	0.716
MTF, MD, FA	0.666	0.383	0.848	0.712	0.678	0.430	0.839	0.727
MTF, M	0.682	0.367	0.853	0.724	0.679	0.401	0.836	0.751
MTF, M, FA	0.705	0.402	0.850	0.716	0.702	0.467	0.837	0.743
MTF, M, MD, FA	0.701	0.389	0.845	0.707	0.677	0.459	0.843	0.700
MTF, xyz	0.680	0.345	0.839	0.713	0.668	0.419	0.842	0.720
MTF, xyz, FA	0.681	0.361	0.841	0.721	0.676	0.434	0.842	0.729

**Table 1.** Lists the average results for the optimal parameters estimate over 3 cross validation and test experiments. The first column lists the feature combinations. Columns 2-4 shows the average SI over the 3 cross validations while column 5 shows the average of the median overlap fraction. Based on the optimal parameters estimate from from cross validation, the test results of column 6-9 are achieved. The features with best performance have been highlighted in gray.

parameters and varying  $\beta$ . Again we perform leave-one-out cross validation for a set of  $\beta$  values. This validation lead to choosing  $\beta=0.1$  whereby the average SI performance over the 30 validations is increased by 0.0105 thus increasing the best average of the median SI training scores from 0.705 to 0.716. This choice of  $\beta$  further results in a test score of 0.713. To visually verify the effect of these numbers for the best performing features, Fig. 2(a) shows a transversal slice of the FLAIR modality. For the same slice, Fig. 2(b) shows the K-NN lesion probability map. Figure 2(c) contains lesions as manually annotated by a radiographer and (d) the thresholded segmentation of the K-NN approach using  $K = 100$  and  $threshold = 0.96$ . A number of false lesion voxels are observed in Fig. 2(d) and by solving Eq. (4) these are reduced as indicated in Fig. 2(e). In practice better results can be obtained if the radiographer changes  $\beta$  on a per subject basis.

#### 5.4 Comparing to other types of classification

The K-NN+ICM method was compared to the freely available unsupervised and parametric method of [3]. The best performing parameters of [3] were determined using cross validation on training data and applied to test data. It achieved a median SI training score of 0.470 and a test score of 0.453. The method of [3] is unsupervised and only considers the inclusion of FLAIR, MPRAGE and T2. We therefore also compare it to a Support Vector Machine (LIBSVM) approach [4] based on FLAIR, MPRAGE, T2, FA and normal appearing probability maps of MNI space. The median training score was found to be 0.492 and the median test score was 0.48. Thus K-NN+ICM outperformed both the parametric and the more advance non parametric approach. Five of the subjects in the study

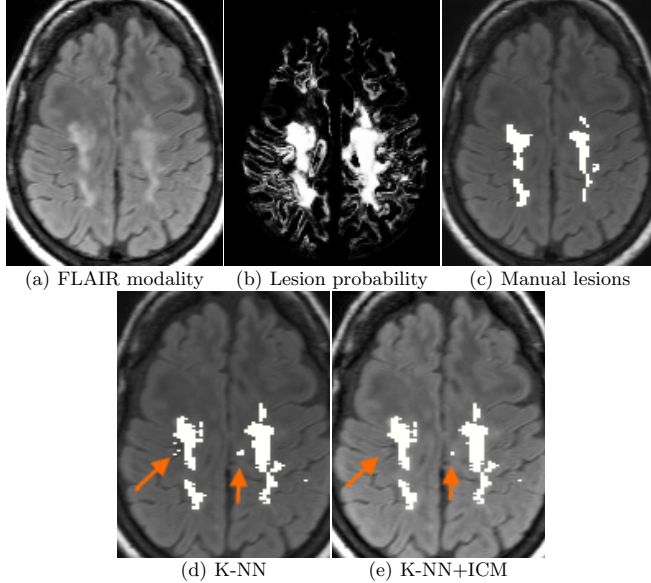


**Fig. 2.** (a) Shows the FLAIR modality and (b) the matching lesion probability map using the K-NN. (c) shows the manual segmentation while (d) shows the thresholded segmentation of the K-NN method. Finally (e) shows the segmentation achieved using K-NN and ICM. The arrows in (d) show false positive, removed in (e)

had been annotated by two different raters. The median SI score, between the two raters was 0.739 indicating that manual raters are better at segmenting. Further the first rater had repeated the annotations 3 times per subject with a median within SI score of 0.8939.

## 6 Summary

We have investigated and performed validation experiments for selecting appropriate features to include in a probabilistic K-NN classifier with MRF. Despite a lower acquisition resolution of the diffusion weighted images the inclusion of FA increased the specificity of the segmentation. This demonstrates that the modality offers some complementary information useful for lesion segmentation. The spatial features of normal probability maps warped non linearly from MNI space were found to be better than that of centroid corrected native coordinates. With further experimentation of the registration parameters for spatially normalizing the normal probability maps we expect this could become an even better feature. Finally, based on the optimal choice of features it was demonstrated how the combination of the non parametric K-NN probabilities and ICM results in improved segmentations when comparing to the K-NN itself as well as other methods. Since ICM only guarantees convergence to a local optimum,

future works is to investigate methods that guarantees solutions closer to the optimum [19].

## References

- [1] Filippi, M., Horsfield MA., Morrissey SP., MacManus DG., Rudge P., McDonald WL., Miller DH.: Quantitative brain MRI lesion load predicts the course of clinically isolated syndromes suggestive of multiple sclerosis. *Neurology*, **44**(4) (1994) 635–641
- [2] Filippi, M. and Cercignani, M. and Inglese, M. and Horsfield, M. A. and Comi, G.: Diffusion tensor magnetic resonance imaging in multiple sclerosis. *Neurology*, **56**(3) (2001) 304–311
- [3] Van Leemput K., Maes F., Vandermeulen D., Colchester A., Suetens P.: Automated segmentation of multiple sclerosis lesions by model outlier detection. *IEEE Trans. Med. Imaging*, **20**(8) (2004) 677–688
- [4] Chang, Chih-Chung, Lin, Chih-Jen: LIBSVM: A library for support vector machines. *ACM Trans. on Intelligent Systems and Technology*, **2**(3) (2011) 27:1–27:27
- [5] Anbeek P., Vincken KL., van Osch M.J.P., Bisschops RHC., van der Grond J.: Probabilistic segmentation of white matter lesions in MR imaging. *NeuroImage*, **21** (2004) 1037–1044
- [6] Besag J.: On the statistical analysis of dirty pictures. *Journal of the Royal Statistics Society B*, **48** (1986) 259–302
- [7] Johnston B., Atkins MS., Booth KS.: Partial volume segmentation in 3D of lesions and tissues in magnetic resonance images. *Proceedings of SPIE: Medical Imaging* 1994, **2167** (1994) 28–39
- [8] Basser P.J., Mattiello J., Le Bihan D.: MR diffusion tensor spectroscopy and imaging. *Biophys J* **66**(1) (1994) 259–267
- [9] Dice LR.: Measures of the Amount of Ecologic Association Between Species. *Ecology* **26** (3) (1945) 297–302
- [10] Reese TG., Heid O., Weisskoff RM., Wedeen VJ.: Reduction of eddy-current-induced distortion in diffusion mri using a twice-refocused spin echo. *Magn. Reson. Med.*, **49** (2003) 177–182
- [11] Sled JG., Zijdenbos AP., Evans AC.: A Nonparametric Method for Automatic Correction of Intensity Nonuniformity in MRI Data. *IEEE Trans. on Medical Imaging*, **17** (1998) 87–97
- [12] Collignon A., Maes F., Delaere D., Vandermeulen D., Suetens P., Marchal G.: Automated Multi-modality Image Registration Based On Information Theory. *Medical Imaging*, (1995) 263–274
- [13] Jezzard P., Balaban RS.: Correction for geometric distortion in echo planar images from Bo field variations. *Magn. Reson. Med.*, **34**(1) (1995) 65–73
- [14] Alexander DC., Pierpaoli C., Basser P.J., Gee, J.C.: Spatial transformations of diffusion tensor magnetic resonance images. *IEEE Trans. on Medical Imaging*, **20**(11) (2001) 1131–1139
- [15] Cook PA., Bai Y., Nedjati-Gilani S., Seunarine KK., Hall MG., Parker G.J., Alexander DC.: Camino: Open-Source Diffusion-MRI Reconstruction and Processing. 14th Scientific Meeting of the International Society for Magnetic Resonance in Medicine, (2006) 27–59
- [16] Cover TM., Hart PE.: Nearest Neighbor Pattern Classification. *IEEE Trans. On Information Theory*, **13** (1967) 21–27
- [17] Muja M., Lowe DG.: Fast Approximate Nearest Neighbors with Automatic Algorithm Configuration. *Int. Conf. on Computer Vision Theory and Application-VISSAPP09*, (2009) 331–340
- [18] Dyrby TB., Rostrop E., Baare FC., Straaten ECW., Barkhof F., Vrenken H., Ropele S., Schmidt R., Erkinjuntti T., Wahlund LO., Pantoni L., Inzitari D., Paulson OB., Hansen LK., Waldemar G.: Segmentation of age related white matter changes in a clinical multi-center study. *NeuroImage*, **41** (2008) 335–345
- [19] Boykov Y., Veksler O., Zabih R.: Fast approximate energy minimization via graph cuts. *IEEE Trans. Pattern Analysis and Machine Intelligence*, **23**(11) (2001) 1222–1239



# Bibliography

---

- [1] D. C. Alexander. Maximum entropy spherical deconvolution for diffusion mri. *Inf Process Med Imaging*, 19:76–87, 2005.
- [2] D. C. Alexander. Multiple-fiber reconstruction algorithms for diffusion mri. *Ann N Y Acad Sci*, 1064:113–133, Dec 2005.
- [3] D. C. Alexander, G. Barker, and S. Arridge. Detection and modelling of non-gaussian apparent diffusion coefficient profiles in human brain data. *Magnetic Resonance in Medicine*, 48:331–340, 2002.
- [4] D. C. Alexander and G. J. Barker. Optimal imaging parameters for fiber-orientation estimation in diffusion mri. *Neuroimage*, 27(2):357–367, Aug 2005.
- [5] D. C. Alexander, C. Pierpaoli, P. J. Basser, and J. C. Gee. Spatial transformations of diffusion tensor magnetic resonance images. *IEEE Trans Med Imaging*, 20(11):1131–1139, Nov 2001.
- [6] P. Anbeek, K. L. Vincken, M. J. P. van Osch, R. H. C. Bisschops, and J. van der Grond. Probabilistic segmentation of white lesions in MR imaging. *Neuroimage*, 21(3):1037–1044, Mar. 2004.
- [7] V. Arsigny, P. Fillard, X. Pennec, and N. Ayache. Log-euclidean metrics for fast and simple calculus on diffusion tensors. *Magn Reson Med*, 56(2):411–421, Aug 2006.
- [8] V. Arsigny, X. Pennec, and N. Ayache. Polyrigid and polyaffine transformations: a novel geometrical tool to deal with non-rigid deformations - application to the registration of histological slices. *Med Image Anal*, 9(6):507–523, Dec 2005.

- [9] A. Ascherio, K. L. Munger, and K. C. Simon. Vitamin d and multiple sclerosis. *Lancet Neurol*, 9(6):599–612, Jun 2010.
- [10] J. Ashburner and K. J. Friston. Nonlinear spatial normalization using basis functions. *Human Brain Mapping*, 7:254–266, 1999.
- [11] L. Bø. The histopathology of grey matter demyelination in multiple sclerosis. *Acta Neurol Scand Suppl*, (189):51–57, 2009.
- [12] P. J. Basser. Inferring microstructural features and the physiological state of tissues from diffusion-weighted images. *NMR Biomed*, 8(7-8):333–344, 1995.
- [13] P. J. Basser, S. Pajevic, C. Pierpaoli, J. Duda, and A. Aldroubi. In vivo fiber tractography using dt-mri data. *Magn Reson Med*, 44(4):625–632, Oct 2000.
- [14] P. J. Basser and C. Pierpaoli. Microstructural and physiological features of tissues elucidated by quantitative-diffusion-tensor mri. *J Magn Reson B*, 111(3):209–219, Jun 1996.
- [15] T. Bayes. An essay towards solving a problem in the doctrine of chances. *Phil. Trans. of the Royal Soc. of London*, 53:370–418, 1763.
- [16] T. E. J. Behrens, M. W. Woolrich, M. Jenkinson, H. Johansen-Berg, R. G. Nunes, S. Clare, P. M. Matthews, J. M. Brady, and S. M. Smith. Characterization and propagation of uncertainty in diffusion-weighted mr imaging. *Magn Reson Med*, 50(5):1077–1088, Nov 2003.
- [17] H. C. Berg. *Random Walks in Biology*. Princeton University Press, revised edition, Sept. 1993.
- [18] J. Besag. On the statistical analysis of dirty pictures. *Journal of the Royal Statistical Society*, B-48:259–302, 1986.
- [19] K. K. Bhatia, J. V. Hajnal, B. K. Puri, A. D. Edwards, and D. Rueckert. Consistent groupwise non-rigid registration for atlas construction. In *Proceedings of the IEEE Symposium on Biomedical Imaging (ISBI)*, pages 908–911, 2004.
- [20] C. Bingham. An antipodally symmetric distribution on the sphere. *The Annals of Statistics*, 2(6):1201–1225, 1974.
- [21] F. L. Bookstein. Principal warps:Thin-Plate splines and the decomposition of deformations. *IEEE Tran Pattern anal.*, 11(6):567–585, jun 1989.
- [22] F. L. Bookstein. Thin-plate splines and the atlas problem for biomedical images. In *Proceedings of the 12th International Conference on Information Processing in Medical Imaging*, IPMI '91, pages 326–342, London, UK, UK, 1991. Springer-Verlag.

- [23] Y. Boykov, O. Veksler, and R. Zabih. Fast approximate energy minimization via graph cuts. *IEEE Trans. Pattern Anal. Mach. Intell.*, 23(11):1222–1239, Nov. 2001.
- [24] M. Bozzali, G. J. M. Parker, L. Serra, K. Embleton, T. Gili, R. Perri, C. Caltagirone, and M. Cercignani. Anatomical connectivity mapping: a new tool to assess brain disconnection in alzheimer’s disease. *Neuroimage*, 54(3):2045–2051, Feb 2011.
- [25] M. Bozzali, B. Spanò, G. Parker, G. Giuliotti, M. Castelli, B. Basile, S. Rossi, L. Serra, G. Magnani, U. Nocentini, C. Caltagirone, D. Centonze, and M. Cercignani. Anatomical brain connectivity can assess cognitive dysfunction in multiple sclerosis. *Mult Scler*, Jan 2013.
- [26] S. Cader, H. Johansen-Berg, M. Wylezinska, J. Palace, T. E. Behrens, S. Smith, and P. M. Matthews. Discordant white matter n-acetylaspartate and diffusion mri measures suggest that chronic metabolic dysfunction contributes to axonal pathology in multiple sclerosis. *Neuroimage*, 36(1):19–27, May 2007.
- [27] Y. Cao, M. I. Miller, S. Mori, R. L. Winslow, and L. Younes. Diffeomorphic matching of diffusion tensor images. In *Proceedings of the 2006 Conference on Computer Vision and Pattern Recognition Workshop, CVPRW ’06*, pages 67–, Washington, DC, USA, 2006. IEEE Computer Society.
- [28] A. Ceccarelli, M. A. Rocca, E. Pagani, A. Ghezzi, R. Capra, A. Falini, G. Scotti, G. Comi, and M. Filippi. The topographical distribution of tissue injury in benign ms: a 3t multiparametric mri study. *Neuroimage*, 39(4):1499–1509, Feb 2008.
- [29] M. Cercignani, K. Embleton, G. J. M. Parker, and M. Bozzali. Group-averaged anatomical connectivity mapping for improved human white matter pathway visualisation. *NMR Biomed*, 56(7):1224–1233, 2012.
- [30] C.-C. Chang and C.-J. Lin. Libsvm: A library for support vector machines. *ACM Trans. Intell. Syst. Technol.*, 2(3):27:1–27:27, May 2011.
- [31] H. Chang and J. M. Fitzpatrick. A technique for accurate magnetic resonance imaging in the presence of field inhomogeneities. *IEEE Transactions in Medical Imaging*, 11(3):319–329, 1992.
- [32] L.-C. Chang, L. Walker, and C. Pierpaoli. Informed restore: A method for robust estimation of diffusion tensor from low redundancy datasets in the presence of physiological noise artifacts. *Magn Reson Med*, 68(5):1654–1663, Nov 2012.
- [33] J. Charcot. *Histologie de la sclérose en plaques*. 1868.

- [34] O. Ciccarelli, T. E. Behrens, D. R. Altmann, R. W. Orrell, R. S. Howard, H. Johansen-Berg, D. H. Miller, P. M. Matthews, and A. J. Thompson. Probabilistic diffusion tractography: a potential tool to assess the rate of disease progression in amyotrophic lateral sclerosis. *Brain*, 129(Pt 7):1859–1871, Jul 2006.
- [35] O. Ciccarelli, D. J. Werring, G. J. Barker, C. M. Griffin, C. A. M. Wheeler-Kingshott, D. H. Miller, and A. J. Thompson. A study of the mechanisms of normal-appearing white matter damage in multiple sclerosis using diffusion tensor imaging—evidence of wallerian degeneration. *J Neurol*, 250(3):287–292, Mar 2003.
- [36] O. Ciccarelli, D. J. Werring, C. A. Wheeler-Kingshott, G. J. Barker, G. J. Parker, A. J. Thompson, and D. H. Miller. Investigation of ms normal-appearing brain using diffusion tensor mri with clinical correlations. *Neurology*, 56(7):926–933, Apr 2001.
- [37] A. Collignon, F. Maes, D. Delaere, D. Vandermeulen, P. Suetens, and G. Marchal. *Automated multi-modality image registration based on information theory*, volume 14, pages 263–274. Kluwer Academic Publishers, 1995.
- [38] D. L. Collins and A. C. Evans. ANIMAL: Validation and applications of Non-Linear Registration-Based segmentation. *International Journal of Pattern Recognition and Artificial Intelligence*, 11:1271–1294, 1997.
- [39] A. Compston and A. Coles. Multiple sclerosis. *The Lancet*, 359(9313):1221–1231, 2002.
- [40] A. Compston and A. Coles. Multiple sclerosis. *The Lancet*, 372(9648):1502–1517, Oct 2008.
- [41] P. A. Cook, Y. Bai, S. Nedjati-Gilani, K. K. Seunarine, M. G. Hall, G. J. Parker, and D. C. Alexander. Camino: Open-source diffusion-mri reconstruction and processing. In *14th Scientific Meeting of the International Society for Magnetic Resonance in Medicine*, 2006.
- [42] I. Corouge, P. T. Fletcher, S. Joshi, S. Gouttard, and G. Gerig. Fiber tract-oriented statistics for quantitative diffusion tensor mri analysis. *Med Image Anal*, 10(5):786–798, Oct 2006.
- [43] T. Cover and P. Hart. Nearest neighbor pattern classification. *Information Theory, IEEE Transactions on*, 13(1):21–27, Jan. 1967.
- [44] K. Curran and D. Alexander. Diffusion tensor orientation matching for image registration. In M. Sonka and J. M. Fitzpatrick, editors, *Society of*

- Photo-Optical Instrumentation Engineers (SPIE) Conference Series*, volume 5032 of *Society of Photo-Optical Instrumentation Engineers (SPIE) Conference Series*, pages 149–156, May 2003.
- [45] L. R. Dice. Measures of the amount of ecologic association between species. *Ecology*, 26(3):297–302, July 1945.
- [46] A. J. Dobson. *An Introduction to Generalized Linear Models*. Chapman & Hall/CRC, 2002.
- [47] A.-M. Dogonowski. *Resting-state Functional Connectivity of the Motor System in Multiple Sclerosis*. PhD thesis, Faculty of Medical and Health Sciences, University of Copenhagen, 2012.
- [48] N. Draper and H. Smith. *Applied Regression Analysis*. Wiley, New York, NY, second edition, 1981.
- [49] O. J. Dunn. Multiple comparisons among means. *Journal of the American Statistical Association*, 56:52–64, 1961.
- [50] D. A. Dymant, G. C. Ebers, and A. D. Sadovnick. Genetics of multiple sclerosis. *Lancet Neurol*, 3(2):104–110, Feb 2004.
- [51] T. B. Dyrby, L. V. Sogaard, G. J. Parker, D. C. Alexander, N. M. Lind, W. F. C. Baare, A. H. Schmidt, N. Eriksen, B. Pakkenberg, O. B. Paulson, and J. Jelsing. Validation of in vitro probabilistic tractography. *NEUROIMAGE*, 37(4):1267–1277, 2007.
- [52] A. Einstein. Über die von der molekularkinetischen Theorie der Wärme geforderte Bewegung von in ruhenden Flüssigkeiten suspendierten Teilchen. *Ann. Phys.*, 322(8):549–560, 1905.
- [53] K. V. Embleton, D. M. Morris, H. A. Haroon, M. A. L. Ralph, and G. J. Parker. Anatomical connectivity mapping. In *Proc. Intl. Soc. Mag. Reson. Med.* 15, 2007.
- [54] A. C. Evans, D. L. Collins, S. R. Millst, E. D. Brown, R. L. Kelly, and T. M. Peters. 3d statistical neuroanatomical models from 305 MRI volumes. In I.-N. S. Symposium, , and M. I. Conference, editors, *Symposium, IEEE-Nuclear S. and and Medical Imaging Conference*, pages 1813–1817, 1993.
- [55] M. Filippi, M. Cercignani, M. Inglese, M. A. Horsfield, and G. Comi. Diffusion tensor magnetic resonance imaging in multiple sclerosis. *Neurology*, 56(3):304–311, Feb 2001.

- [56] M. Filippi, M. A. Horsfield, S. P. Morrissey, D. G. MacManus, P. Rudge, W. I. McDonald, and D. H. Miller. Quantitative brain mri lesion load predicts the course of clinically isolated syndromes suggestive of multiple sclerosis. *Neurology*, 44(4):635–641, Apr 1994.
- [57] M. Filippi and M. A. Rocca. Mr imaging of multiple sclerosis. *Radiology*, 259(3):659–681, Jun 2011.
- [58] M. Filippi and M. A. Rocca. The neurologist’s dilemma: Ms is a grey matter disease that standard clinical and mri measures cannot assess adequately—no. *Mult Scler*, 18(5):557–558, May 2012.
- [59] M. Filippi, M. A. Rocca, F. Barkhof, W. Brück, J. T. Chen, G. Comi, G. DeLuca, N. De Stefano, B. J. Erickson, N. Evangelou, F. Fazekas, J. J. G. Geurts, C. Lucchinetti, D. H. Miller, D. Pelletier, B. F. G. Popescu, H. Lassmann, and A. o. t. C. b. P. M. R. I. f. i. M. S. w. . Association between pathological and mri findings in multiple sclerosis. *Lancet Neurol*, 11(4):349–360, Apr 2012.
- [60] B. Fischl, D. H. Salat, E. Busa, M. Albert, M. Dieterich, C. Haselgrove, A. van der Kouwe, R. Killiany, D. Kennedy, S. Klaveness, A. Montillo, N. Makris, B. Rosen, and A. M. Dale. Whole brain segmentation: automated labeling of neuroanatomical structures in the human brain. *Neuron*, 33(3):341–55+, 2002.
- [61] P. T. Fletcher and S. Joshi. Principal geodesic analysis on symmetric spaces: Statistics of diffusion tensors. In *In: ECCV Workshops CVAMIA and MMBIA. (2004) 87?98*, pages 87–98. Springer-Verlag, 2004.
- [62] R. Fletcher. *Practical methods of optimization; (2nd ed.)*. Wiley-Interscience, New York, NY, USA, 1987.
- [63] L. M. J. Florack, B. M. T. H. Romeny, J. J. Koenderink, and M. A. Viergever. Scale and the differential structure of images. *Image and Vision Computing*, 10:376–388, 1992.
- [64] G. E. Forsythe, M. A. Malcolm, and C. B. Moler. *Computer Methods for Mathematical Computations*. Prentice-Hall, Englewood Cliffs, NJ, 1977.
- [65] F. Frenet. Sur les courbes à double courbure. *Journal de Mathématiques Pures et Appliquées*, 17:437–447, 1852.
- [66] K. J. Friston, A. Holmes, J. B. Poline, C. J. Price, and C. D. Frith. Detecting activations in PET and fMRI: Levels of inference and power. *Neuroimage*, 40:223–235, 1996.

- [67] A. Gallo, M. Rovaris, R. Riva, A. Ghezzi, B. Benedetti, V. Martinelli, A. Falini, G. Comi, and M. Filippi. Diffusion-tensor magnetic resonance imaging detects normal-appearing white matter damage unrelated to short-term disease activity in patients at the earliest clinical stage of multiple sclerosis. *Arch Neurol*, 62(5):803–808, May 2005.
- [68] D. H. Gilden. Infectious causes of multiple sclerosis. *Lancet Neurol*, 4(3):195–202, Mar 2005.
- [69] D. H. Gilden, M. E. Devlin, M. P. Burgoon, and G. P. Owens. The search for virus in multiple sclerosis brain. *Mult Scler*, 2(4):179–183, Nov 1996.
- [70] C. B. Goodlett, P. T. Fletcher, J. H. Gilmore, and G. Gerig. Group analysis of dti fiber tract statistics with application to neurodevelopment. *Neuroimage*, 45(1 Suppl):S133–S142, Mar 2009.
- [71] A. Greenbaum. *Iterative methods for solving linear systems*. Society for Industrial and Applied Mathematics, Philadelphia, PA, USA, 1997.
- [72] T. E. B. Heidi Johansen-Berg. *Diffusion MRI: From quantitative measurement to in-vivo neuroanatomy*. ELSEVIER, 2009.
- [73] D. Holland, J. M. Kuperman, and A. M. Dale. Efficient correction of inhomogeneous static magnetic field-induced distortion in echo planar imaging. *NeuroImage*, 50(1):175–183, 2010.
- [74] R. Hooke and T. A. Jeeves. “direct search” solution of numerical and statistical problems. *J. ACM*, 8(2):212–229, Apr. 1961.
- [75] H. Hotelling. The generalization of student’s ratio. *The Annals of Mathematical Statistics*, 2:360–378, Aug. 1931.
- [76] H. Hou and H. Andrews. Cubic splines for image interpolation and digital filtering. *Acoustics, Speech and Signal Processing, IEEE Transactions on*, 26(6):508–517, Jan. 2003.
- [77] U. Inria, S. Antipolis, J.-P. Thirion, A. Guimond, A. Guimond, J. Meunier, J. Meunier, and P. Epidaure. Average brain models: A convergence study. *Computer Vision and Image Understanding*, 77(77):192–210, 1999.
- [78] M. J. Jesper L. R. Andersson and S. Smith. Non-linear registration aka spatial normalisation , fmrib technical report tr07ja2. Technical report, FMRIB Centre, Oxford, United Kingdom, 2007.
- [79] P. Jezzard and R. S. Balaban. Correction for geometric distortion in echo planar images from b0 field variations. *Magn Reson Med*, 34(1):65–73, Jul 1995.

- [80] I. T. Jolliffe. Principal component analysis, 2nd ed., April 2002.
- [81] D. K. Jones. *Diffusion MRI: Theory, Methods, and Applications*. Oxford University Press, 2011.
- [82] D. K. Jones and M. Cercignani. Twenty-five pitfalls in the analysis of diffusion mri data. *NMR Biomed*, 23(7):803–820, Aug 2010.
- [83] D. K. Jones and C. Pierpaoli. The contribution of cardiac pulsation to variability of tractography results. In *ISMRM, 13th annual meeting, Miami, p.225*, 2005.
- [84] R. Keys. Cubic convolution interpolation for digital image processing. *Acoustics, Speech, and Signal Processing [see also IEEE Transactions on Signal Processing]*, *IEEE Transactions on*, 29(6):1153–1160, 1981.
- [85] S. Kirkpatrick, C. D. Gelatt, and M. P. Vecchi. Optimization by simulated annealing. *Science*, 220:671–680, 1983.
- [86] D.-J. Kroon and C. H. Slump. Mri modalitiy transformation in demon registration. In *Proceedings of the Sixth IEEE international conference on Symposium on Biomedical Imaging: From Nano to Macro, ISBI'09*, pages 963–966, Piscataway, NJ, USA, 2009. IEEE Press.
- [87] J. F. Kurtzke. Rating neurologic impairment in multiple sclerosis: an expanded disability status scale (edss). *Neurology*, 33(11):1444–1452, Nov 1983.
- [88] M. Lazar, D. M. Weinstein, J. S. Tsuruda, K. M. Hasan, K. Arfanakis, M. E. Meyerand, B. Badie, H. A. Rowley, V. Haughton, A. Field, and A. L. Alexander. White matter tractography using diffusion tensor deflection. *Hum Brain Mapp*, 18(4):306–321, Apr 2003.
- [89] K. Levenberg. A method for the solution of certain problems in least squares. *Quart. Applied Math.*, 2:164–168, 1944.
- [90] D. K. B. Li, U. Held, J. Petkau, M. Daumer, F. Barkhof, F. Fazekas, J. A. Frank, L. Kappos, D. H. Miller, J. H. Simon, J. S. Wolinsky, M. Filippi, and S. L. C. f. M. S. R. . Mri t2 lesion burden in multiple sclerosis: a plateauing relationship with clinical disability. *Neurology*, 66(9):1384–1389, May 2006.
- [91] C. Lin, V. Wedeen, J. Chen, C. Yao, and W. Tseng. Validation of diffusion spectrum magnetic resonance imaging with manganese-enhanced rat optic tracts and ex vivo phantoms. *Neuroimage*, 19(3):482–95, 2003.
- [92] F. Lin, C. Yu, T. Jiang, K. Li, and P. Chan. Diffusion tensor tractography-based group mapping of the pyramidal tract in relapsing-remitting multiple sclerosis patients. *AJNR Am J Neuroradiol*, 28(2):278–282, Feb 2007.

- [93] J. A. Little, D. L. G. Hill, and D. J. Hawkes. Deformations incorporating rigid structures. *Computer Vision and Image Understanding*, 66(2):223–232, 1997.
- [94] D. C. Liu, J. Nocedal, D. C. Liu, and J. Nocedal. On the limited memory bfgs method for large scale optimization. *Mathematical Programming*, 45:503–528, 1989.
- [95] B. R. Logan, M. P. Geliazkova, and D. B. Rowe. An evaluation of spatial thresholding techniques in fmri analysis. *Hum Brain Mapp*, 29(12):1379–1389, Dec 2008.
- [96] F. D. Lublin and S. C. Reingold. Defining the clinical course of multiple sclerosis: results of an international survey. national multiple sclerosis society (usa) advisory committee on clinical trials of new agents in multiple sclerosis. *Neurology*, 46(4):907–911, Apr 1996.
- [97] W. P. M. Brett and S. Kiebel. *"Introduction to Random field theory"*, *Human Brain Function*. Academic Press, 2nd edition., 2003.
- [98] N. Makris, D. N. Kennedy, S. McInerney, G. A. Sorensen, R. Wang, V. S. Caviness, and D. N. Pandya. Segmentation of Subcomponents within the Superior Longitudinal Fascicle in Humans: A Quantitative, In Vivo, DT-MRI Study. *Cereb Cortex*, 15(6):854–869, June 2005.
- [99] L. E. Malvern. *Introduction to the Mechanics of a Continuous Medium*. Prentice Hall, 1969.
- [100] K. V. Mardia. *Statistics of directional data / K.V. Mardia*. Academic Press, London ; New York ;, 1972.
- [101] D. W. Marquardt. An Algorithm for Least-Squares Estimation of Nonlinear Parameters. *SIAM Journal on Applied Mathematics*, 11(2):431–441, 1963.
- [102] R. A. Marrie. Environmental risk factors in multiple sclerosis aetiology. *Lancet Neurol*, 3(12):709–718, Dec 2004.
- [103] W. I. McDonald, A. Compston, G. Edan, D. Goodkin, H. P. Hartung, F. D. Lublin, H. F. McFarland, D. W. Paty, C. H. Polman, S. C. Reingold, M. Sandberg-Wollheim, W. Sibley, A. Thompson, S. van den Noort, B. Y. Weinshenker, and J. S. Wolinsky. Recommended diagnostic criteria for multiple sclerosis: guidelines from the international panel on the diagnosis of multiple sclerosis. *Ann Neurol*, 50(1):121–127, Jul 2001.
- [104] Z. Michalewicz. *Genetic algorithms + data structures = evolution programs*. Springer, 1992.

- [105] D. H. Miller, O. A. Khan, W. A. Sheremata, L. D. Blumhardt, G. P. A. Rice, M. A. Libonati, A. J. Willmer-Hulme, C. M. Dalton, K. A. Miszkiet, P. W. O'Connor, and I. N. M. S. T. G. . A controlled trial of natalizumab for relapsing multiple sclerosis. *N Engl J Med*, 348(1):15–23, Jan 2003.
- [106] J. Miller, Rupert G. Developments in multiple comparisons 1966-1976. *Journal of the American Statistical Association*, 72(360):pp. 779–788, 1977.
- [107] J. Modersitzki. *Numerical Methods for Image Registration*. Oxford University Press, 2004.
- [108] J. Modersitzki. *FAIR: Flexible Algorithms for Image Registration*. SIAM, Philadelphia, 2009.
- [109] S. Mori, W. E. Kaufmann, C. Davatzikos, B. Stieltjes, L. Amodi, K. Fredericksen, G. D. Pearlson, E. R. Melhem, M. Solaiyappan, G. V. Raymond, H. W. Moser, and P. C. M. van Zijl. Imaging cortical association tracts in the human brain using diffusion-tensor-based axonal tracking. *Magn Reson Med*, 47(2):215–223, Feb 2002.
- [110] M. Muja and D. G. Lowe. Fast approximate nearest neighbors with automatic algorithm configuration. In *In VISAPP International Conference on Computer Vision Theory and Applications*, pages 331–340, 2009.
- [111] J. A. Nelder and R. Mead. A Simplex Method for Function Minimization. *The Computer Journal*, 7(4):308–313, Jan. 1965.
- [112] H. B. Nielsen and K. Madsen. *Introduction to Optimization and Data Fitting*. Informatics and Mathematical Modelling, Technical University of Denmark, DTU, Richard Petersens Plads, Building 321, DK-2800 Kgs. Lyngby, aug 2007.
- [113] J. Nocedal and S. J. Wright. Line search methods. In T. V. Mikosch, S. I. Resnick, and S. M. Robinson, editors, *Numerical Optimization*, Springer Series in Operations Research and Financial Engineering, pages 30–65. Springer New York, 2006.
- [114] J. I. O’Riordan, A. J. Thompson, D. P. Kingsley, D. G. MacManus, B. E. Kendall, P. Rudge, W. I. McDonald, and D. H. Miller. The prognostic value of brain mri in clinically isolated syndromes of the cns. a 10-year follow-up. *Brain*, 121 ( Pt 3):495–503, Mar 1998.
- [115] A. Ozturk, S. A. Smith, E. M. Gordon-Lipkin, D. M. Harrison, N. Shiee, D. L. Pham, B. S. Caffo, P. A. Calabresi, and D. S. Reich. Mri of the corpus callosum in multiple sclerosis: association with disability. *Mult Scler*, 16(2):166–177, Feb 2010.

- [116] E. Pagani, M. Filippi, M. A. Rocca, and M. A. Horsfield. A method for obtaining tract-specific diffusion tensor mri measurements in the presence of disease: application to patients with clinically isolated syndromes suggestive of multiple sclerosis. *Neuroimage*, 26(1):258–265, May 2005.
- [117] H.-J. Park, M. Kubicki, M. E. Shenton, A. Guimond, R. W. McCarley, S. E. Maier, R. Kikinis, F. A. Jolesz, and C.-F. Westin. Spatial normalization of diffusion tensor mri using multiple channels. *Neuroimage*, 20(4):1995–2009, Dec 2003.
- [118] G. J. M. Parker and D. C. Alexander. Probabilistic monte carlo based mapping of cerebral connections utilising whole-brain crossing fibre information. *Inf Process Med Imaging*, 18:684–695, Jul 2003.
- [119] D. W. Paty and D. K. Li. Interferon beta-1b is effective in relapsing-remitting multiple sclerosis. ii. mri analysis results of a multicenter, randomized, double-blind, placebo-controlled trial. ubc ms/mri study group and the ifnb multiple sclerosis study group. *Neurology*, 43(4):662–667, Apr 1993.
- [120] X. Pennec, P. Fillard, and N. Ayache. A riemannian framework for tensor computing. *Int. J. Comput. Vision*, 66(1):41–66, Jan. 2006.
- [121] C. Pierpaoli and P. J. Basser. Toward a quantitative assessment of diffusion anisotropy. *Magnetic Resonance in Medicine*, 26:893–906, 1996.
- [122] S. M. Pizer, D. S. Fritsch, P. A. Yushkevich, V. E. Johnson, and E. L. Chaney. Segmentation, registration, and measurement of shape variation via image object shape. *IEEE Trans Med Imaging*, 18(10):851–865, Oct 1999.
- [123] J. Pluim, J. Maintz, and M. Viergever. Interpolation artefacts in mutual information based image registration. *Computer Vision and Image Understanding*, 77(2):211–232, 2000.
- [124] J. P. W. Pluim, J. B. A. Maintz, and M. A. Viergever. Mutual-information-based registration of medical images: a survey. *IEEE Transactions on Medical Imaging*, 1:986–1004, 2003.
- [125] C. H. Polman, P. W. O’Connor, E. Havrdova, M. Hutchinson, L. Kappos, D. H. Miller, J. T. Phillips, F. D. Lublin, G. Giovannoni, A. Wajgt, M. Toal, F. Lynn, M. A. Panzara, A. W. Sandrock, and A. F. F. I. R. M. I. . A randomized, placebo-controlled trial of natalizumab for relapsing multiple sclerosis. *N Engl J Med*, 354(9):899–910, Mar 2006.
- [126] C. H. Polman, S. C. Reingold, B. Banwell, M. Clanet, J. A. Cohen, M. Filippi, K. Fujihara, E. Havrdova, M. Hutchinson, L. Kappos, F. D. Lublin,

- X. Montalban, P. O'Connor, M. Sandberg-Wollheim, A. J. Thompson, E. Waubant, B. Weinshenker, and J. S. Wolinsky. Diagnostic criteria for multiple sclerosis: 2010 revisions to the mcdonald criteria. *Ann Neurol*, 69(2):292–302, Feb 2011.
- [127] C. H. Polman, S. C. Reingold, G. Edan, M. Filippi, H.-P. Hartung, L. Kappos, F. D. Lublin, L. M. Metz, H. F. McFarland, P. W. O'Connor, M. Sandberg-Wollheim, A. J. Thompson, B. G. Weinshenker, and J. S. Wolinsky. Diagnostic criteria for multiple sclerosis: 2005 revisions to the "mcdonald criteria". *Ann Neurol*, 58(6):840–846, Dec 2005.
- [128] A. M. Pouch, P. A. Yushkevich, B. M. Jackson, A. S. Jassar, M. Vergnat, J. H. Gorman, R. C. Gorman, and C. M. Sehgal. Development of a semi-automated method for mitral valve modeling with medial axis representation using 3D ultrasound. *J Biomech*, 39(2):933–50, 2012.
- [129] M. J. D. Powell. An efficient method for finding the minimum of a function of several variables without calculating derivatives. *The Computer Journal*, 7(2):155–162, Jan. 1964.
- [130] P. Preziosa, M. A. Rocca, S. Mesaros, E. Pagani, T. Stosic-Opincal, K. Kacar, M. Absinta, D. Caputo, J. Drulovic, G. Comi, and M. Filippi. Intrinsic damage to the major white matter tracts in patients with different clinical phenotypes of multiple sclerosis: A voxelwise diffusion-tensor mr study. *Radiology*, 2011.
- [131] T. G. Reese, O. Heid, R. M. Weisskoff, and V. J. Wedeen. Reduction of eddy-current-induced distortion in diffusion mri using a twice-refocused spin echo. *Magn Reson Med*, 49(1):177–182, Jan 2003.
- [132] P. Rogelj and S. Kovacic. Symmetric image registration. In *Proceedings of SPIE, Vol. 5032, Medical Imaging 2003: Image Processing*, pages 484–493, 2003.
- [133] D. Rueckert, A. F. Frangi, and J. A. Schnabel. Automatic construction of 3d statistical deformation models using non-rigid registration. *IEEE Transactions on Medical Imaging*, 22:77–84, 2003.
- [134] D. Rueckert, L. I. Sonoda, C. Hayes, D. L. G. Hill, M. O. Leach, and D. J. Hawkes. Nonrigid registration using free-form deformations: Application to breast mr images. *IEEE Transactions on Medical Imaging*, 18:712–721, 1999.
- [135] J. Ruiz-Alzola, C.-F. Westin, S. K. Warfield, C. Alberola, S. Maier, and R. Kikinis. Nonrigid registration of 3d tensor medical data. *Med Image Anal*, 6(2):143–161, Jun 2002.

- [136] C. E. Shannon. The mathematical theory of communication. 1963. *MD Comput*, 14(4):306–317, 1997.
- [137] J. G. Sled, A. P. Zijdenbos, and A. C. Evans. A nonparametric method for automatic correction of intensity nonuniformity in MRI data. *IEEE transactions on medical imaging*, 17(1):87–97, Feb. 1998.
- [138] S. M. Smith. Fast robust automated brain extraction. *Hum Brain Mapp*, 17(3):143–155, Nov 2002.
- [139] S. M. Smith, Y. Zhang, M. Jenkinson, J. Chen, P. M. Matthews, A. Federico, and N. De Stefano. Accurate, robust, and automated longitudinal and cross-sectional brain change analysis. *Neuroimage*, 17(1):479–489, Sep 2002.
- [140] L. Snook, C. Plewes, and C. Beaulieu. Voxel based versus region of interest analysis in diffusion tensor imaging of neurodevelopment. *Neuroimage*, 34(1):243–252, Jan 2007.
- [141] E. O. Stejskal and J. E. Tanner. Spin diffusion measurements: Spin echoes in the presence of a Time-Dependent field gradient. *The Journal of Chemical Physics*, 42(1):288–292, 1965.
- [142] C. Studholme. Simultaneous population based image alignment for template free spatial normalisation of brain anatomy. In *WBIR'03*, pages 81–90, 2003.
- [143] C. Studholme, D. L. G. Hill, and D. J. Hawkes. An overlap invariant entropy measure of 3d medical image alignment. *Pattern Recognition*, 32(1):71–86, Jan. 1999.
- [144] J. Talairach and P. Tournoux. *Co-Planar Stereotaxic Atlas of the Human Brain: 3-D Proportional System: An Approach to Cerebral Imaging (Thieme Classics)*. Thieme, Jan. 1988.
- [145] P. Thevenaz, U. E. Ruttimann, and M. Unser. A pyramid approach to subpixel registration based on intensity. *Trans. Img. Proc.*, 7(1):27–41, Jan. 1998.
- [146] P. Thevenaz and M. Unser. Optimization of mutual information for multiresolution image registration. *IEEE Transactions on Image Processing*, 9:2083–2099, 2000.
- [147] J.-P. Thirion. Image matching as a diffusion process: an analogy with Maxwell’s demons. *Medical Image Analysis*, 2(3):243–260, 1998.

- [148] J.-D. Tournier, F. Calamante, and A. Connelly. Robust determination of the fibre orientation distribution in diffusion mri: non-negativity constrained super-resolved spherical deconvolution. *Neuroimage*, 35(4):1459–1472, May 2007.
- [149] J.-D. Tournier, F. Calamante, D. G. Gadian, and A. Connelly. Direct estimation of the fiber orientation density function from diffusion-weighted mri data using spherical deconvolution. *Neuroimage*, 23(3):1176–1185, Nov 2004.
- [150] D. Tschumperlé and R. Deriche. Diffusion tensor regularization with constraints preservation. In *Proceedings of the 2001 IEEE Computer Society Conference on Computer Vision and Pattern Recognition (CVPR)*, volume 1, pages 948–953. IEEE, 2001.
- [151] D. S. Tuch. Q-ball imaging. *Magn Reson Med*, 52(6):1358–1372, Dec 2004.
- [152] D. S. Tuch, T. G. Reese, M. R. Wiegell, N. Makris, J. W. Belliveau, and V. J. Wedeen. High angular resolution diffusion imaging reveals intravoxel white matter fiber heterogeneity. *Magn Reson Med*, 48(4):577–582, Oct 2002.
- [153] R. Turner, D. Le Bihan, J. Maier, R. Vavrek, L. K. Hedges, and J. Pekar. Echo-planar imaging of intravoxel incoherent motion. *Radiology*, 177(2):407–414, Nov 1990.
- [154] M. Unser, P. Thevenaz, and L. Yaroslavsky. Convolution-based interpolation for fast, high-quality rotation of images. *Image Processing, IEEE Transactions on*, 4(10):1371–1381, Aug. 2002.
- [155] K. Van Leemput, F. Maes, D. Vandermeulen, A. Colchester, and P. Suetens. Automated segmentation of multiple sclerosis lesions by model outlier detection. *Medical Imaging, IEEE Transactions on*, 20(8):677–688, 2001.
- [156] K. Van Leemput, F. Maes, D. Vandermeulen, and P. Suetens. Automated model-based tissue classification of mr images of the brain. *IEEE Trans Med Imaging*, 18(10):897–908, Oct 1999.
- [157] T. Vercauteren, X. Pennec, A. Perchant, and N. Ayache. Diffeomorphic demons: Efficient non-parametric image registration. *NeuroImage*, 45(1):Supplement 1, March 2009, Pages S61–S72, Nov. 2008.
- [158] P. Viola and W. M. Wells, III. Alignment by maximization of mutual information. *Int. J. Comput. Vision*, 24(2):137–154, Sept. 1997.

- [159] H. Wang, L. Dong, J. O'Daniel, R. Mohan, A. S. Garden, K. K. Ang, D. A. Kuban, M. Bonnen, J. Y. Chang, and R. Cheung. Validation of an accelerated 'demons' algorithm for deformable image registration in radiation therapy. *Phys. Med. Biol.*, 50(12):2887–2905, 2005.
- [160] Z. Wang, B. C. Vemuri, Y. Chen, and T. Mareci. A constrained variational principle for direct estimation and smoothing of the diffusion tensor field from dwi. In C. J. Taylor and J. A. Noble, editors, *ipmi*, volume 2732 of *Lecture Notes in Computer Science*, pages 660–671. Springer, 2003.
- [161] S. Warach, D. Chien, W. Li, M. Ronthal, and R. R. Edelman. Fast magnetic resonance diffusion-weighted imaging of acute human stroke. *Neurology*, 42(9):1717–1723, Sep 1992.
- [162] L. Wasserman. *All of Statistics, A concise Course in Statistical Inference*. Springer, 2004.
- [163] V. J. Wedeen, T. G. Reese, D. S. Tuch, M. R. Weigel, J. G. Dou, R. M. Weiskoff, and D. Chessler. Mapping fiber orientation spectra in cerebral white matter with fourier-transform diffusion MRI. In *Proceedings of 8th Annual Meeting ISMRM, Denver*, page 82, 2000.
- [164] K. Q. Weinberger and L. K. Saul. An introduction to nonlinear dimensionality reduction by maximum variance unfolding. In *AAAI'06: proceedings of the 21st national conference on Artificial intelligence*, pages 1683–1686. AAAI Press, 2006.
- [165] D. Weinstein, G. Kindlmann, and E. Lundberg. Tensorlines: advection-diffusion based propagation through diffusion tensor fields. In *Proceedings of the conference on Visualization '99: celebrating ten years, VIS '99*, pages 249–253, Los Alamitos, CA, USA, 1999. IEEE Computer Society Press.
- [166] N. I. Weisenfeld and S. K. Warfield. Automatic segmentation of newborn brain MRI. *NeuroImage*, 1:10, May 2009.
- [167] B. L. Welch. The generalization of 'student's' problem when several different population variances are involved. *Biometrika*, 34(1/2):28–35, 1947.
- [168] W. J. Welch. Construction of permutation tests. *Journal of the American Statistical Association*, 85(411):693–698, 1990.
- [169] M. Wels, G. Carneiro, A. Aplas, M. Huber, J. Hornegger, and D. Comaniciu. A discriminative model-constrained graph cuts approach to fully automated pediatric brain tumor segmentation in 3-d mri. In *Proceedings of the 11th international conference on Medical Image Computing and Computer-Assisted Intervention - Part I, MICCAI '08*, pages 67–75, Berlin, Heidelberg, 2008. Springer-Verlag.

- [170] D. J. Werring, C. A. Clark, G. J. Barker, A. J. Thompson, and D. H. Miller. Diffusion tensor imaging of lesions and normal-appearing white matter in multiple sclerosis. *Neurology*, 52(8):1626–1632, May 1999.
- [171] C.-F. Westin, S. Peled, H. Gudbjartsson, R. Kikinis, and F. A. Jolesz. Geometrical diffusion measures for MRI from tensor basis analysis. In *ISMRM '97*, page 1742, Vancouver Canada, April 1997.
- [172] R. P. Woods, S. T. Grafton, C. J. Holmes, S. R. Cherry, and J. C. Mazziotta. Automated image registration: I. general methods and intrasubject, intramodality validation. *Journal of Computer Assisted Tomography*, 22(1):139–152, 1998.
- [173] K. J. Worsley, S. Marrett, P. Neelin, A. C. Vandal, K. J. Friston, and A. C. Evans. A unified statistical approach for determining significant signals in images of cerebral activation. *Hum Brain Mapp*, 4(1):58–73+, 1996.
- [174] H. J. Yu, C. Christodoulou, V. Bhise, D. Greenblatt, Y. Patel, D. Serafin, M. Maletic-Savatic, L. B. Krupp, and M. E. Wagshul. Multiple white matter tract abnormalities underlie cognitive impairment in rrms. *Neuroimage*, 59(4):3713–3722, Feb 2012.
- [175] P. A. Yushkevich, P. T. Fletcher, S. Joshi, A. Thall, and S. M. Pizer. Continuous medial representations for geometric object modeling in 2D and 3D. In *Image and Vision Computing*, pages 17–27, 2002.
- [176] P. A. Yushkevich, H. Zhang, and J. C. Gee. Parametric medial shape representation in 3-d via the poisson partial differential equation with non-linear boundary conditions. *Inf Process Med Imaging*, 19:162–173, 2005.
- [177] P. A. Yushkevich, H. Zhang, T. J. Simon, and J. C. Gee. Structure-specific statistical mapping of white matter tracts. *Neuroimage*, 41(2):448–461, Jun 2008.
- [178] M. Zaitsev, J. Hennig, and O. Speck. Point spread function mapping with parallel imaging techniques and high acceleration factors: Fast, robust, and flexible method for echo-planar imaging distortion correction. *Magnetic Resonance in Medicine*, 52(5):1156–1166, 2004.
- [179] H. Zhang, B. B. Avants, P. A. Yushkevich, J. H. Woo, S. Wang, L. F. McCluskey, L. B. Elman, E. R. Melhem, and J. C. Gee. High-dimensional spatial normalization of diffusion tensor images improves the detection of white matter differences: an example study using amyotrophic lateral sclerosis. *IEEE Trans Med Imaging*, 26(11):1585–1597, Nov 2007.

- [180] H. Zhang, P. A. Yushkevich, and J. C. Gee. Registration of diffusion tensor images. *Conference on Computer Vision and Pattern Recognition - CVPR'04*, 01:842–847, 2004.
- [181] H. Zhang, P. A. Yushkevich, and J. C. Gee. Deformable registration of diffusion tensor mr images with explicit orientation optimization. *Med Image Comput Comput Assist Interv*, 8(Pt 1):172–179, 2005.
- [182] Y. Zhang, S. Smith, and M. Brady. Hidden markov random field model and segmentation of brain mr images. *IEEE TRANSACTIONS ON MEDICAL IMAGING*, 20:45–57, 2001.